Downloaded from orbit.dtu.dk on: Dec 19, 2017

Technical University of Denmark

Fabrication of polymer microcantilevers by nanoimprint lithography

Greve, Anders; Svendsen, Winnie Edith; Boisen, Anja

Publication date:
2010

Document Version
Publisher's PDF, also known as Version of record

Link back to DTU Orbit

Citation (APA):
Greve, A., Svendsen, W. E., & Boisen, A. (2010). Fabrication of polymer microcantilevers by nanoimprint lithography. Kgs. Lyngby, Denmark: Technical University of Denmark (DTU).

DTU Library
Technical Information Center of Denmark

General rights
Copyright and moral rights for the publications made accessible in the public portal are retained by the authors and/or other copyright owners and it is a condition of accessing publications that users recognise and abide by the legal requirements associated with these rights.

- Users may download and print one copy of any publication from the public portal for the purpose of private study or research.
- You may not further distribute the material or use it for any profit-making activity or commercial gain
- You may freely distribute the URL identifying the publication in the public portal

If you believe that this document breaches copyright please contact us providing details, and we will remove access to the work immediately and investigate your claim.

DTU Nanotech
Department of Micro- and Nanotechnology

DTU

Fabrication of Polymer Microcantilevers by Nanoimprint Lithography

PhD. Thesis

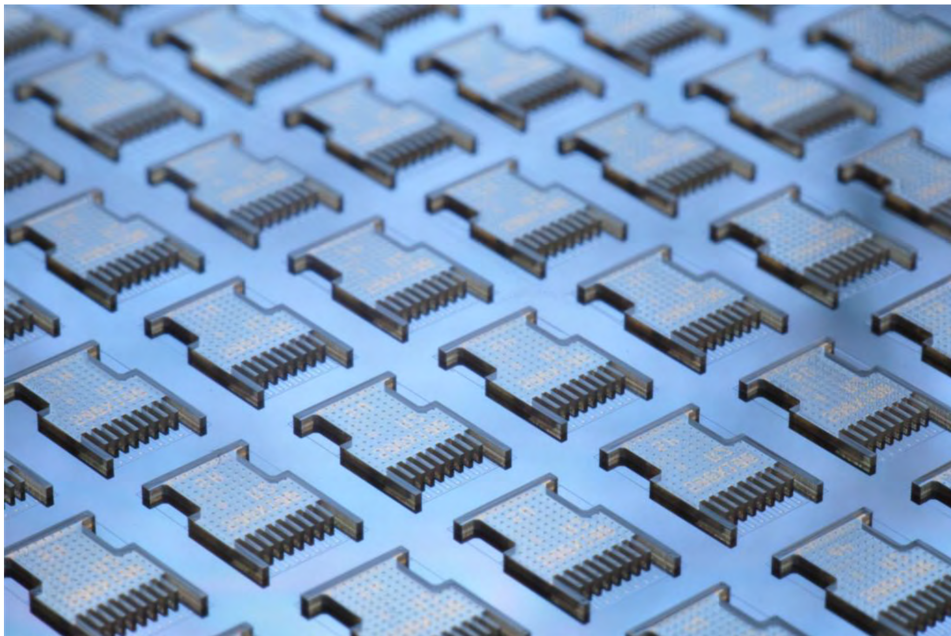

Anders Greve

Supervisors:

Prof. Anja Boisen and Asc. Prof. Winnie Svendsen
DTU Nanotech

January 22, 2010

Preface

This thesis has been written as a partial fulfillment of the requirements for obtaining the PhD degree at the Technical University of Denmark (DTU). The PhD project has been carried out at the department for Micro- and Nanotechnology (DTU Nanotech) in the period from 1st of February 2007 to 31st of January 2010. During these three years a six months period has been spent at U.C. Berkeley Mechanical Department under Professor Arunava Majumdar.
The PhD project is part of the Nanonose research programme supported by the ministry of research and innovation through the NABIIT programme. This project has been conducted in the Nanoprobes group within the NanoSystems Engineering section at DTU Nanotech.

Professor Anja Boisen
Main supervisor

Associate Professor Winnie Swendsen
Co-supervisor

My first thanks goes to professor and group leader Anja Boisen. You have been a great supervisor offering endless support and new opportunities for me to develop both personally and professionally. It has been a great inspiration to see how you manage the group and integrate different people to work together. Which leads me to the next group of people to thank, which is the Nanoprobes group. I have had a great time working with a lot of different intelligent people from all over the world. During my time in the group the activities have taken off and three new groups have been established from it. One of which is headed by my co-supervisor Winnie Svendsen, whom I would also like to thank for being a great help, especially at the beginning of the project.
I would also like to thank the people in the NanoNose Project, especially the people working fulltime in the project: Søren Dohn, David Larsson and Claus H. Nielsen. It has not been an easy task trying to work together and plan for things to work together when it has never been made before. But everybody has met the challenge with big smiles and optimism, which have made it a both a fun and encouraging environment to work in.
For more technical help on the project I would like to thank Stephan Keller for help on the fluorocarbon and SU8 processing, and Asger L. Vig for help and introduction to nanoimprint lithography.

A special thanks to Professor Arunva Majumdar for welcoming me to his group and laboratory at the Mechanical Department at University of California Berkeley and PhD Marta Cerutti for helping me in the lab and introducing me to the Californian life style.

Last a thanks to the people I have not yet mentioned but also have helped me through the thesis.

Anders Greve
January 31st 2010
DTU Nanotech
Technical University of Denmark

Abstract

This thesis presents a novel fabrication method for microcantilevers for different sensing applications. Microcantilevers are thin beams clamped at one end like a miniaturized diving board. Over the last 10-15 years they have emerged as a platform for ultra senstive sensors for gas and bio/chemical applications. The specific application is controlled by the functionalization of the cantilevers which can be done with different coatings which offer selectivity to different target molecules. Once the target molecules interact with the coating it will give rise to an increase in mass and a change in surface stress. Traditionally, these measurements have been performed using silicon based cantilevers, but as these are expensive to fabricate. Therefore, people are moving to cheaper polymer materials, which are also softer thus enhancing the signal from surface stress. The conventional polymer fabrication technique, injection molding, offers very poor definition of the microcantilever, since it requires that a very thin cavity is filled in order to realize the structures. By using NanoImprint Lithography (NIL) for defining the cantilevers, the microcantilever can be defined in thermoplastic materials with added surface structures without complicating the processing. In this work microcantilevers with a length of 500 μm, a width of 100 μm and a thickness of 4.5 μm have been realized. The yield of these microcantilevers is above 95 % and the thickness variation is 67 nm, which is comparable to commercial silicon cantilevers. The fabrication process also allows for fabrication of advanced three dimensional structures which are not economically viable for silicon based cantilevers.

For the functionalization of the cantilevers a new process of using a mechanical shadow mask together with plasma polymerization have been introduced. This allows us to coat individual cantilevers on a wafer scale which for the current design means over 300 chips, each with eight cantilevers. The shadow mask is aligned by hand using the mechanical structures, with a precision of 20 μm. As a proof-of-principle the cantilevers have been coated with maleic anhydride, polyvinylpyrrolidone and polystyrene, and tested against water and ethanol. The response shows that the cantilevers have indeed been coated with different polymers.

Dansk Resume

Denne Ph.D.-afhandling omhandler udviklingen af en ny metode til at fremstille nanomekaniske sensorer på. Bjælken er fikseret i den ene ende, mens den anden ende er frit svævende som en vippe. Denne type sensorer har været under udvikling som en sensor platform over de sidste 10-15 år, og den kan bruges til at lave ultra følsomme målinger indenfor biologiske og kemiske målinger. Selektiviteten for sensoren bliver styret af hvilken overflade behandling bjælken får. Den samme bjælke kan bruges til mange forskellige formål alt efter hvordan den bliver funktionaliseret til at detektere specifikke molekyler. Når molekylet så kommer og binder på overfladen på bjælken vil den ændre overfladestresset og massen for bjælken. ændringen i stress kan måles ved at observere udbøjningen af bjælken, mens massen kan detekteres ved måle ændringen i egenfrekvensen for bjælken. Disse mikrobjælker bliver traditionelt fremstillet i silicium baserede materialer, hvilket dog har den ulempe at de bliver dyre og stive. Ved at lave bjælkerne i plastik kan de blive både billigere og blødere. Almindelige fremstillings teknikker til objekter i plastik så som sprøjtestøbning, egner sig meget dårligt til fremstilling af mikrobjælker, da det kræver at meget små kaviteter bliver fyldt under processen. Ved at brug NanoImprint Litografi (NIL) kan man lave meget bedre definerede bjælker og inkludere nanostrukturer på overfladerne uden at komplicere fremstillingen yderligere. I dette arbejde er der blevet fremstillet bjælker med en længde på 500 μm, bredde på 100 μm og tykkelse på 4,5 μm. Udbyttet for fremstillingen ligger på over 95 % og variationen på tykkelsen er på 67 nm, hvilket er sammenligneligt med kommercielle silicium baserede mikrobjælker. Den nye fremstillings teknik tillader også at der kan bliver inkluderet mere avancerede tre dimensionelle strukturer, som ikke kan masse produceres i silicium. Funktionaliseringen af de fremstillede mikrobjælker kan gøres ved en ny metode som også er blevet udviklet i projektet. Ved at bruge en skyggemaske fremstillet i silicium kan enkelte bjælker funktionaliseres på en skive samtidig. Skygge masken bliver mekanisk positioneret med en præcision på 20 μm i forhold til bjælkerne og placeret i et plasma kammer som så deponere en tynd plastikfilm. Skyggemasken sørger så for at plastikfilmen kun rammer de rigtige bjælker over en hel skive som indeholder 300 sensorer med hver otte bjælker. For at bevise det virker er tre forskellige polymere blevet deponeret gennem skyggemasken på bjælkerne og tested. De funktionaliserede bjælker gav forskellige udslag fra vand og acetone dampe afhængig af hvilken polymer der var blevet lagt på. Da de andre bjælker på sensoren ikke gav samme signal kunne det konkluderes at det virkede.

Contents

1 Introduction **1**
1.1 Sensors Motivation 1
1.2 Cantilever Sensing 3
1.3 Fabrication of Microcantilevers 5
1.4 NanoNose Project 8
1.5 Motivation and Novelty 9
1.5.1 Overview of Thesis 9

2 Theory **11**
2.1 Bending of Cantilever 11
2.1.1 Resonant Frequency 14
2.2 Introduction to Lasers and VCSEL 14
2.3 Cantilever Sensing 16
2.4 Interference in a VCSEL 17
2.5 Summary 19

3 Design **21**
3.1 Nanoimprint Lithography 21
3.2 Design Consideration for NIL 25
3.3 Free Standing NIL Structures 27
3.4 Advanced Structures 29
3.5 Complete structure 31
3.6 Summary 32

4 Fabrication **33**
4.1 Fabrication of Stamp 33
4.2 Materials 36
4.3 Fabrication of Polymer Cantilever 37
4.4 Challenges During Processing 44
4.5 FIB Cantilever 48
4.6 Summary 50

5 Characterization **51**
5.1 Static Characterization 51
5.2 Dynamic Performance 54

5.3 Summary 55

6 Peptide-Based Receptors for Explosives 57

6.1 Setup 57
6.2 Characterization 59
6.3 Peptide Measurements 63
6.4 Summary 68

7 Shadow Mask and Functionalization 69

7.1 Design of Shadow mask 69
7.2 Fabrication of Shadow mask 71
7.3 Mechanical Alignment 75
7.4 Deposition through shadow mask 77
7.5 Summary 77

8 Setup and Measurements 79

8.1 Setup 79
8.2 Uncoated response 82
8.3 Coated Response 84
8.4 Differential Measurements 90
8.4.1 Resonance Measurements 91
8.5 Surface Structures 92
8.6 VCSEL Response 93
8.7 Summary 95

9 Conclusion 97

9.1 Outlook 98

A Publications and Conference Contributions 109

A.1 Articles 109
A.2 Conferences 110

B Detailed Process Sequences 111

C Matlab files for VCSEL 115

D Mask Designs 119

Chapter 1

Introduction

1.1 Sensors Motivation

Sensors have become a very important part of our lifes, and are present in most of our consumer goods. Normally, we do not think much about it until they start to fail when we have to use them. In mobile phones there has always been a microphone which translates the sound waves into an electrical signal. However, with modern phones the microphone is far from the only sensor, many now have built in accelerometers and tilt sensors. Modern cars also have a huge array of sensors just to monitor the performance of the engine (temperature, pressure ...). Probably more noticeably over the last decade, airbag and accelerometers are being fitted into the car. With the prices dropping more accelerometers are placed inside the car so that also the specific kind of impact can be calculated and the specific airbags deployed [1].

All these sensors have been around for some time and have thus been highly optimized and have become very cheap. However, there is still a huge demand for sensors which have not yet been fulfilled. Biosensors for the medical industry have been around for many years but still it is challenging to compete with nature. Maybe the best example of a highly effective sensor is a dog's nose. It is highly sensitive and selective, it can be used to find burried land mines, or minute traces of hidden narcotics. It can even be used to test if people are sick just by sniffing the patients breath [2].

A sensor can generally be divided into three parts, see Fig. 1.1. The first is the receptor which gives the selectivity of the sensor. For the biochemical sensor this could be antibodies, or for gas sensing a coating with a specific affinity. The second part is the transducer which is the main source for the sensitivity of the sensor. The transducer translates the capture of molecules into a measurable quantity. It could be fluorescence molecules, a microcantilever or a membrane in a microphone. The third and final part is the readout from the sensor, which could be a fluorescent scanner, an optical laser or an electronic circuit. This part also has a huge impact on the sensitivity and range of the sensor.

Over the years many different types of sensors have been developed and improved, but there are still many applications where the sensor are very inaccurate. The ideal

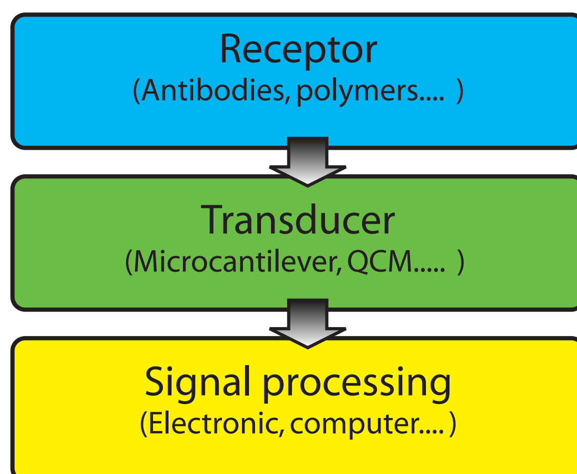

Figure 1.1: A sensor can be divided up into three parts: receptor, transducer and readout. While the receptor gives the selectivity of the sensor the transducer and readout work together to give the sensitivity of the sensor.

sensor is very specific and sensitive, which means that only a very small amount of sample is needed and it can be detected in mixtures with other compounds. Depending on the application a number of false positives are more acceptable than false negative. As an example in an airport it would be acceptable to have to check an extra bag for explosives even though it was empty, but it is not acceptable to have a person who is able to carry on explosive compounds unnoticed. For other substances like for example drugs, a higher false negative rate is accepted since the drugs are not deadly to other people.
Furthermore, the sensors need to be cheap and compact and preferably portable. If the price of the sensor is too high the impact of the sensor will be limited and thus not reaching its full potential. The sensor should preferably be small so it takes up less space and can be moved around. If the sensors require little supply materials, chemicals and power, and it is robust enough it could be made into a hand held device for use in the field. Even if all these requirements are met the success of the sensor is still not guaranteed. The sensor needs to have an easy interface for operations, preferably most of the analysis should be done by the sensor, just telling the operator if the target is present.
To summarize the ideal sensor is:

Selective The ideal sensor should be 100 % selective, only giving a response to the target and nothing else. It should also achieve this selectivity with a short response time.

Sensitive The ideal sensor can detect minute traces, ideally single molecules. The sensitivity should not limit the range of operation.

Cheap The sensor should be cheap so that the cost is not hindering its use.

This is of course not possible to achieve for all applications. Depending on the industry the price of the sensor can be high. For example airports in U.S.A. used 2.67 billion$ in 2006 on security [3]. For diagnostic purposes disposable sensors are often required to minimize cross contamination.
An illustration of a receiver operating curve showing the connection between false positive and true positive, is shown in Fig. 1.2. The problem for many sensors is that in order to minimize the number of missed true positives, the number of false positives also increases. By improving the sensors it is possible to get a higher number of true positives while maintaining a low number of false positive. A possible shortcut to this is to combine different types of sensors for the same application [4, 5].

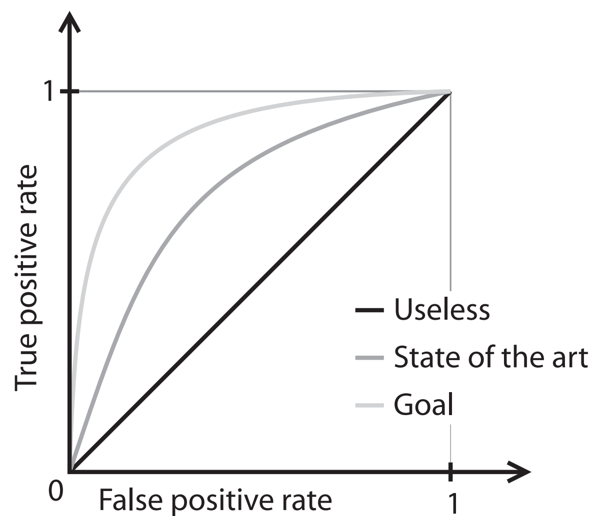

Figure 1.2: Reciever operating characteristic curve (true positive rate or sensor sensitivity versus false positive) reproduction from [6]. The "Useless" line a sensor equivalent to represents flipping a coin. The "Goal" is to move as close as possible to a sensor that have a high true positive rate while maintaining a low false positive rate.

1.2 Cantilever Sensing

The use of microcantilevers for sensing started in 1986, when the Atomic Force Microscope (AFM) was invented [7]. An AFM can measure the topography of a surface by moving a cantilever with an extremely sharp tip over the sample. The movement of the cantilever is then monitored by a readout system. For the first systems the cantilever deflection was detected by a Scanning Tunneling Microscope (STM) tip placed above the cantilever [7]. Now, the most common method of detecting the movement of the cantilever is pointing a laser beam at the tip of the cantilever and use a detector to observe the movement of the reflected laser beam. Other methods for detecting the movement of the cantilever have also been demonstrated. One example is a piezoresistive readout has been developed and has the advantage of being able to measure in nontransparent mediums [8, 9, 10].

The AFM cantilever has a sharp tip for scanning the surface. For sensing purposes, this tip is not necessary. The idea of using cantilevers for chemical sensing has existed since the 1940's [11], but it was not until the cantilevers could be made with micro/nano dimensions that the true potential could be realized. The cantilever can be operated in three fundamentally different modes.

- *Surface stress.* A biochemical reaction takes place on the surface of the cantilever. When target molecules bind to a selective surface coating they will induce a surface stress, thus causing the cantilever to bend, see Fig. 1.3(a).
- *Change in temperature.* When an exothermic or endothermic reaction takes place it will change the temperature of the cantilever. If the cantilever is a sandwich of materials with different Coefficient of Thermal Expansion (CTE), it will bend due to the bimorph effect, see Fig. 1.3(b).
- *Change in mass.* The resonant frequency depends on the mass of the system resonating. Therefore an added mass will change the frequency, see Fig. 1.3(c).

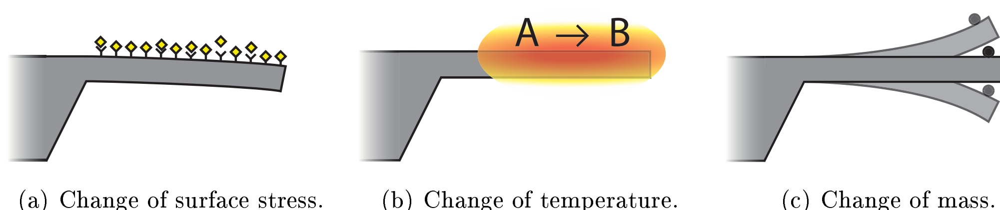

(a) Change of surface stress. (b) Change of temperature. (c) Change of mass.

Figure 1.3: Three different detection principles using a cantilever. (a) illustrates change in surface stress due to chemical adsorption. (b) change in temperature due to chemical reaction on the cantilever. (c) mass change can be measured due to change in frequency.

As was the case for the AFM, the readout can be done in many different ways. The most common ways to detect the cantilever deflection is by optical or piezoresistive readout [12]. The optical readout has the advantage of higher sensitivity and it is less sensitive to electrical noise [13, 14]. The measurement of the surface stress created from molecular binding is only possible because the cantilever can be made very thin. The cantilever has a very small thermal mass and therefore it does not require a lot of energy to change the temperature of the cantilever. It is therefore possible to measure the energy produced by chemical reactions in very small quantities. The readout can either be done by measuring the bending induced by the bimorph effect or by a temperature sensitive resistor on the cantilever. A sensitivity as low as 100 pW has been demonstrated [15, 16]. As mentioned previously the thermal constant for these micro structures is very small, and it is therefore possible to monitor very fast temperature changes [17, 18].
The mass of a particle could be measured by the deflection of the cantilever if large enough. However, a much more sensitive way is to measure the frequency change of the cantilever with and without the particle. The frequency is strongly dependent on the mass of the system, and as the cantilever can be made very small and thereby very

light, even a small particle would change the mass of the system enough to change the frequency. The highest sensitivity is achieved in high vacuum as the damping of the cantilever movement is minimized, but measurements are also possible in air. Resonant frequency detection can also bee done in liquid, but other microstructures work better in this enviroment, like for example membranes or Quartz Crystal Microbalances [19, 20].
Different companies are commercializing products that enable these types of measurements. Cantion A/S offers a system for detecting the surface stress by piezoresistive readout [21]. Companies like Protiveris Gmbh and Concentris Gmbh are also using optical readout [22, 23].
The measuring method can be a combination of the methods mentioned above, thus increasing the information extracted from the experiment. If surface stress is measured during the adsorption of molecules and the resonant frequency change is measured before and after the adsorption, both the mass and the surface stress can be calculated from the experiment [24]. This could increase the selectivity of the sensor, which is just as important a parameter as the sensitivity, and for micro sensors, and perhaps the biggest challenge.

1.3 Fabrication of Microcantilevers

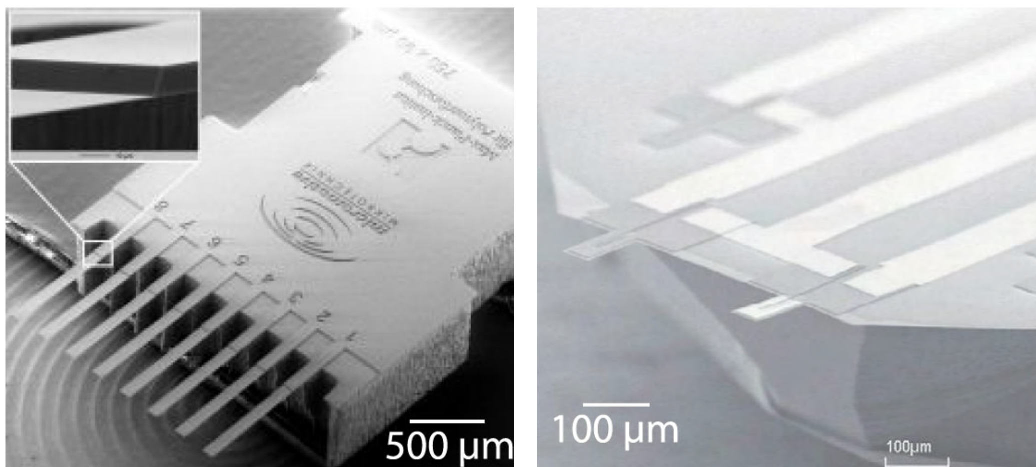

(a) Commercial available single crystalline silicon cantilevers [25].

(b) Silicon cantilever with built-in piezoresistor [26].

Figure 1.4: Examples of silicon microcantilevers. (a) is an SEM picture of a commercial flat silicon cantilever array for sensing purposes. The cantilevers are passive so an external readout system is needed. (b) shows two silicon based cantilever with integrated piezo resistors for measuring the movement of the cantilever.

Silicon cantilevers are dominating the market for cantilever sensors and for good reasons. Silicon processing is a huge industry, which has made the processing highly optimized and reproducible. Furthermore, crystalline silicon makes good resonators,

and they can be made very thin for surface stress measurements. Silicon cantilever designed for sensing are commercially available from several companies, see Fig. 1.4(a). Cantilevers for static measurements are typically around 1 μm thick and 450-950 μm long. Special, sensitive cantilevers of 500 nm thickness and 500 μm length are also available [22, 25]. Silicon processing does also add the possibility of incorporating a piezo resistor into the cantilever when doping the silicon. Doped silicon has a high piezo coefficient making the cantilevers very sensitive. Even though silicon cantilevers are highly optimized and are fabricated using standard silicon processing, there is still a thickness variation of $\pm$300 nm between chips and $\pm$50 nm on each chip. The spring constant can vary from 8-60 mN/m for a 450 μm long cantilever [25].
Silicon fabrication relies on very expensive machinery and foundries. Furthermore, for static mode, silicon is not a very soft material and therefore the bending signal is reduced. By fabricating the cantilevers in polymers potentially softer cantilevers can be fabricated at a lower cost. Microcantilevers of SU8 have been fabricated for AFM, which is currently the largest market for microcantilevers, see Fig. 1.5(a) [27]. But SU8 cantilevers for sensing purposes have also been realized, see Fig. 1.5(b) [28].

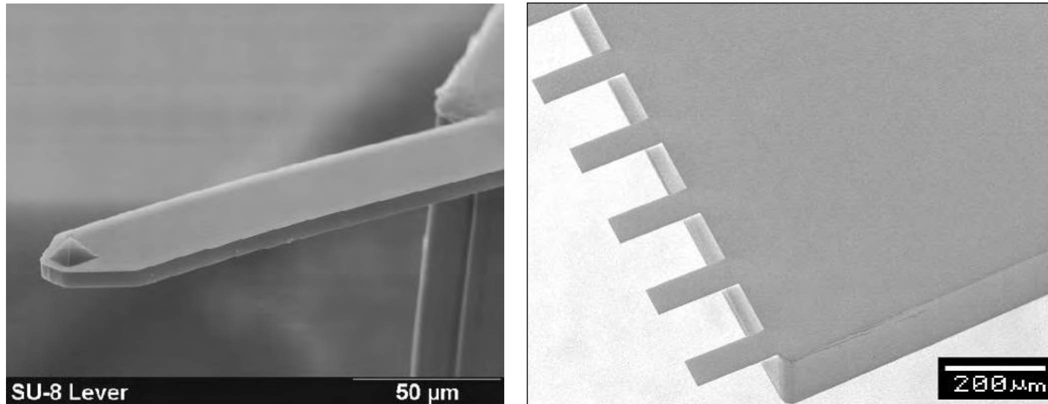

(a) AFM cantilever made of SU8 [27]. (b) Flat SU8 cantilever [28].

Figure 1.5: Different polymer cantilevers realized in SU8. (a) shows an AFM cantilever completely fabricated in SU8, to make the tip a silicon mould is used. (b) shows an array of flat SU8 cantilevers intended for sensing applications.

SU8 cantilevers still require many cleanroom facilities such as UV lithography machines. In order to make even cheaper microcantilevers, microinjected cantilevers have been demonstrated, see Fig. 1.6(a) [29]. To make even thinner cantilever a solvent casting technique can be used, seeFig. 1.6(b) [30].
These injection molded cantilevers have a length of 500 μm, a width of 100 μm and thickness 10 μm. They have been used for chemical thiol sensing [31]. A closer look at a finished cantilever (Fig. 1.7) reveals the problem of poorly defined cantilevers and surfaces. The standard deviation for the width and thickness is 5 μm and 400 nm respectively. Furthermore the fabricated chips had to be removed manually from the mould after injecting before the next chip could be produced. This procedure is

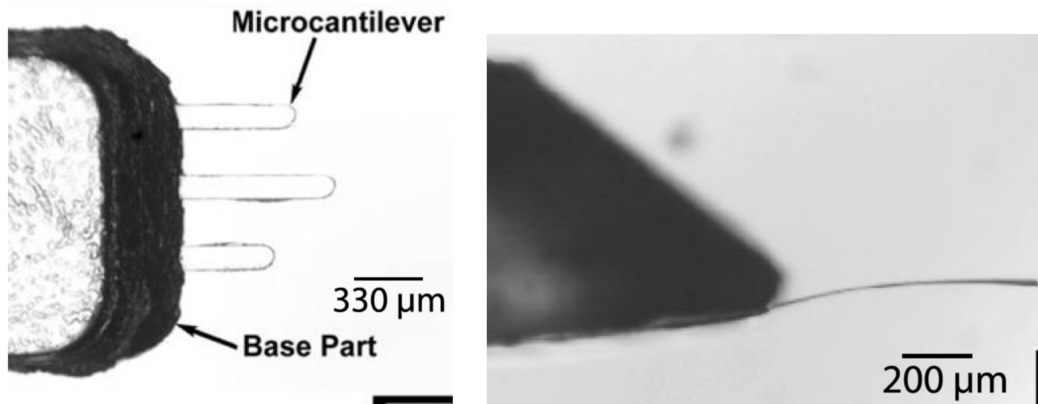

(a) Optical micrograph of an injection moulded polystyrene part showing complete mould cavity filling [29].

(b) PS cantilever made by solvent casting with a thickness of 2 μm, 500 μm length and 50 μm width [30].

Figure 1.6: Examples of different microcantilever fabricated in polystyrene.

severely limiting the benefits from using injection molding techniques for cheap mass production.

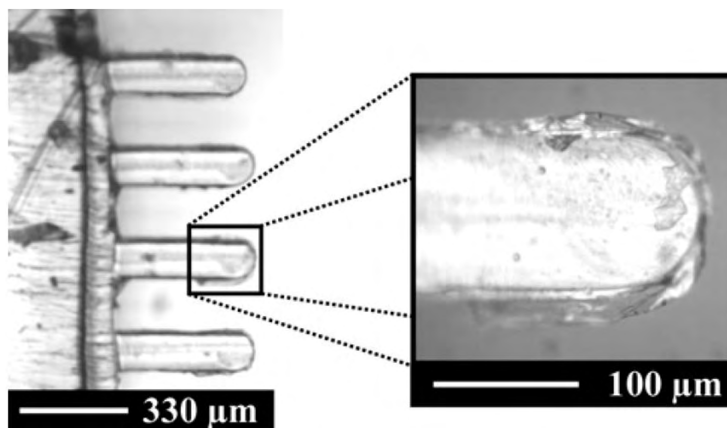

Figure 1.7: Optical micrograph of a polystyrene microcantilever fabricated by microinjection molding [31]. The close up of the tip shows how the polymer starts to flow outside the mould defining the cantilevers, thus the lateral definition of the cantilever is very poor when using this technique.

It has also been demonstrated that it is possible to fabricate AFM cantilevers by injection molding. This is acheved by making an indentation for the tip in the mould for the tip [32].

1.4 NanoNose Project

The scope of the NanoNose program is to develop a gas sensor - or an "artificial nose" based on polymer cantilever arrays and an optical detection system. The principle is that molecules adsorbed on a micrometer-sized cantilever will cause the cantilever to deflect due to changes in surface stress. Alternatively, a mass change can be detected by monitoring a shift in the resonant frequency of the cantilever. For mass detection the cantilever should be as small as possible (nanometer dimensions) in order to increase the mass sensitivity. The artificial nose will be capable of accurately recognizing and quantifying a number of different airborne chemical entities present at extremely low concentrations simultaneously.
The research project is a collaboration between DTU Nanotech - Department of Micro- and Nanotechnology and DTU Photonics - Department of Communications, Optics and Materials, both at DTU, The Polymer Department at RISØ, and Centre for Microtechnology and Surface Analysis at DTI. The project furthermore has a collaboration with the companies Alight Technologies A/S, Unisensor A/S, Niro A/S and Danfoss A/S. The companies will identify specific applications of the artificial nose and provide key technological components.

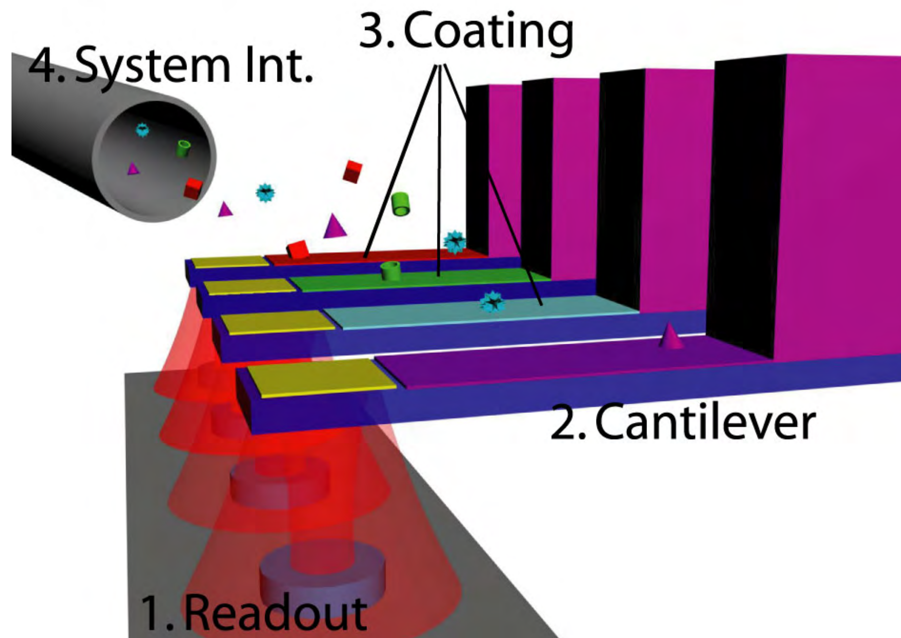

Figure 1.8: 3D illustration of the NanoNose system. 1. Readout is done by VCSEL emitting laser light onto the microcantilever. 2. The cantilever is fabricated by NIL, which has not been done before. 3. Coating is done by plasma polymerization of different polymers. 4. System integration is design a setup where sensor can be tested.

The principle of using an array of polymer coated cantilevers for sensing has been presented before for simple solvents [33, 34]. The novelty in this project primarily lies in

the new readout system using selfmixing interferometry in a VCSEL (vertical-cavity surface-emitting laser), a new fabrication technique for the microcantilever employing nanoimprint lithography, and the polymers are made by plasma polymerization. An overview of the system is shown in Fig. 1.8.
The VCSEL readout scheme allows for a very sensitive detection of the cantilever deflection in a very compact system. While the combination of a new way of fabricating cantilevers can also potentially help to improve the readout system and increase the signal from the coatings. Furthermore, the new fabrication technique will allow for more reproducible cantilevers, compared to what can be achieve by previous techniques in similar materials. By using plasma polymerization to coat the cantilevers a much more uniform coating on the cantilever can be achieved, and it can be done on a larger scale. The main focus points for sensing have been on solvents recognition and explosive compounds.
There are four people employed on the project, so the project is divided up into four different segments. Some of the other parts related to this thesis will be introduced as they are used.

1. **Readout** The readout system is developed at DTU photonics and PhD David Larsson is hired as a Post Doc. to work on this part
2. **Cantilever** Is the topic of this thesis
3. **Coating** Thin polymer coatings are deposited using plasma polymerization and are used for sensing purposes the coatings are characterized by QCM and AFM. This part is carried out at DTU RISØ by PhD stud. Claus H. Nielsen.
4. **System Integration** The system was orignally part of this thesis but after $\frac{1}{2}$ a year PhD Søren Dohn was hired to continue and finish this. Thus the focus of this thesis was moved to fabrication of the cantilever.

The Nanonose research programme is supported by the ministry of research and innovation and the project was awarded through the NABIIT programme.

1.5 Motivation and Novelty

The aim of this project is to design, fabricate and characterize polymer cantilevers for the NanoNose project by NanoImprint Lithography (NIL). It is important that the cantilevers can work together with the readout system and the polymer coating that needs to be deposited. Most of this project is about developing new technologies and with this comes the challenge of getting these to work together. Therefore, part of the focus of the work has also been on making sure that it is possible to do the readout using the VCSEL and coat the cantilevers.

1.5.1 Overview of Thesis

- Chapter two will describe the general mechanical theory for microcantilevers in static and dynamic mode. The theory behind the novel readout system with

the VCSEL will be described.

- In chapter three NIL will be introduced and the consideration for fabricating cantilevers by NIL will be discussed. A final process sequence for the fabrication is presented.
- The fabrication of the cantilever will be presented in chapter four. First, the stamp is fabricated which is then used to fabricate the polymer cantilevers. The fabrication did have some challenges and these are presented separately.
- In Chapter five the fabricated cantilevers are characterized for the static and dynamic performance.
- Peptide-Based Receptors have been developed for explosives detection at U.C. Berkeley and in chapter six they will be tested on the cantilevers
- Chapter seven describes the fabrication and use of shadow mask which is used to control which cantilevers will be functionalize on the wafer.
- The different parts come together in chapter eight where first the test setup is described, and then the coated cantilevers are tested. Finally, the readout of the cantilevers by the VCSEL readout system is presented.
- Chapter nine is the conclusion of the thesis highlighting what has been achieved and what can be done in the future.
- Appendix A includes the list of published articles during this project.
- In appendix B the detailed process sequence for the different parts are presented.
- The Matlab scripts for the theory behind the readout using the VCSEL is presented in appendix C.
- Appendix D presents the final mask design.

Chapter 2

Theory

This chapter will go through the necessary theory used in this project. Since the major part of the project is concerning cantilever sensing, the basic mechanics for a cantilever with respect to end-point deflection, surface stress sensitivity and resonant frequency will be described. The second part will go through the theory behind the special readout scheme planed for in the project. First, the basics behind a VCSEL is explained and then the theory behind how the self-mixing can be used for measuring the deflection of the cantilever.

2.1 Bending of Cantilever

The fundamental sensing part in the project is a cantilever. It is therefore essential to understand the basic mechanics behind the cantilever movement. The cantilever can either operate in static or dynamic mode. For the static mode there are two scenarios of interest, the simplest being the end point deflection and the second being the surface stress situation which is also the most important for this work.
For this project the cantilever will be made of a single material thus making the mechanics simpler. The cantilever is rectangular and has a width w, length L and thickness t. The deflection can be described by.

$$\frac{d^2u}{dx^2} = -\frac{M}{EI}; \tag{2.1}$$

where u describes the deflection at the position along the cantilever at position x [35]. M is the moment, E is Young's modulus and I is the cross sectional area moment of inertia. For a rectangular cantilever I is given by $\frac{wt^3}{12}$.
For the case of the end point deflection, a force F is applied at the tip of the cantilever, see Fig. 2.1 for details. For small displacements the cantilever can be approximated with a spring and it is possible to apply Hooke's (law for the tip of the cantilever $x = L$):

$$F = -ku(L) \tag{2.2}$$

where k is the spring constant for the cantilever. In order to solve Eq. (2.1) the moment needs to be defined. Along the length of the cantilever the moment will

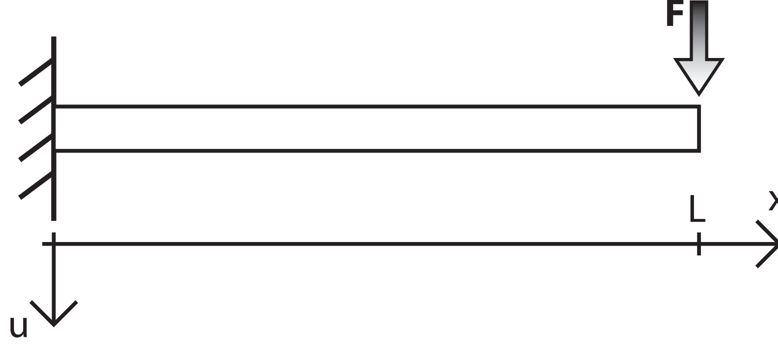

Figure 2.1: Graphical illustration of point deflection of a cantilever with one fixed end and a free end. A force F is applied at the tip ($x = L$) of the cantilever.

change as $M = -F(L - x)$, so at the tip for $x = L$ the moment is zero. For the perfectly fixed beam at $x = 0$, the following boundary conditions can be used:

$$u(0) = 0$$

$$\left.\frac{du}{dx}\right|_{x=0} = 0$$

The solution to Eq. (2.1) is then:

$$u(x) = \frac{Fx^2}{2EI}\left(L - \frac{x}{3}\right) \tag{2.3}$$

At the apex of the cantilever ($x = L$) bending is

$$u(L) = \frac{L^3}{3EI}F \Leftrightarrow F = \frac{3EI}{L^3}u(L) \tag{2.4}$$

and the spring constant for the cantilever is therefore:

$$k = \frac{3EI}{L^3} = \frac{Ewt^3}{4L^3} \tag{2.5}$$

It should be noted that for the point deflection the signal depends on the thickness to the power of three (t^3).
In the NanoNose project the cantilever will be coated with a thin polymer film t_f, which will create a stress, thus bending the cantilever. The polymer coating will be significantly thinner than the cantilever thickness $t >> t_f$ and thus the polymer coating can be considered as a surface stress. In this case there is an in-plane force acting around the neutral axis, where the neutral axis can be approximated with the middle of the cantilever, hence the force acting on the cantilever is $F = wt_f\sigma$, where σ is the surface stress [N/m^2]. The moment can then be calculated as the distance from the neutral axis is $-t/2$, $M = wt_f\sigma t/2$ by inserting this expression for the moment into Eq. (2.1)

$$\frac{d^2u}{dx^2} = \frac{wt\sigma t_f}{2EI} \tag{2.6}$$

The film stress can be expressed as $\sigma_s = t_f\sigma$, where σ_s denotes the surface stres. The same boundary conditions apply because the assumption was just a fixed beam, we now get:

$$u(x) = \frac{wtx^2}{4EI}\sigma_s \tag{2.7}$$

For a uniaxial surface stress in the x direction this is a fairly good approximation, but for a more realistic case the biaxial stress also needs to be included. The Young's modulus is replaced by $E/(1-\nu)$ where ν is the Poisson's ratio for the cantilever material. By inserting the cross sectional moment of inertia for the cantilever the result is

$$u(x) = \frac{(1-\nu)wtx^2}{4EI}\sigma_s = \frac{3(1-\nu)x^2}{Et^2}\sigma_s \tag{2.8}$$

The deflection of a cantilever with length L the maximum deflection can be found to

$$u(x) = \frac{3(1-\nu)L^2}{Et^2}\sigma_s \tag{2.9}$$

Comparing the end point deflection with the surface stress generated deflection, it is seen that the deflection now only scales with t^2. This is important for the comparison of a polymer and silicon based cantilever, since it is difficult to fabricate a thin cantilever in polymer. Thus, a polymer cantilever has an advantage when used for surface stress sensing. By a quick comparison the Young's modulus of polymers like SU8 and Topas are around 100 times less than for silicon, which means that the same surface stress sensitivity can be achieved by a cantilever 10 times thicker.

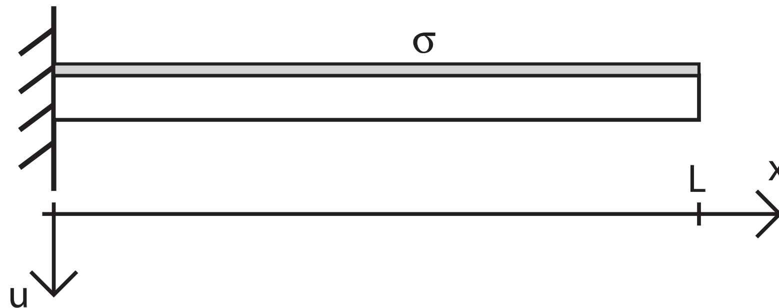

Figure 2.2: Graphical illustration of fixed beam exposed to a surface stress deflection of a cantilever with one fixed end and a free end.

2.1.1 Resonant Frequency

In order to find the resonant frequencies for at cantilever it is necessary to solve the Euler-Bernoulli beam equation [36]

$$EI\frac{\partial^4 u}{\partial x^4} + \rho A\frac{\partial^2 u}{\partial t^2} = 0 \tag{2.10}$$

In order to solve the equation it is necessary to set up four boundary conditions:

$$u(0) = 0 \quad \text{and} \quad \left.\frac{du}{dx}\right|_{x=0} = 0 \tag{2.11}$$

$$\left.\frac{\partial^2 u}{\partial x^2}\right|_{x=L} = 0 \quad \text{and} \quad \left.\frac{\partial^3 u}{\partial x^3}\right|_{x=L} = 0 \tag{2.12}$$

The equation can then be solved as done in [37]. The allowed wavenumbers are:

$$cos(c_n L)cosh(c_n L) + 1 = 0 \tag{2.13}$$

So for the first five modes $c_n L$=1.875, 4.694, 7.855, 10.996, 14.137..., and the resonant frequency can be found by:

$$f_n = \frac{(c_n L)^2}{2\sqrt{3}\pi}\sqrt{\frac{k}{m}} \tag{2.14}$$

where m is the mass of the cantilever

2.2 Introduction to Lasers and VCSEL

In order to understand how a VCSEL can be used for measuring the deflection of a cantilever it is useful with a quick reminder of how a normal laser works. A laser consists of a gain medium between two highly reflective mirrors and a power source. The mirrors are shaped so that they form an optical cavity, see Fig. 2.3. As the light passes back and forth between the two mirrors it is being amplified by the gain medium for every pass. By making one of the mirrors slightly transparent, part of the light can escape and the laser beam is emitted through the slightly transparent mirror [38]. For the simple model the gain medium has two levels a ground state and an excited state, corresponding to a low energy level and a high energy level. When a particle decays from the high energy level to the low level the energy difference will be converted into an emitted photon. The energy for the gain medium can be supplied by various sources such as another laser or electrical current. Once excited, the decay to the lower energy can either happen by spontaneous emission, or it can also occur by stimulated emission where a particle will drop from the high energy level to the lower level because of an incoming photon, which will cause it to emit and equivalent photon. The photon will have the same frequency, polarization, direction and phase as the stimulating photon (wave).

If the emitted light is reflected back into the laser cavity, by an external reflector (cantilever), it will effect the performance of the laser. Depending on the distance

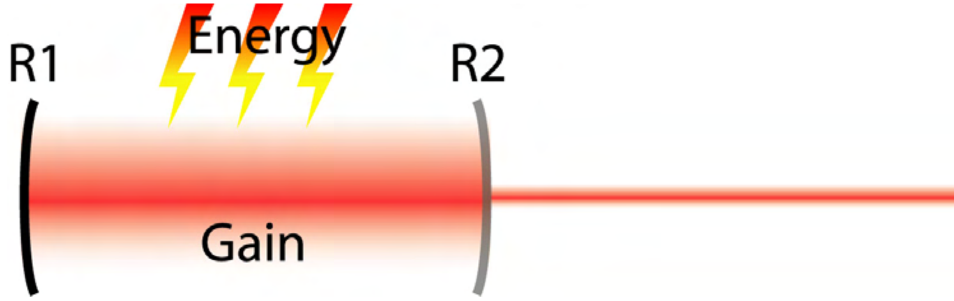

Figure 2.3: This drawing illustrates a simple laser. The optical cavity consist of the two mirrors R1 and R2, R2 is partly transparent allowing part of the light to escape. The gain medium in the cavity amplifies the light. The gain medium is pumped by an external energy source, which could be electrical or another laser.

to the reflector it will either cause constructive or destructive interference. This can be used for sensing purposes to measure the distance to the reflector.
The VCSEL is basically build up like any other laser, however there are some fundamental limitations, as the laser is oriented vertically to the wafer and therefore the entire cavity needs to be epitaxially grown. Therefore, the optical cavity for the VCSEL is considerable shorter than most other laser cavities, which means that the gain needs to be high and the mirrors must have a high reflectivity in order to get significant passes through the cavity to achieve lasing. The mirrors for the resonating cavity are made by Distributed Bragg Reflectors (DBR), and the active gain medium is build up by quantum wells. The DBR consist of peridodic layers of GaAs and $Al_xGa_{1-x}As$, with a spacing of a quater wave length $\frac{\lambda}{4n}$. The combined reflectivity is given by:

$$R = \left(\frac{\left(\frac{n_{AlGaAs}}{n_{GaAs}}\right)^{2N} - 1}{\left(\frac{n_{AlGaAs}}{n_{GaAs}}\right)^{2N} + 1} \right)^2 \tag{2.15}$$

Where n_{AlGaAs} is the refractive index of AlGaAs and n_{GaAs} is the refractive index of GaAs. N is the number of pairs of AlGaAs and GaAs layers. For a VCSEL the two mirrors have a reflectivity of around 99.9% (N=23 pairs) for the bottom mirror and 99.0% for the top mirror (N=17 pairs). In most cases the top mirror is p-doped and the bottom mirror is n-doped forming a diode.
The cavity in a VCSEL is typically the length of a wavelength, so for a VCSEL emitting light at a wavelength of 850 nm. The cavity is around 240 nm due to the refractive index of the cavity material. The active gain region in a VCSEL is a series of quantum wells from 1 and up, usually 3 is used and are placed in the center where the electric field component of the laser light is at a maximum. Depending on the wavelength desired, different materials for the quantum wells can be used, but often InGaAs is used in the quantum wells. The thickness of each quantum well is only around 8 nm, which means that the actual gain region in the cavity is very short. The lateral dimension of the cavity is controlled by an oxidation step in which the diameter is controlled. A typical diameter for a VCSEL is about 3 μm.

2.3 Cantilever Sensing

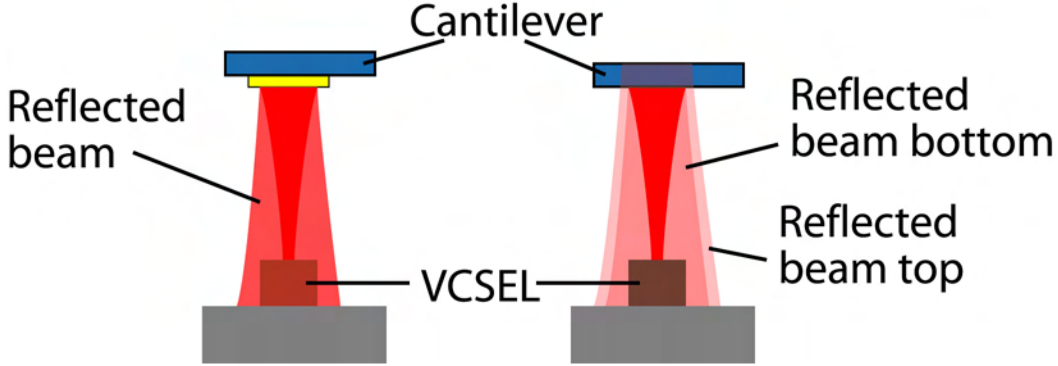

Figure 2.4: Illustration of a VCSEL emitting laser light onto a microcantilever. To the left is a metal coated cantilever which resulting an almost perfect mirror reflecting most of the light back towards the VCSEL. To the right is a microcantilever without a metal coating. Part of the light is then reflected from the bottom and part from the top of the cantilever.

The performance of a laser depends on the two mirrors, but if the emitted light is reflected back into the cavity by an external object it will affect the performance of the laser, see Fig. 2.4. If the reflectivity of the object is known it can be used to calculate the distance to it.
There are three important factors that need to be taken into account. First, the beam has a divergence meaning that it will spread out when it is propagating. Thus, if the reflector is a flat mirror only a fraction of the laser light will be reflected back into the cavity. Secondly, the intensity of the laser beam has a gaussian distribution which also affect the amount reflected. Last, also depending on the distance, the reflected light will be in phase or slightly out of phase resulting in destructive interference in the cavity.
The first part is relative simple as it is a pure geometric factor, see Fig. 2.5. The typical diameter for a VCSEL cavity is on the order of D= 3 μm and the divergence is around θ=11°, the distance to the reflector is denoted z. The power reflected back into the cavity can then be calculated by:

$$Power_R = \frac{D}{D + 2 \cdot (tan(\theta/2) \cdot 2 \cdot z} \tag{2.16}$$

Since the cantilever is not a perfect mirror, the losses need to be taken into account. For a cantilever with a metal coating the power reflectivity is given by R_{metal}, the power reflected back into the cantilever is then given by:

$$Power_R = R_{metal} \frac{D}{D + 2 \cdot (tan(\theta/2) \cdot 2 \cdot z} \tag{2.17}$$

For the cantilever that does not have a metal coating the two interfaces of the cantilever needs to be taken into consideration. For a polymer cantilever made of Topas the power reflectivity of the interface between air and polymer is only

around 0.04. This can easily be calculated now by considering the two interfaces independently. However, now there are two beams being reflected with different paths lengths. Depending on the cantilever thickness t the reflectivity can change from almost zero if $t = \lambda(1 + 2N)/4$ where the reflected beam of the top interface is in destructive interference with the reflected beam from the bottom interface. For $t = \lambda N/2$ the reflection of the two interface are in phase and the cantilever reflection is maximized.

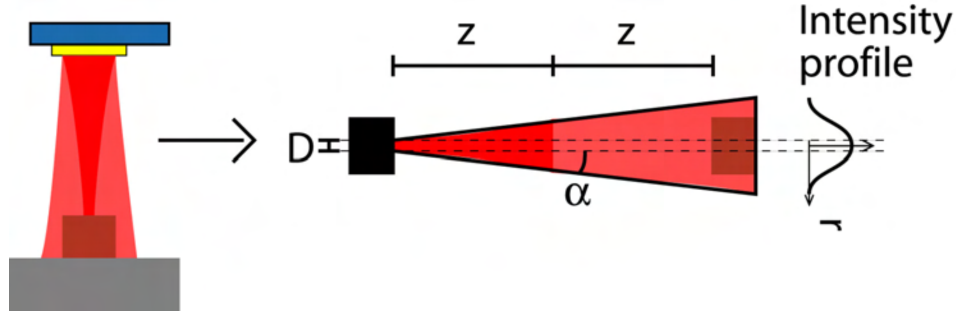

Figure 2.5: Illustration of the geometry behind the calculations of the laser being reflected back into the cavity. The divergence of the cantilever is $\theta = 2\alpha$. z is the distance between the VCSEL and the cantilever.

The power is not uniform across the beam, but expresses a gaussian intensity profile which can be written as:

$$I(r) = e^{-\frac{r^2}{\omega_0^2}} \tag{2.18}$$

where r is the position along the radius and ω_0 (D/2) is the radius of the VCSEL. The part which is reflected back into the cavity of the VCSEL is the center part of the beam where the intensity is the highest, as shown in Fig. 2.5.
For a VCSEL with the chosen values the reflected percentage as a function of distance is plotted in Fig. 2.6, for both the purely geometrical consideration and including the gaussian beam profile. When including the beam profile a higher percentage is reflected back into the laser as the sides of the beam with a lower intensity are being lost.

2.4 Interference in a VCSEL

The analysis of how the lasing is affected by the laser light being coupled back into the laser is not straight forward. Hsu *et al.* has studied this phenomenon for a laser being coupled into a fiber which is in close resembles with the case of a laser since we are just looking at the light being reflected back from the fiber and back into the laser [39]. They find the output power ($P_{out,th}$) to be given by:

$$P_{out,th}(z) = \eta_d(z)\frac{\hbar\omega}{q}(I - I_{th}(z)) \tag{2.19}$$

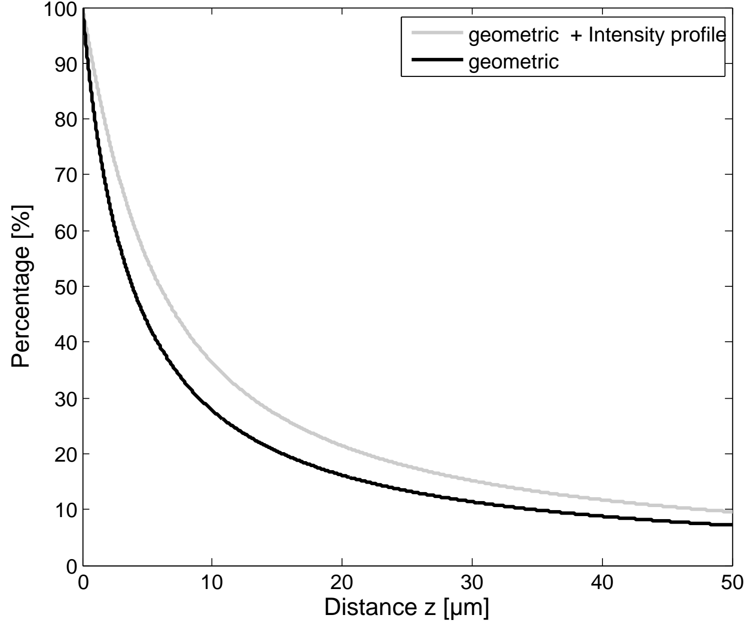

Figure 2.6: Graph showing the calculated percentage of the reflected beam from a perfect flat mirror (R=1). For small distances, below 10 μm, the change is very large, but for longer distances the effect is greatly reduced, and therefore not useful at longer distances. The Matlabscript is shown in App. C.

where $\eta_d(z)$ is the differential quantum efficiency as a function of z, $\hbar\omega$ is the photon energy, q is the elementary charge, I is the current supplied to the laser and $I_{th}(z)$ is the threshold current for a given z position. The threshold current is:

$$I_{th}(z) = I_{th,o} exp\left(\frac{\Delta g_{th}(z)}{g_o}\right) \tag{2.20}$$

where $I_{th,o}$ = 4.62 mA and g_o is 3300 cm^{-1}, both are parameters for the VCSEL without reflection. The Δg_{th} is found in [40].

$$\Delta g_{th} = -\frac{\xi}{d} cos(\phi_{ext}) \tag{2.21}$$

$\phi_{ext} = 4\pi z/\lambda$, d is the length of the laser cavity which is 1.4 μm (including part of the DBR as the laser is not reflected of the first interface), and ξ denotes the coupling effect from the external reflector back into the laser cavity:

$$\xi = (1 - R_2)\frac{r_3}{r_2} \tag{2.22}$$

where R_2 is the power reflectivity of the top DBR mirror, r_3 is the reflectivity of the cantilever and r_2 is the reflectivity of the top DBR in the VCSEL.
The differential quantum efficiency $\eta_d(z)$ is given by:

$$\eta_d(z) = F(z)\eta_i \frac{\alpha_m(z)}{\Gamma g_{th}(z)} \tag{2.23}$$

Considering a small internal loss, then $\frac{\alpha_m(z)}{\Gamma g_{th}(z)}$ can be approximated to 0.9, and the internal quantum efficiency η_i to 0.9 [39]. $F(z)$ can be calculated by

$$F(z) = \frac{T_{eff}(z)}{(1 - R_{eff}(z)) + \sqrt{\frac{R_{eff}(z)}{R_1}}(1 - R_1)} \tag{2.24}$$

where R_{eff} and T_{eff} are the effective power reflectivity and transmissivity from the top DBR, while R_1 is the bottom DBR power reflectivity which is around 0.999 for a VCSEL. The effective power reflectivity can be calculated from [41]:

$$R_{eff} = R_2(1 + \xi_r^2 + 2\xi_r cos(2\pi z/\lambda)), \tag{2.25}$$

where $\xi_r = \frac{r_3}{r_2}$
It is now possible to calculate the output power of the VCSEL as a function of the cantilever position, see Fig. 2.7. The calculation does not include the change in reflected percentage calculated in the previous section, but for the distances of 50-53 μm the effect is minimal, see App. C for the detailed calculations. Fig. 2.7 also illustrates the biggest drawback with this readout technique. Ideally, one output power should correspond to one position so the position is precisely known. However, this can only only be achieved for small displacements on the slopes between extremum points. For larger displacements, passing through a maximum or minimum the sensitivity would drop to zero in these regions and it would be difficult to interpret from the power output in which direction the cantilever is moving, if only relying on the VCSEL readout. For ideal operation the current input should be close to the threshold current, where the greatest change in output power will occur.
By using this readout technique the system can be made very compact, and it is possible to detect the deflection of the cantilever with a small spacing equivalent to the spacing of the VCSEL, which is typically 250 μm distance.

2.5 Summary

To summarize this chapter the important theory behind the mechanics of a cantilever and the novel readout technique has been discussed. Since the major part of this project is concerning cantilever sensing, the basic mechanics behind a cantilever with respect to end-point deflection, surface stress sensitivity and the resonant frequency has been be described. It has been illustrated how the thickness can be around 10 times thicker for a polymer cantilever and still achieve the same sensitivity as a silicon based cantilever for static measurements. The second part explained the basic behind the VCSEL used in the project. Then the theory behind the self-mixing was described and, the advantages and disadvantages of this technique were illustrated.

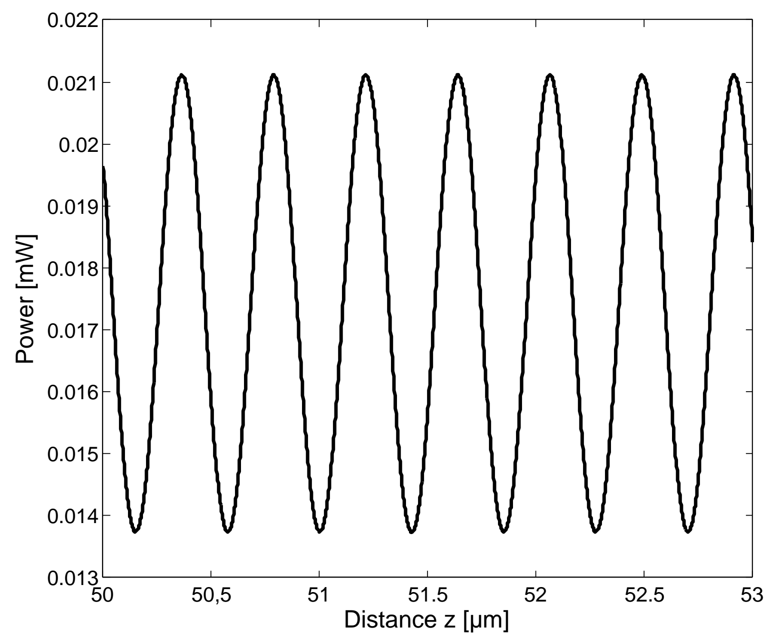

Figure 2.7: This graph shows the changes in output power as a function of the cantilever displacement. The highest sensitivity is achieved where the slope is the highest. That is between a maximum and a minimum.

Chapter 3

Design

This chapter will introduce the design of the cantilevers for the project. The cantilevers are to be fabricated by NanoImprint Lithography (NIL), and therefore the chapter will start with a short introduction to the field, which then will lead to a possible design of the cantilevers. Since it is new to fabricate cantilevers by NIL the different advantages and disadvantages will be presented and discussed. NIL has the advantage of being able to make more complex structures on the cantilevers, but it is a challenge to fabricate free standing structures by NIL.

3.1 Nanoimprint Lithography

The term Nanoimprint Lithography is first mentioned in the mid nineties [42]. The process it self is not completely new as it can be considered an evolution of known techniques, such as printing, embossing and molding. The process is basically just to heat and press a hard stamp into a soft material, and thereby replicating the negative structure into the soft material. The process is therefore not novel, but the application of the technique as a lithographic technique for IC (Integrated Circuit) is new. Currently, the 45 nm technology is being produced by photo lithography with a wavelength of 193 nm. By itself it is a tremendous achievement to fabricate features at one fourth the size of the wavelength [43]. This has only been possible due to highly optimized designs, optics and resists. It is even possible to produce a 157 nm source. However, due to the higher energy of the photons, the tricks developed for 193 nm can not be applied. The price for these lithography machines is on the order of 40 M€and the cost of a mask is around 400 k€, increasing for every generation. Therefore NIL it still considered as one of the potential technologies for the IC industry by around 2020 by International Technology Roadmap for Semiconductors [44]. Since NIL is basically such a simple process the machines are considerably cheaper; on the order of 1 M€. The stamps or "masks" for NIL might become expensive depending on which structures need to be reproduced. Since NIL was first introduced as a technology for the IC industry the main focus in the beginning was targeted on fabricating nanometer sized features and on trying to replicate them over a large diameter wafer [45, 46].

However, NIL can also be used for other application where it is of interest to fabricate structures down to micro and nano meters in polymer. Miniaturized lab on a chip (LOC) system requires precis control of fabricated structures in compatible materials. NIL is a prime candidate for fabricating these structures, and it can be directly transferred to thermoplastics [47]. NIL might also simplify and reduce the cost of fabricating existing product like polarizers [48].

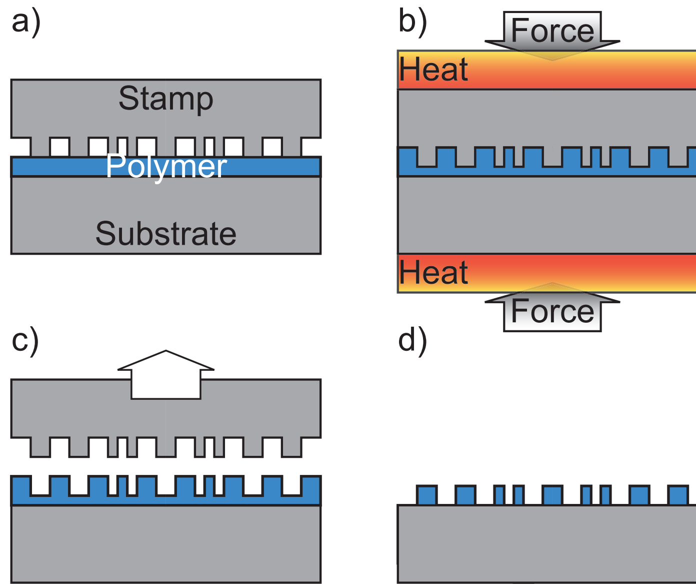

Figure 3.1: Illustration of the NIL process. a) This is the starting point, with the substrate coated with a thin polymer film, and a prepared stamp. The substrate and the stamp are placed together inside the NIL machine and evacuated. b) The stack is then heated and at the desired temperature well above T_g the force is applied for the time necessary to perform the imprint and to achieve complete filling of the stamp. c) Then the stack is cooled down again and once below the T_g the stamp and the substrate can be released, and the structures from the stamp have been transferred to the polymer. d) The last step is to etch the residual layer, which is usually done in an oxygen plasma in a anisotropic manner in the RIE in order to damage the structures as little as possible.

The basic NIL process is illustrated in Fig. 3.1. First, a substrate is coated with a thin polymer film. If necessary the substrate is pretreated to improve adhesion of the polymer. The treatment could be a simple baking step, removing moist from the surface. The stamp is fabricated by standard silicon processing techniques, and coated with an anti-stiction coating to ensure a good release between the polymer and the stamp. The substrate and the stamp are placed face to face and mounted inside a NIL machine, which is then evacuated. The stack is heated and at the desired temperature, well above glass transition temperature T_g of the polymer a force is applied for the time necessary to perform the imprint. The temperature, time and pressure are determined by the polymer and the structures on the stamp. After complete filling of the stamp, the stack is cooled down again and once below the

T_g the stamp and the substrate can be released, and the structures from the stamp have been transferred to the polymer. The final step is to remove the residual layer, which is the thin layer left below the protrusion in the stamp. Due to the fluidic dynamics during imprint, it is not possible to avoid a residual layer formation. The residual layer is usually removed by an oxygen plasma etch in a anisotropic manner in a reactive ion etch (RIE) in order to damage the structures as little as possible. For some application this step can be avoided which is desirable, since it also saves time. By switching to a silicon etching recipe in the RIE the polymer pattern can then be used to transfer the pattern to the silicon [47]. It is also possible to evaporate metal after the oxygen etch and subsequently dissolve the polymer, performing a liftoff process to produce a metal pattern on the substrate [42].

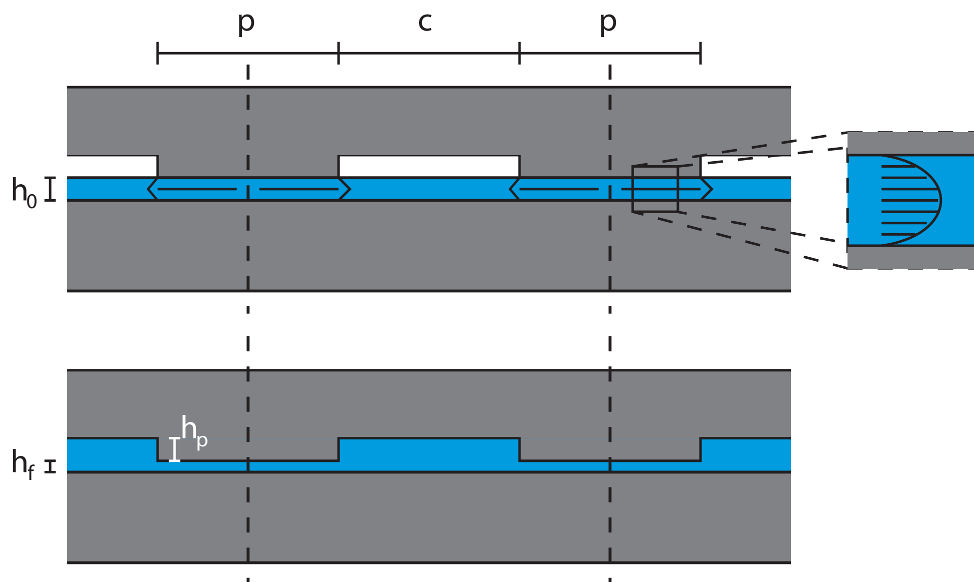

Figure 3.2: Illustration of the polymer flow during the imprinting process. The top is before the imprint and the bottom is after. Before the imprint the polymer has a thickness of h_0. As the protrusion (p) starts to push the polymer, the resulting flow has a parabolic profile. After the imprint, the cavity (c) is filled, and there is a residual layer of thickness h_f left. The protrusions have a hight of h_p.

It is during the imprinting process, that the pattern is transferred. What happens is basically just a redistribution of the polymer material. For NIL, the polymers of interest are usually thermoplastics, but thermoset polymers can also be used. Thermoplastics have a glass transition temperature T_g which relates how the polymer responds to stress. Below T_g, the deformation of the polymer is primarily due to elastic deformation, and the polymer will most likely return to its original position. Above T_g, local motion of polymer chains take place and therefore the modulus of the polymer drops by several orders of magnitude. The overall polymer chain network remains. Thus the polymer is likely to return to its original position once the pressure is released. By increasing the temperature further to T_f, a liquid flow

state is reached, and it is in this regime NIL patterning can take place. At this temperature irreversible movement of entire chains occur and therefore the pattern will be retained also after release of the stamp. Moreover, the modulus viscosity of the polymer is further reduced making it easier to redistribute the polymer [49, 50]. The redistribution of the polymer takes place as a squeeze flow which can be described by fluid dynamics theory. In the beginning of the imprinting process, the flow of the polymer takes place below the protrusions. Since the polymer is heated to T_f it behaves as liquid, and can be assumed to be an ideal viscous, incompressible Newtonian liquid, as illustrated in Fig. 3.2. Considering a stamp with periodic structure $(c - p - c - p..)$ as illustrated, it is simple to write up an equation for the polymer distribution before and after the imprint. Before, the polymer has the thickness of h_0. (The distance $c+p$ is one periode.) After the imprint the cavity has been filled, with a cross sectional area of $c \times h_p$, the residual layer adds an area of h_f over a periode, since it is present below the protrusion as well as the cavity.

$$h_0(c+p) = h_f(c+p) + h_p c \tag{3.1}$$

To fill an entire stamp it is just needed to do a summation over the entire stamp. The final residual layer can then be calculated to:

$$h_f = h_0 - h_p \frac{c}{c+p} \tag{3.2}$$

The necessary time to complete an imprint is very dependent on the size of the protrusions. The time to fill t_f the structure is found to be [51]:

$$t_f = \frac{\eta_0 p^2}{2P} \left(\frac{1}{h_f^2} - \frac{1}{h_0^2} \right) \tag{3.3}$$

where η_0 is the viscosity of the polymer during imprint, P is the applied pressure during imprint. There are two important factors to notice in this equation, on which the imprint time is heavily dependent. First, the imprint time is related to the protrusion by p^2, and the residual layer is linked by $\frac{1}{h_f^2}$, meaning that as the residual layer goes towards zero the imprint time goes towards infinity, or until the cavities are completely filled when the flow stops. The actual flow of the polymer during the imprinting process is more complex and will not be covered in this thesis [52].
There are many other types of NIL than the thermal NIL considered for this work. Many initiatives try to reduce cost and size of the machines for the process. As an example, heaters can be implemented into the stamp [53]. For high volume production a roll-to-roll technique has been proposed, where the stamp is on a roller and the substrate moves continuously thereby the speed can be increased [54]. NIL is not limited to thermoplastics. By using a transparent stamp the pattern can also be transferred to UV-curable monomers [55]. The advantage of UV NIL is that the polymer often has a lower viscosity thus reducing the time needed to redistribute the polymer and the temperature cycle can be avoided. This process can also be used in the roll-to-roll technique [56].

3.2 Design Consideration for NIL

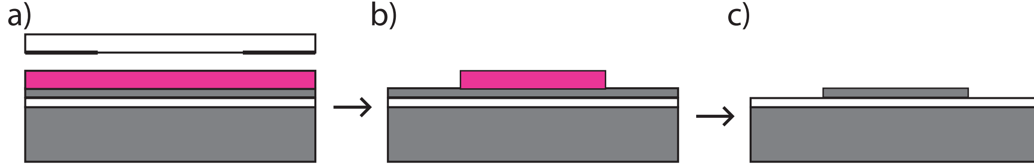

Figure 3.3: Schematics of a normal fabrication scheme for defining a cantilever structure in silicon on a SOI wafer. a) SOI wafer with UV resist and the UV mask. b) After development of the resist. c) The structure has been transferred to the silicon device layer by an etching process and the resist has been removed.

Traditionally, when designing the masks for fabrication of microcantilevers, the defining step will look similar to Fig. 3.3. There is a layer, in this case a device layer on an SOI wafer, where the cantilever needs to be defined. A layer of photo resist is spin coated onto the wafer, and exposed through an UV mask. After the development of the resist, the desired area is covered by resist and the pattern can be transferred by an etching process such as RIE. The resist is removed and the cantilever is now defined in the device layer, and ready to be released.

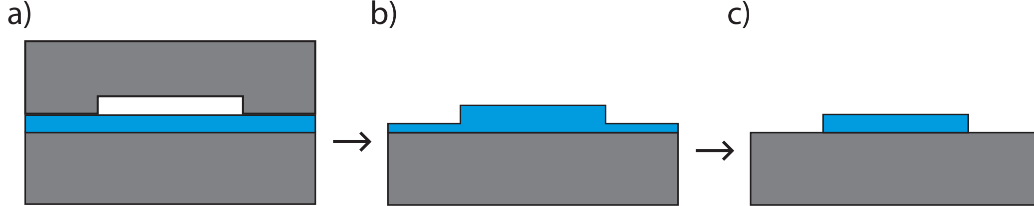

Figure 3.4: The process flow for fabrication of a polymer cantilever by NIL with same design as Fig. 3.3. a) A substrate is coated with the desired polymer and the stamp is placed on top ready for imprint. b) After the imprint the stamp is removed. c) The residual layer is removed by an oxygen etch.

The same design can be applied for fabricating the cantilevers by NIL. The process flow is illustrated in Fig. 3.4. The stamp is fabricated in silicon using the same mask. An anisotropic RIE to the desired depth defining the cantilever thickness. The stamp is then imprinted into a polymer film and the residual layer etched. As discussed in the previous section the design of the stamp is of great importance to the quality and simplicity of the imprint process. Since it is necessary to remove the residual layer to define the cantilever it is desirable to have a minimum thickness in order to reduce the etching time which might potentially damage the cantilever. Microcantilevers used for static sensing applications most often have a width of 100 μm and a spacing of 150 μm [22]. This will make the protrusion p =150 μm wide and the cavity equal to c =100 μm. If we now consider to imprint a cantilever with a thickness of $h_p = 5$ μm and a desired residual thickness of h_r =0.1 μm. In PMMA

with a molecular weight of 75k, and with a viscosity of 2648 Pas at 250 °C and at a pressure of 3.6 10^6 Nm^{-2} [51]. The imprint time can be calculated to:

$$t_f = \frac{2648(150 \cdot 10^{-6})^2}{2 \cdot 3.610^6} \left(\frac{1}{(0.1 \cdot 10^{-6})^2} - \frac{1}{(2.1 \cdot 10^{-6})^2} \right) \text{ s} = 826 \text{ s} \tag{3.4}$$

which is almost 14 min. If one wants to reduce the residual layer thickness to 50 nm it takes 3308 s or 55 min.

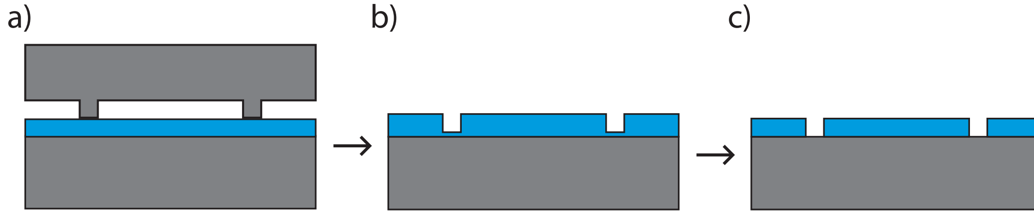

Figure 3.5: The process flow for fabrication of a polymer cantilever by NIL with an optimized design. a) A substrate is coated with the desired polymer and the stamp is placed on top ready for imprint. b) After the imprint the stamp is removed. c)The residual layer is removed by an oxygen etch.

A more intelligent design would be to reduce the protrusion length to a minimum and thereby reducing the time. Instead of imprinting the entire area around the cantilever, the idea is to only imprint the outline of the cantilever like a cookie cutter. For a side view of the process, see Fig. 3.5. For the same desired cantilever, but now with a protrusion width of 15 μm, the imprint time can be reduced to:

$$t_f = \frac{2648(15 \cdot 10^{-6})^2}{2 \cdot 3.610^6} \left(\frac{1}{(0.1 \cdot 10^{-6})^2} - \frac{1}{(4.35 \cdot 10^{-6})^2} \right) \text{ s} = 8.27 \text{ s} \tag{3.5}$$

Which is 100 times shorter, and consequently it is possible to achieve a much thinner residual layer without a very long imprint time.

Until now only the design of the cantilever has been considered which consist of lines. There is however not much to be added. Only a line at the apex of the cantilever and an outline of cantilever support. Fig. 3.6 shows how the design for a mask looks for both the normal UV design and for the optimized NIL design. The top view illustrates that the highest concentration of protrusion area is found around the cantilever. It will therefore be in this area that the cavities in the stamp are filled the fastest, while in the center it will take longer to achieve a complete filling. It is however not important that the center is filled completely for a successful outcome of the device. It can actually be an advantage as there will always be some variation in the polymer thickness across the wafer and these large cavity areas can act as buffer zones, being filled in the areas where there are slightly more polymer and not filled in the areas with less polymer. A more homogenous thickness of the residual layer across the wafer can then be achieved.

For the final design of the imprint mask, the protrusion coverage is 6.4 % around the cantilever, and 2.3 % for one entire chip including the spacing around the chip,

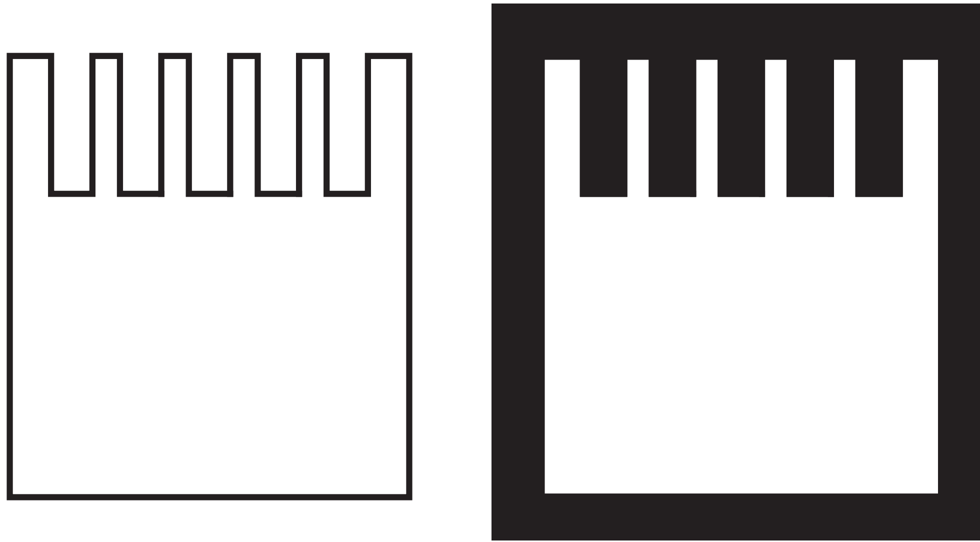

(a) Mask design of the optimized NIL design. (b) Mask design for a UV process.

Figure 3.6: The two figures clearly illustrate the difference between area needed to imprint depending on the two designs. This is just a small graphical representation of the design. The actual design has 8 cantilevers and the mask layout is shown in App. D.

so the same percentage for the entire wafer. The widest feature 15 μm to keep the imprint time as short as possible and to have a very thin residual layer. One could go for thinner structures than 15 μm, but it proved difficult to detect and ensure that the residual layer was removed during processing. Being able to use a profilometer to measure the residual layer is highly desirable as this is a very fast technique. Furthermore, a width of 15 μm also facilitates optical inspection of the residual layer as a color at the bottom of the imprinted protrusion.

3.3 Free Standing NIL Structures

The cantilever needs to be released in order to be able to work as a sensor. The literature contains very few studies on free standing polymer structures fabricated by NIL. This is partly due to the fact that NIL is intended as a lithographic pattern transfer technique and most other applications are trying to keep the polymer fixed on the substrate . There has however been made some smaller bridges, see Fig. 3.7 [57]. The fabrication of these structures is made by Reverse NIL (RNIL) where the polymer is spun onto the stamp and then transferred to an underlying substrate containing a gap. For gaps larger than 10 μm Polycarbonate (PC) for the bridges is not transferred, as the stiction to the stamp is too large. These structures are however very short and clamped at both ends, and would not work for our purpose. Furthermore they are not accessible from both sides as they are placed on top of a substrate, which will disturb the proposed readout technique Sec. 2.3.
Looking at the fabrication schemes for polymer based cantilevers, the work by Keller

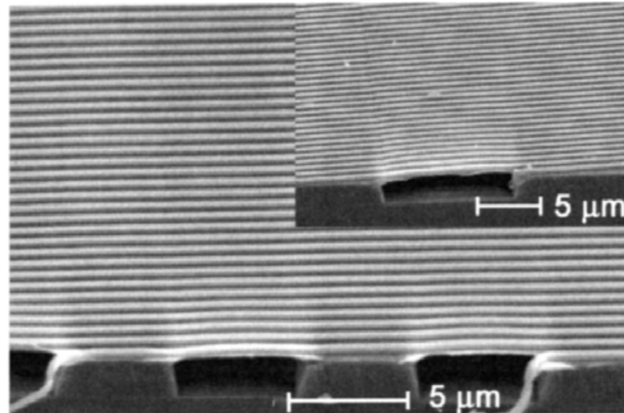

Figure 3.7: The largest free standing structures of 10 μm PC bridges. The bridges are fabricated by reverse NIL, as the polymer is spin coated onto the stamp and then transferred to the substrate, the substrate contains the grooves that makes the holes under the bridges [57].

et al. could potentially work for NIL fabricated cantilevers, see Fig. 3.8 [58]. The cantilever is fabricated in SU8 on top of a Fluorocarbon (FC) coating which has been optimized to have sufficient stiction to allow for spin coating of polymers on top of the FC coating but it still allows the cantilevers to be released after processing. The idea is to replace the thin SU8 with a thermoplastic polymer. Next, the cantilever support structure is realized in SU8 using UV-lithography. The potential problem with this techniques is that the polymer might end up on the stamp since there are many surface structures and small roughnesses due to the processing of the stamp.

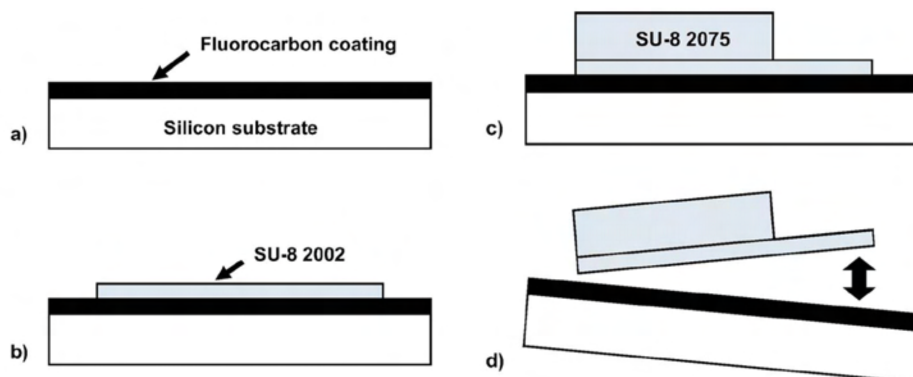

Figure 3.8: Illustration of the process flow for SU8 microcantilevers. The FC coating is deposited, the thin SU8 layer for the cantilever is patterned and a thick support structure of SU8 2075 is defined so the cantilever can be lifted of the wafer [58].

For this to succeed it is important to have a good anti-stiction coating on the stamp. Various ways have been tested to coat and prepare stamps for the imprinting process. The first studies exploited the bulk properties of the stamp. For PMMA, for example, the adhesion is stronger to silicon than to silicon dioxide which the stamp was made

of [42]. In later experiments different coatings such as PTFE and FC have been developed for the stamp [59, 60, 61]. However, since FC is also used for the release of the cantilever this is unlikely to work. In order to evaluate the performance of a coating the contact angle with water is often measured, see Fig. 3.9. Presently, the best coating seems to be achieved by $-CF_3$ groups, achieving a contact angle of 119° corresponding to a free energy of 6.7 mJ/m^2 on a glass surface [62]. In order to apply this to a silicon stamp by vapor deposition, the chemical composition of FDTS ($Cl_3Si(CH_2)_2(CF_2)_7CF_3$) has proven effective achieving a maximum contact angle of 120° under optimized conditions [63]. The exact process of how these layers are formed will be explained during the description of the fabrication in Chap. 4.

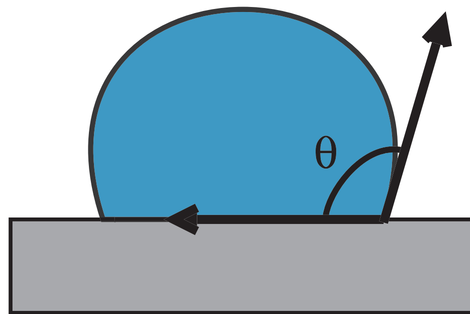

Figure 3.9: Illustraion of how to measure the contact angle between a water droplet and a surface. The FDTS coating has a contact angle close to 120°, while the FC is slightly lower at 110°.

Using the contact angle to measure the surface energy is not perfect or ideal, since the mask and substrate surfaces are very different. The substrate is flat as it has been polished in the manufacturing process. The stamp is structured by different etching processes which has altered the surface roughness. This can also give a rise in the contact angle, but it is not beneficial for the release process. However since it was found from Billenberg *et al.* that the FDTS coating performes better than the FC coating there is a chance it will work [60].

3.4 Advanced Structures

NIL also has other advantages to normal lithography. Most lithographic techniques only allow for defining a pattern on a surface thus only 2D, or $2\frac{1}{2}$D including etching. NIL will transfer any pattern defined in the mask, as long as there are no undercut in the structure to complicate the release process. It has been shown that structuring the surface of a cantilever can result in an increase in signal response by approximately 4.5 times in static mode [64, 65]. These types of structures can be incorporate into the stamp and then transferred to the cantilever. By adding another UV mask step to the fabrication of the stamp, the surface structures can be included in the stamp. These two masks are shown in Fig. 3.10. The idea is to increase the bending

response, but since the cantilever is already bending it is difficult to quantify how much of the increased signal is from the structure and what is from the thinning of the cantilever. One way of investigating this is to orient the ripples at and angle on the cantilever. By having a 45° between the cantilever and the ripples, the ripples should not only add to the bending, but also twist the cantilever in the direction of the ripples.

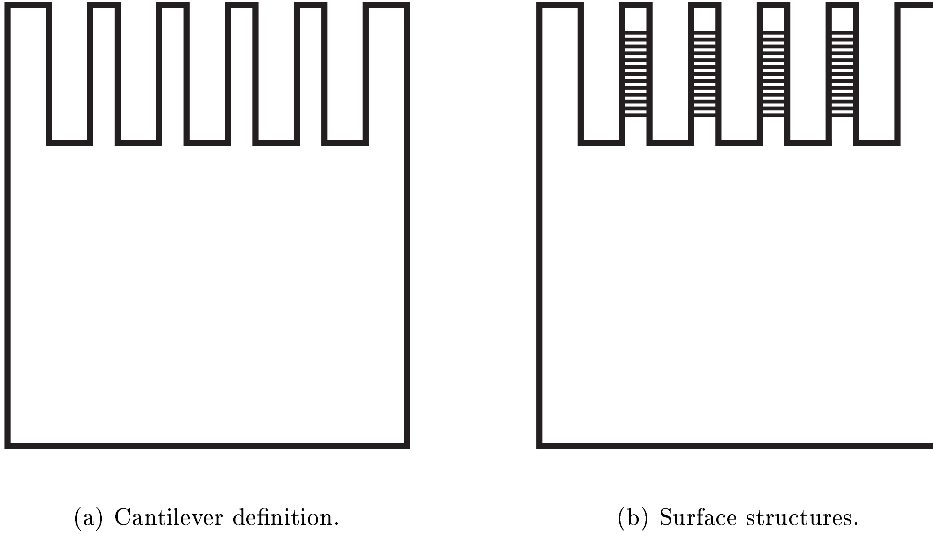

(a) Cantilever definition. (b) Surface structures.

Figure 3.10: The two masks needed for the fabrication of the stamp with surface structures. Once the stamp is made, both patterns will be transferred together in the process thus reducing the number of lithography steps from two to one.

Using the masks the side view of a cantilever would look similar to Fig. 3.11(a). This structuring gives rise to an increase in surface area as well, which should also help to increase the signal in the dynamic mode.

NIL is not limited to producing $2\frac{1}{2}$D structures, if other shapes are added to the stamp they will also be transferred. In microfabrication structures are usually made of different layers which are defined by more or less vertical etches just changing the profile during the etch. Sloped side walls can be achieved by performing etches which are selective to different crystal planes, but then the angle and geometry is still limited by the crystal lattice. FIB can be used to produce more advanced structures as shown in Fig. 3.11(b). Such structures are however too expensive to produce for any commercial application as the FIB is very time consuming and expensive. However, when producing the cantilevers by NIL, the structures can be produced by FIB in the stamp and then transferred to the cantilever in the imprinting process. Since the stamp is used many times, it is not a problem for the price and process time. For the fabrication of the cantilever the process is exactly the same no matter if there is surface structures or not.

Since the FIB is not limited by crystal planes also other angles can be produced.

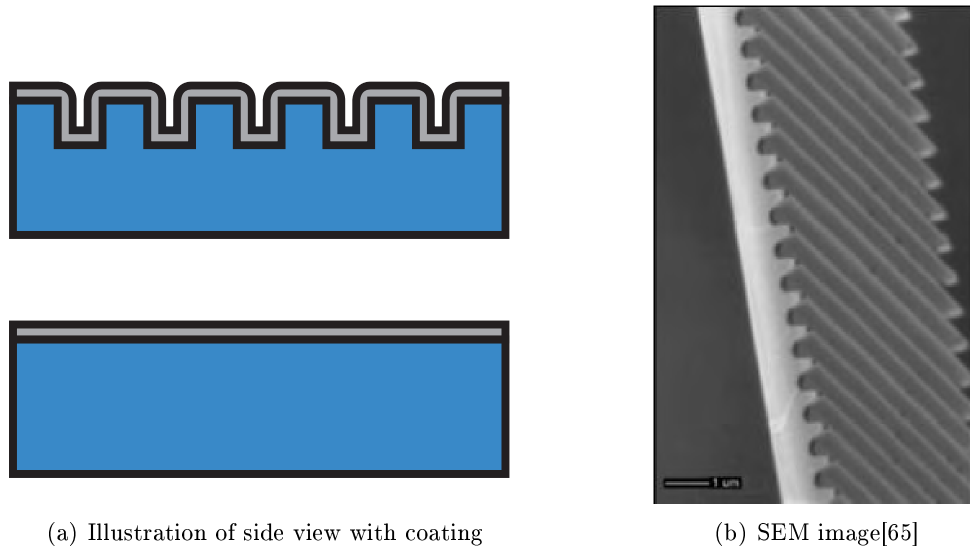

(a) Illustration of side view with coating (b) SEM image[65]

Figure 3.11: a) shows the illustration between having a flat cantilever and a rippled cantilever surface with a polymer coating on. b) Is a SEM image of the silicon cantilever where ripples are introduced by FIB [65].

As discussed in Sec. 2.3 it can be a problem to achieve a good sensitivity of the bare polymer as the reflectivity is low. By implementing a reflector, consisting of 45° angles, the laser light will be reflected when passing through the polymer, as the polymer of interest has a refractive index of 1.52 [66]. The design is illustrated in Fig. 3.12 where the top side of the cantilever has the grating.

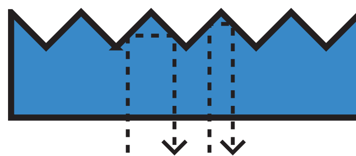

Figure 3.12: Illustration of reflective structure. By having a sawtooth structure with an angle of 45° the laser light should be 100 % reflected, without the need for metallization.

3.5 Complete structure

The final chip will need a support structure for the cantilever. When the finished cantilever is placed on a FC layer the easiest way to release it will be to follow the example by Keller *et al.* Here a body chip is defined in a 300 μm thick SU8 layer, which facilitates simple removal by tweezers [58]. One concern is how strong the adhesion between the SU8 and the imprinted polymer will be. For readout purposes

a reflective metal pad at the apex of the cantilever could be necessary. The easiest would be to perform a lift-off process of a metal layer after the NIL step and before fabricating the support structure in SU8. A graphical illustration of the finished chip is shown in Fig. 3.13. The final chip will have 8 cantilevers and two SU8 protection bars on either side, the masks are shown in App. D. The thick SU8 layer will also have periodic holes to help with the stress release in the support structure.

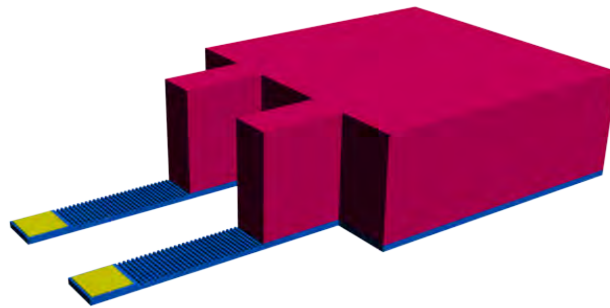

Figure 3.13: Illustration of finished cantilever chip. The cantilever will be made of a thermoplastic material, and the support is made in SU8. Metal pad at the apex will improve the reflectivity and the readout.

3.6 Summary

In this chapter the NIL process has been introduced, some of the advantages and disadvantages have been discussed. The optimal mask design for fabricating cantilevers by NIL, has been introduced and quantified. The challenge of releasing the cantilever was also presented and possible solutions were discussed. By fabricating cantilevers by NIL, some advantages are achieved as structures can be implemented into the stamp and replicated to the cantilever without adding complexity to the fabrication.

Chapter 4

Fabrication

In this chapter the fabrication of cantilevers by NIL will be presented. The fabrication of the stamp will first be introduced as a separate part since it can be reused several times during the fabrication of the cantilevers which are presented in the following section. Several challenges were encountered during the fabrication, and the most crucial ones are discussed, as well as other process sequences which were tried during the time of the project. Finally, the possibility of using FIB to produce sloped sidewalls on the cantilever was tested.
The stamp is made of silicon and coated with an antistiction coating. The cantilever itself is structured by NIL in Topas whereas the support structure is defined in SU-8 by UV lithography. After processing, the chip can simply be lifted off the supporting substrate by a pair of tweezers. This is possible since the substrate is initially coated with an FC layer. An antistiction coating on the stamp ensures that the Topas remains on the FC layer after the imprinting process.

4.1 Fabrication of Stamp

The stamp is fabricated by standard silicon processing, UV lithography, anisotropic dry etching and thermal oxidation. The finished stamp can then be coated with an antistiction coating, a graphical overview is presented in Fig. 4.1.
The starting point is a single crystal 4" Si (100) wafer, see Fig. 4.1(a). The first step is included to illustrates the possibility of structuring the surface of the cantilever, as discussed in Sec. 3.4. A short etch is used to realize micrometer sized ripples at the bottom of the stamp. The lines have a pitch of 4 μm and are initially defined in standard UV photoresist. The lines are transferred to the substrate by a shallow anisotropic Reactive Ion Etch (RIE) (SF_6: 31 sccm, O_2: 9 sccm, pressure: 80 mTorr, power: 35 W) for 2.5 min. which result in a depth of 800 nm, see Fig. 4.1(b). If flat cantilevers are desired this step can be skipped. A second RIE step with the same process parameters but for a longer time of 15 min. is the performed. This results in an etch depth of 4 μm, see Fig. 4.1(c). This etch defines the cantilever by the protrusion created, it will imprint the outline of the cantilever and support area. Depending on how perfect the RIE is running there can be some surface roughness

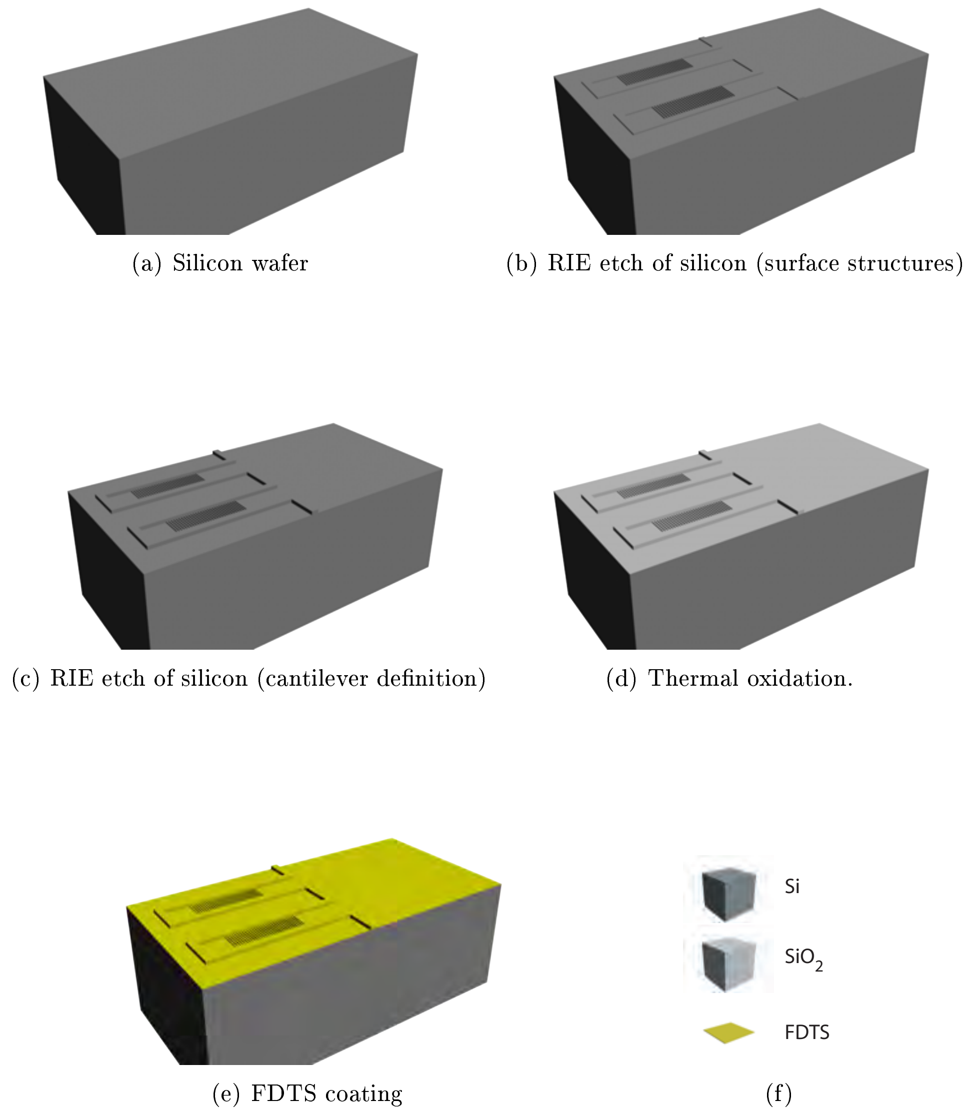

(a) Silicon wafer

(b) RIE etch of silicon (surface structures)

(c) RIE etch of silicon (cantilever definition)

(d) Thermal oxidation.

(e) FDTS coating

(f)

Figure 4.1: Graphical illustration of the process sequence for the stamp. a) The starting point is a silicon wafers (100), b) the first etch defines the surface structures and c) the second etch defines the outline of the cantilever. d) An oxidation step smoothes the stamp and is removed again before the e) FDTS coating is applied.

after the etch. By adding an oxidation step this roughness can be minimized [61]. The roughness is reduced because the oxidation process is a reaction with the silicon of the stamp. The roughness is basically caused by small tips on the surface. These will be oxidized from both the top and sides and the oxidation from the sides will slowly reduce the silicon tip [61]. Before the stamp can be placed in the oxidation

furnace it needs to be cleaned by a standard RCA clean. The oxidation process is a wet thermal oxidation for 90 min. at 1000 °C which results in an oxide thickness of 475 nm measured by ellipsometry. The oxide is removed again by an oxide etch (BHF) for 8 min.
Before the stamp can be used it needs to be coated with a good antistiction coating. As discussed in Sec. 3.3 this is a very critical step, the most effective antistiction coating was found to be a FDTS coating, due to its structure and covalent binding to silicon [60, 63]. The coating is deposited using a molecular vapour deposition (MVD) system (MVD-100, Applied Microstructures Inc.). The silicon surface is first activated by an oxygen plasma which creates hydroxyl groups on the surface. Next, a conformal monolayer is formed by letting a chlorosilane based precursor (1H,1H,2H,2H-perfluorodecyltrichlorosilane, FDTS) react covalently with the hydroxyl groups on the silicon surface, see Fig. 4.1(e). The self-assembled monolayer increases the surface energy of the stamp to a contact angle of 120° for water, thereby preventing the adhesion of Topas to the stamp during the imprint process. If the FDTS coating starts to wear off, then a new layer can be applied, by first stripping the coating by a high power oxygen plasma and then running the coating process again.
SEM images of the stamp can be seen in Fig. 4.2. Fig. 4.2(a) shows the full array of eight cantilevers for imprinting, and Fig. 4.2(b) is a SEM of the top end of a cantilever with ripples. The apex of the cantilever does not have ripples to allow for the optical readout.

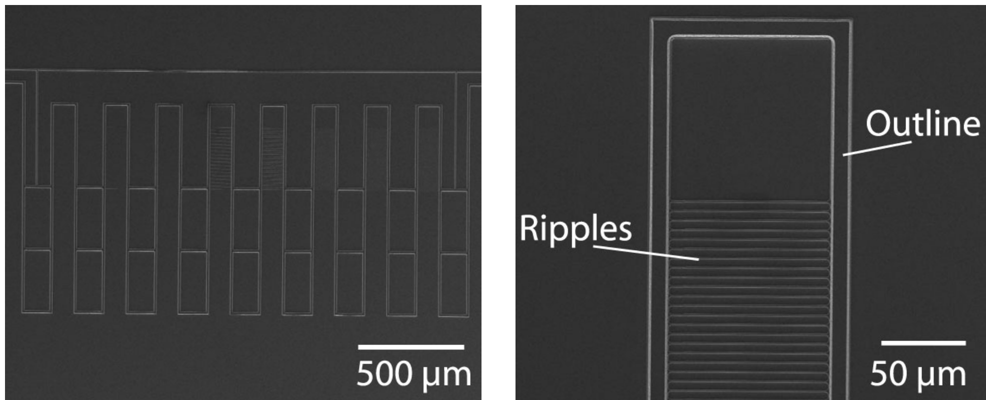

(a) SEM image of stamp for imprint of cantilever array.

(b) SEM image of the stamp with close up of the tip of a cantilever.

Figure 4.2: These SEM pictures show a top view of the stamp. a) Shows the full cantilever with eight cantilevers with surface structures and on both sides are included an area which will be the protection bar. b) Is a SEM image of the tip of the cantilever stamp. The two parallel white lines shows the protrusion for the outline of the cantilever. While the array of the horizontal lines defines the surface structure.

The protrusion height is defined by the RIE, therefore there is a height variation across the wafer, see Fig. 4.3. In the centre of the wafer the etched depth is only 4.87 μm while at the edge it is up to 5.39 μm, resulting in a variation of 520 nm with a

parabolic profile. The parabolic etch profile is known to originate from variations in the electric field gradient and loading effects in the RIE system [67].

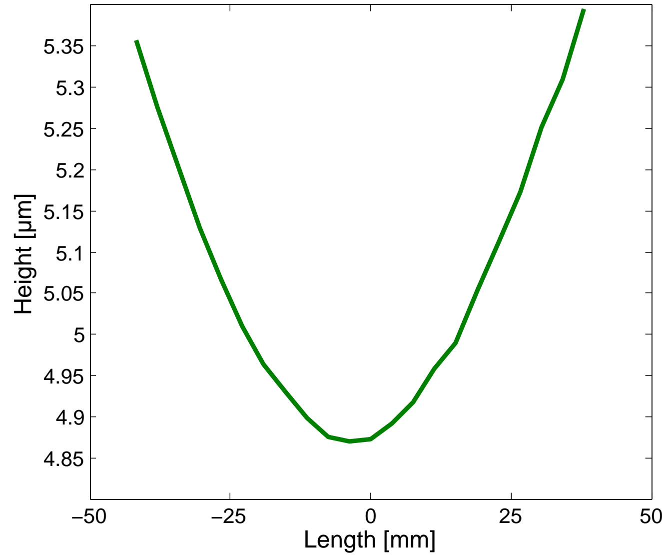

Figure 4.3: This graph shows the protrusion height across the wafer. The nonuniformity of the profile is caused by the electric field gradient in the RIE chamber during the etching. The minimum should have been in the center, but the wafer was off centered compared to the field in the chamber, during the etching process.

4.2 Materials

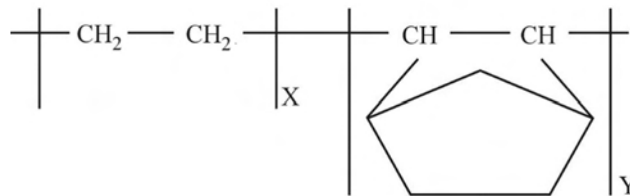

Figure 4.4: Schematic drawing of the chemical structure of Topas. The polymer is cylic olefin copolymer consisting of X times ethylene (C_2H_4) and Y times norbornene (C_7H_10) monomers [68].

The material for the cantilever needs be chosen so it is compatible with the application and the processing technique. For NIL the most widely used polymer is PMMA. This polymer is cheap and easily available [42]. However PMMA has shown poor performance in its resistance to solvents. Solvents might be interesting to measure on from an application point of view. Another polymer which has been tested is Topas, which has a much higher resistance to soap solutions, hydrolysis, acids and

	Dry_Tef2	Stand. Pass.
Pressure [mTorr]	5	10
Gas flow (C_4F_8 [sccm]	120	120
Coil power [W]	300	1000
Platen power [W]	0	0
Deposition time [s]	60	60

Table 4.1: Process parameters for the flourocarbon coating process compared to the standard passivation cycle in a DRIE. The lower power makes for easire control of the deposition rate. [69]

organic polar solvents. However, Topas is soluble in solvents like heptane, toluene and hexane. Even though this is not desirable from an application side, it does make it possible to dissolve the polymer and spin coat it which is needed for the NIL processing. These properties make it a good candidate for a cantilever that is to be used for gas sensing. Topas also has a low surface energy which makes it possible to control the stiction to stamp and substrate. Topas also has a high optical clarity which makes it difficult to perform the readout without a metal reflective pad on the cantilever [66].

4.3 Fabrication of Polymer Cantilever

The cantilever chip fabrication can be divided into two parts the first part concerning the imprinting is illustrated in Fig. 4.5, and the last part is illustrated in Fig. 4.9. The starting point is again a silicon wafer, see Fig. 4.5(a). In order to be able to later release the cantilever, a fluorocarbon (FC) layer is deposited. A FC layer is deposited during the passivation cycle in an Advanced Silicon Etch'er (ASE). The deposition has been optimized so that it is possible to spin coat polymers on top of the layer [69]. Even though the starting point is a new wafer, it is first cleaned by a 5 minutes oxygen plasma. Next the process Dry_Tef2 (see Table. 4.1) which takes 60 s and it leaves a thin layer of about 25 nm thickness, see Fig. 4.5(b). The difference between the standard passivation cycle and the process used is illustrated in Table. 4.1. The Dry_Tef2 is very similar to the process also used for antistiction coating in previous work. Only the pressure has been slightly reduced [60].
Before the polymer is spin coated, the wafer is dehydrated by placing it on a hotplate at 150 °C for 5 min. Next, layer of Topas (mr-I T85-5.0 XP [70]) is spun onto the wafer at 2500 rpm. for 30 s to a thickness of 5.5 μm. The wafer is then baked again at 150 °C for 10 minutes to remove the solvents, see Fig. 4.5(c). This step also helps planerizing the polymer coating after it has been spin coated. This happens within the first 1-2 minutes of the baking. The achieved polymer thickness is 0.5 μm thinner than what is achieved on a pure silicon surface due to the FC layer.
The Si stamp is imprinted at 170 °C at 15 kN for 30 min in an EVG-NIL machine, see Fig. 4.5(d). During the imprint process a sheet of graphene of 1 mm thickness

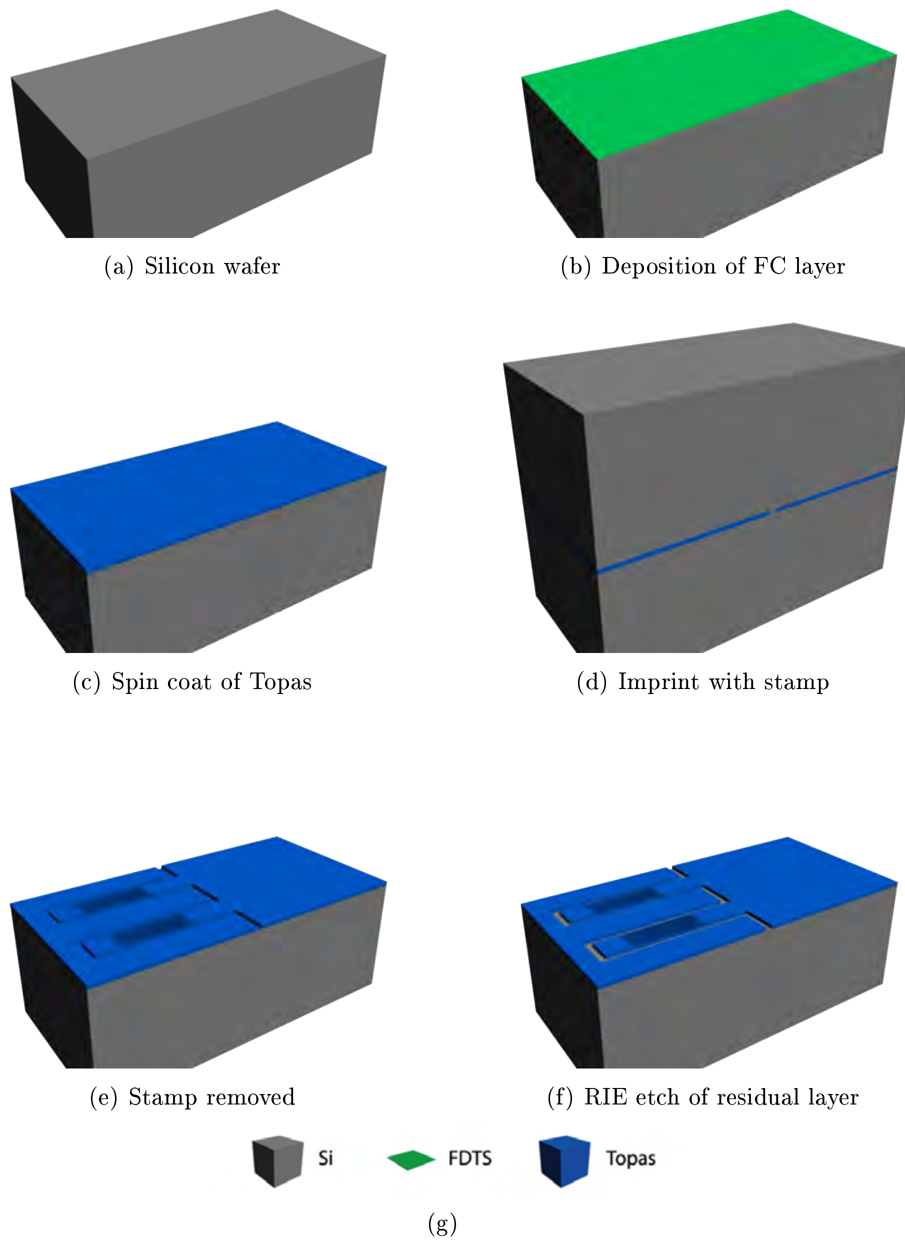

Figure 4.5: Graphical illustration of the NIL process. The starting point is a silicon wafer (a), on which a FC layer is deposited (b). A 5.5 μm layer of Topas is spin coated on (c), and imprinted at 170 °C at 15 kN for 30 minutes (d). The stamp is removed (e), and the residual layer is etched by an oxygen plasma (f).

is placed on both sides of the stamp and substrate to help distribute the pressure evenly across the wafer. The stamp is not released before the temperature is well below the T_g of Topas. The T_g of the Topas used is 85°C, and the release is done around 30 °C. The release is done by forcing a razor blade in between the stamp and substrate, and slowly moving it around the edge gently releasing the stamp from the substrate, see Fig. 4.5(e).
Fig. 4.6 shows a 4" wafer before and after imprint. Before the imprint, the polymer layer is fairly uniform. The small variation in color across the wafer indicates that there is a slight difference in thickness. After the bake on the hotplate the polymer contracts a bit. It is illustrated around the edge of the wafer, where the polymer retracts in small regions (lower left side of the wafer). This is outside the area where the chips are placed, and therefore can be neglected since the influence is minimal. If the FC coating was more repellant it would not be possible to spin coat Topas on top of it. After imprint, the polymer has been redistributed and the uniformity across the wafer looks very different, see Fig. 4.6(b). Even though it look like the thickness is very different across the wafer then, it is important to remember that a few nanometer will result in a change in color, and the wafer used for fabricating the cantilevers, even though very smooth, have a variation across the wafer on the micron level.

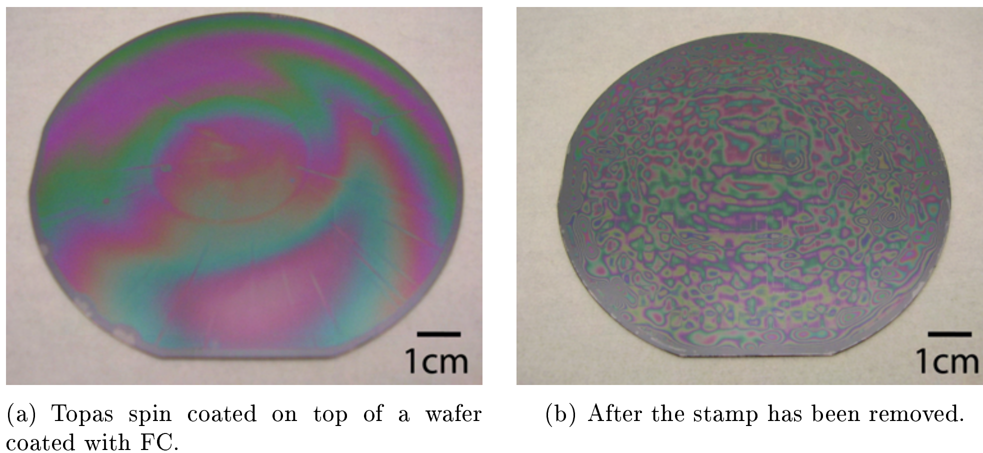

(a) Topas spin coated on top of a wafer coated with FC.

(b) After the stamp has been removed.

Figure 4.6: Images of wafer before imprint and after imprint. In (a) it is possible to see Topas creeping a little, in the lower left edge due to the low adhesion between the Topas and FC layer. In (b) a picture of the Topas after a successful imprint has been performed.

The imprint leaves a residual Topas layer at under the protrusions that needs to be removed, see Fig. 4.5(f). The residual layer thickness can be measured by making a scratch through the polymer and then measure it with a profilometer, as seen in Fig. 4.7(a). To the left is the scratch and to the right is the protrusion, the difference is 145 nm. The residual layer is etched by an anisotropic RIE for 6 min. (N_2: 99 sccm, O_2: 20 sccm, pressure: 300 mTorr, power: 60 W). Measuring the profile again in the same place, it can be tested that the residual layer is removed. Fig. 4.7(b) shows that the scratch and the protrusion on the right has the same depth and thus

the residual layer is removed. By comparing the difference between the height before and after the etch, the etch rate can be extracted to be 2 nm/s. In theory the etch is far too long as it etches about 740 nm. The prolonged etch time is to ensure that the residual layer has been removed across the entire wafer.

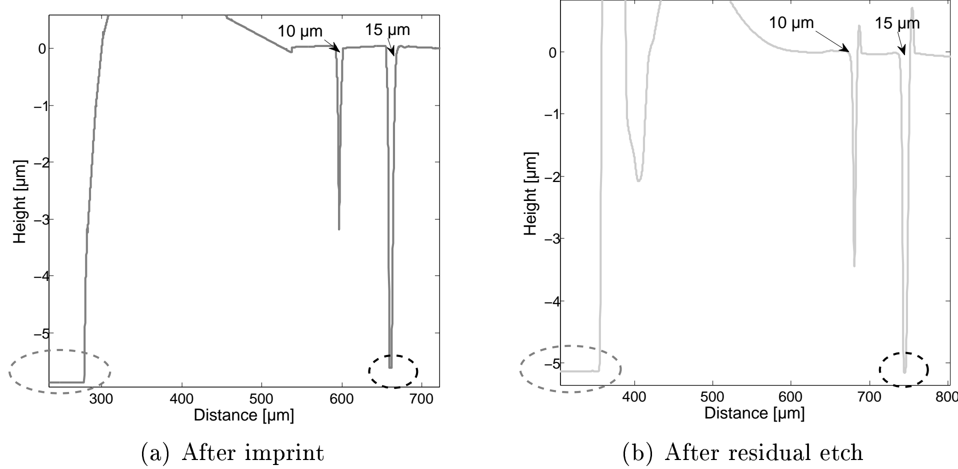

(a) After imprint (b) After residual etch

Figure 4.7: The graphs shows the profile measurement before and after the etch of the residual layer. To the left on the graphs are the area (marked with a dotted ellipse) which has been scratched and therefore the Topas has been removed. The number indicates the width of the protrusion (10 and 15 μm), the cantilever starts to the right of the 15 μm protrusion. (a) Shows the profile before the etch where there is still a residual layer, which is about 145 nm the height difference between the left and right side of the scan. (b) Is a scan the same place but after the etch.

From the fabrication of the stamp there was a difference between the protrusion height across the wafer, as shown in Fig. 4.8. The height of the polymer after the imprint is identical to the height of the protrusions on the stamp. However after the residual layer has been removed the height is reduced, partly due to over etching, but also because the profile of the etch various across the wafer [67]. However since it is the same machine which is used for this part of the process the etching profile will be the same thus compensating a little for the uniformity achieved in the stamp. The thickness variation across the wafer is 300 nm, and 95 % of the chips are within a range of 170 nm. Compared to the variation in the stamp depth shown in Fig. 4.8 the cantilever thickness variation across the wafer is significantly smaller. The standard deviation for the cantilever thickness across a wafer is 67 nm, which is considerable less than what has prevoiusly been reported for microcantilevers fabricated in thermoplatics by injection molding with a standard deviation of 300 mn [30]. It should also be noted that the injection molded microcantilevers have a length and width variation of 10 μm and 4 μm, and for this technique the width difference is less than one micron and the variation in length is around 1-2 μm due to alignment error. The process has been repeated for over 30 wafers with a cantilever thickness varying between 4.5 and 5 μm, from wafer to wafer using the same stamp. When a metal reflective pad or a complete coating of the cantilever is required a

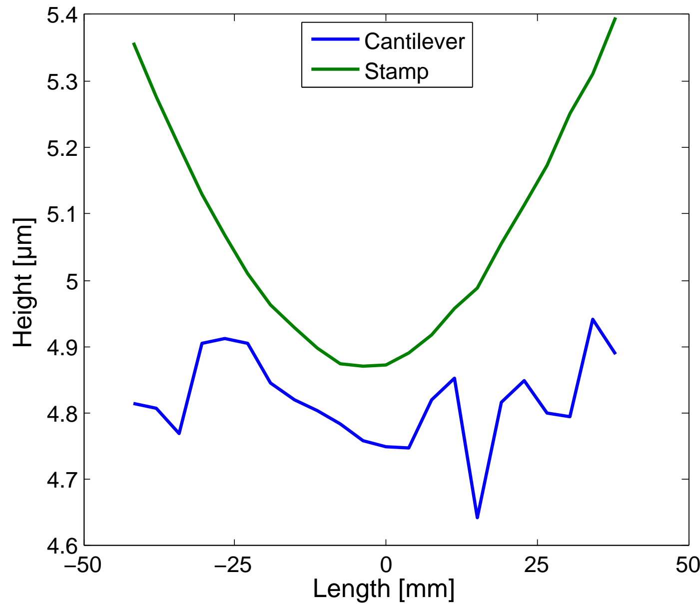

Figure 4.8: Graph showing the protrusion size of the stamp and cantilever height across the wafer. The protrusion height of the stamp is equivalent to the cantilever thickness before the residual layer etch.

simple lift-off process is performed. The best lift-off results were achieved by using a 2.2 μm thick resist AZ5214E, and performing an image reversal process. The pattern is exposed for 5 s (35mJ/cm^2), baked for 100 s at 120 °C, flood exposed for 35 s and then developed. Next, 5 nm of titanium for adhesion and 20 nm of gold are evaporated by e-beam. The deposition rate of the metal was reduced to 1 Å/s, as higher rates tends to heat up the polymer during the process resulting in a stress and bending of the final cantilever. The lift-off was performed in acetone with short second ultra sound pulses to assist the process. The final process takes around 15 minutes, see Fig. 4.9(a).
In order to have a support for the cantilever a 300 μm thick layer of SU-8 2075 is subsequently spun on at 600 rpm for 60 seconds and soft baked at 50 °C for 10 h. The body of the chip is defined in this layer by UV exposure for 1400 mJ/cm^2, post baking at 50 °C for 10 h and finally developing for 30 min., see Fig. 4.9(b). In order to prevent reflow of the cantilevers and to reduce residual stress in the SU8 the baking processes was kept below 50 °C.
Finally, the finished chips can be removed mechanically by tweezers and the cantilevers are released, see Fig. 4.9(c). The release yield is 95 % after fabrication and is slightly improving over time after fabrication. The final out of plane bending of the cantilever apex is below 10 μm, for cantilevers with no metal coating or only at the tip.
Optical microscope images of the released cantilevers can be seen in Fig. 4.10 and in Fig. 4.11.

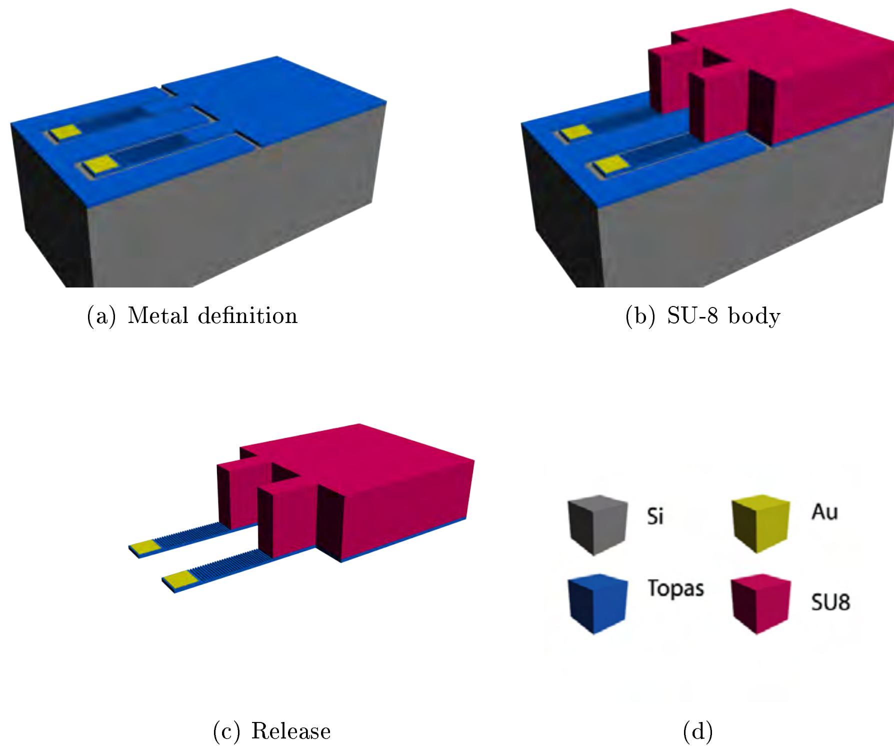

(a) Metal definition (b) SU-8 body

(c) Release (d)

Figure 4.9: Graphical illustration of the process sequence for the definition of metal pad and SU8 body structure and final release. (a) metal is defined at the apex of the cantilevers, (b) a thick 300 μm layer of SU8 is defined by UV-lithography as a support structure. The final cantilever chip can be lifted of the FC layer and the cantilevers are released (c).

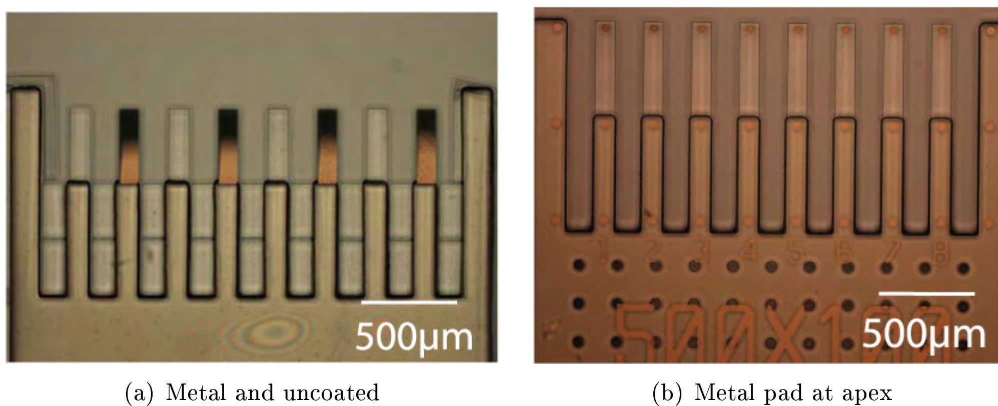

(a) Metal and uncoated (b) Metal pad at apex

Figure 4.10: Top view pictures of released chips. Every second cantilevers is metal coated in (a) and in (b) only the apex of the cantilever is coated.

The release yield of the cantilevers actually improves over time, as the cantilevers

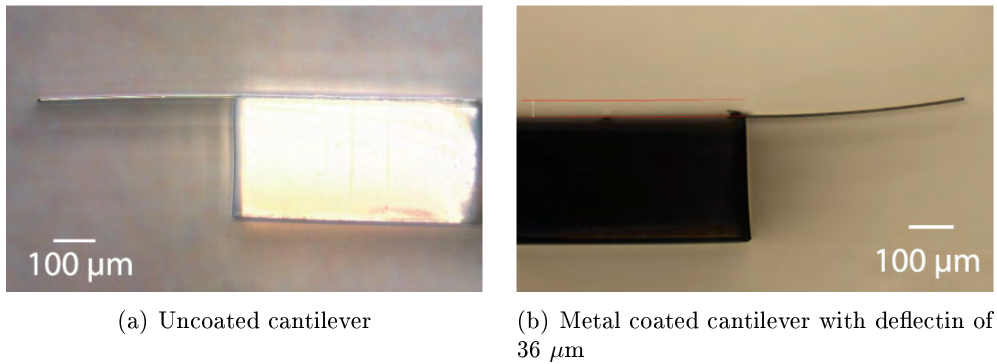

(a) Uncoated cantilever

(b) Metal coated cantilever with deflectin of 36 μm

Figure 4.11: Sideview of released cantilevers, the uncoated cantilever has almost on initial bending. The metal coated cantilever has a bending from the metallization process which displace the tip about 36 μm.

are easier to release a few days after processing. This also means that the imprinting step needs to be done within 24 hours of spin coating the Topas, so the polymer does not stick to the stamp. After one year the chips still remain on the FC layer, but become very easy to remove.

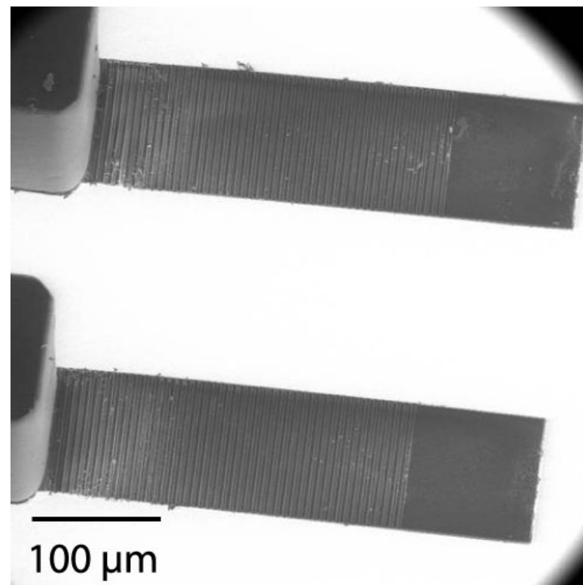

Figure 4.12: SEM image of a released pure polymer cantilever with surface structures. The cantilever is 400 μm long, 100 μm wide and 4.5 μm thick.

4.4 Challenges During Processing

During the processing of the cantilever several challenges occurred. As already discussed in Sec. 3.3, the process of making a free standing cantilever by NIL is not straight forward, and has not been done before. In this process the polymer is to be lifted off the substrate at the end. This requires precis control of the FC layer between substrate and the polymer and adhesion to the stamp needs to be as small as possible. Basically, two things can go wrong. First, the polymer can stick to the stamp and be lifted off the substrate. An example of this is shown in Fig. 4.13. Second, the polymer might stick to the substrate and either the chip can not be removed or the cantilever is damaged in the process, see Fig. 4.14.

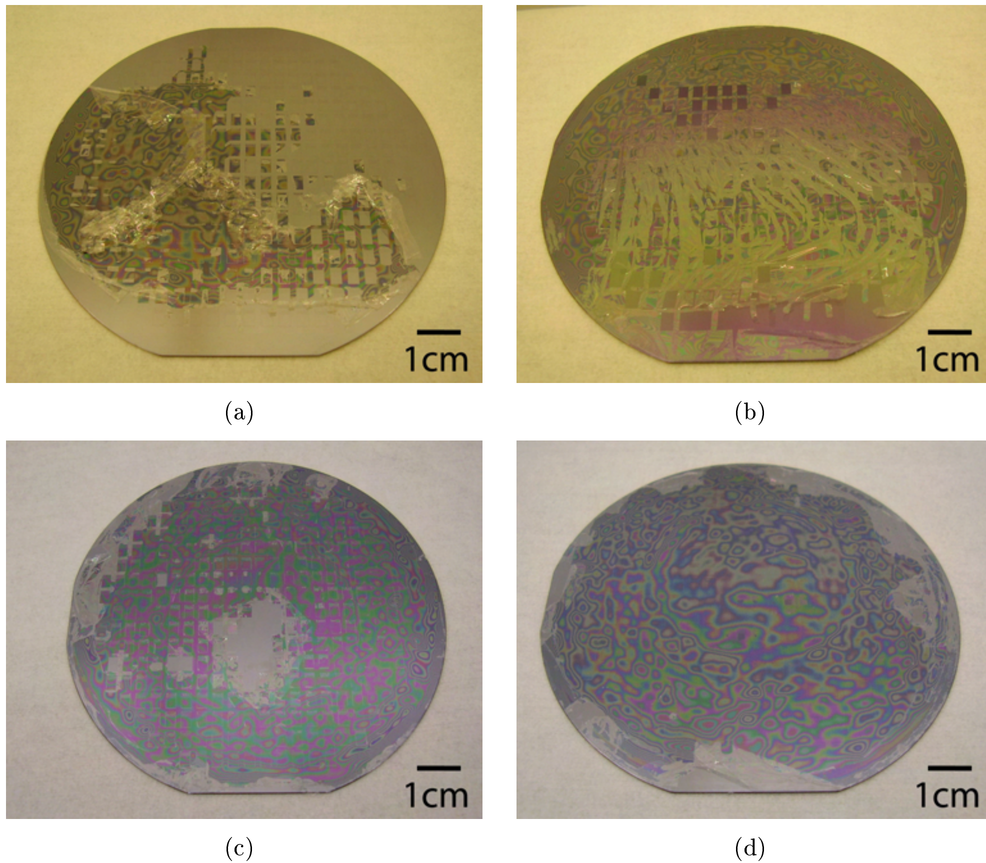

Figure 4.13: It can be challenging to control that the Topas stay on the FC layer. (a) and (b) have been performed with a stamp where there was problems with the RIE process, which resulted in a rough stamp surface which peeled of the Topas on large areas of the wafer. (c) is performed with a stamp that still have the oxide layer, even though it had been coated subsequently with FDTS the Topas still comes off. (d) shows how the Topas starts to come of around the edges when the coating of the stamp has been damaged due to the separation process by a razor.

The stiction to the stamp can arise either from the stamp or from the surface coating.

The first test was done without oxidation of the stamp, and initially it worked fine. Later there were problems with the performance of the RIE, which caused a small increase in surface roughness. The result can be seen in Fig. 4.13(a) and Fig. 4.13(b), where the polymer is starting to fall of the substrate. Some of the chips remain on the substrate showing that for that area the adhesion was stronger between the substrate and the polymer than the force needed to brake the polymer around the thin residual layer. For some of the chips the polymer has remained on the stamp.
Therefore the oxidation step was introduced in order to smoothen the surface of the stamp. It was tested if the oxide can be left on the stamp during imprint and the result after imprint is shown in Fig. 4.13(c). The area in the center clearly shows that the adhesion to the stamp is too strong. Removing the oxide and reapplying the FDTS coating solves the problem. The FDTS antistiction coating can also cause problems. Obviously this process is more sensitive than most other NIL work, since the polymer adhesion to the substrate is weak. The separation of the stamp and substrate was done by using a razor blade, and as the blade is pushed in between the two, it could mechanically scratch and damage the FDTS coating of the stamp. This resulted in problems with the polymer releasing from the substrate around the edges of the wafer, see Fig. 4.13(d). This problem was greatly reduced by keeping the razor blade at a small angle away from the stamp thus limiting the contact between the razor blade and stamp.

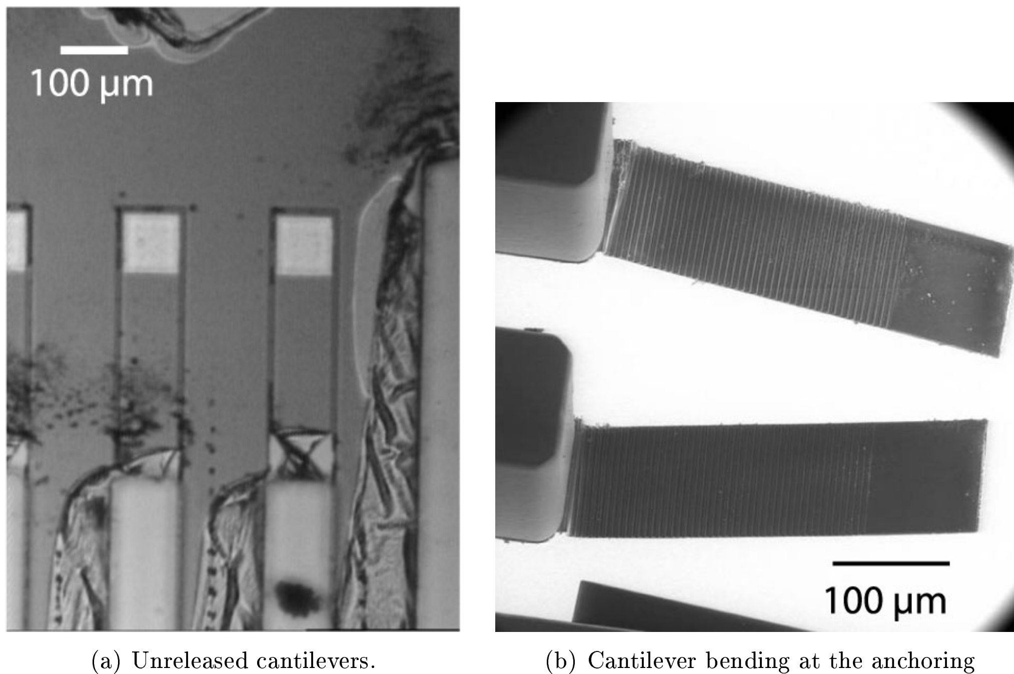

(a) Unreleased cantilevers. (b) Cantilever bending at the anchoring

Figure 4.14: Illustration of problems where the adhesion to the FC have been too large. In (a) the cantilever can hardly come off and in (b) the cantilever bend severely at the anchoring.

Even though the imprinting process went as planned the cantilevers still had to be

released, unfortunately it is necessary to finish the processing before it is possible to test if the cantilevers can be released. Fig. 4.14(a) shows an example of how cantilevers do not come off when the SU8 support structure is lifted off. For the pure polymer cantilevers without metal, it has not been a problem that the cantilevers have been bending due to internal stresses. It was however discovered that if the FC coating is not performing well, then problems with bending at the anchoring of the cantilever might occur, probably due to plastic deformation during the release process.
The imprint process also needs to be optimized. There are three parameters to change for the imprint; time, pressure and temperature, as introduced in Eq. (3.3). In order to reduce the time and residual layer for the imprint, it was tested to do the process at 190 °C. The result is shown in Fig. 4.15. The defects are clearly not due to filling of the stamp as many of the defects starts from around the protrusions. By reducing the temperature to 170 °C the defects disappeared. The pressure is limited by the machine and what the stamp and substrate can withstand without breaking. A pressure of 15 kN for 30 minutes proofed to give reproducible and uniform results.

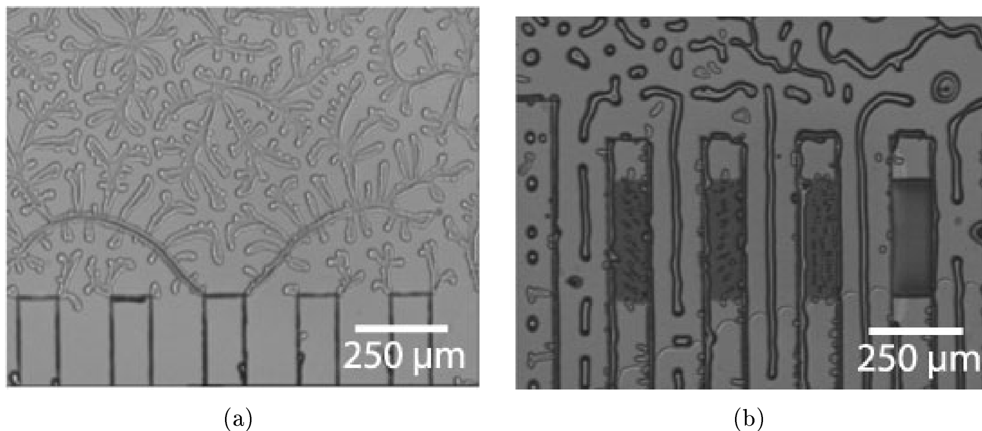

(a) (b)

Figure 4.15: These microscope pictures show the problems when imprint at 190 °C, by reducing the temperature to 170 °C the defects disappeared. The right picture could indicate poor filling, but since it was removed by lowering the temperature it was not the case.

In order to optimize the release it was tested to replace the FC layer by a sacrificial layer. Two different approaches were tested. First, it was tested to have an oxide layer beneath the polymer. The problem in this case is that after the oxide has been etched, the cantilever is pulled down towards the substrate due to capillary forces and stretch marks (wrinkles) close to the anchoring point of the cantilever have been observed. It was also tested to combine the oxide and the FC layer. However, this caused the oxide etchant to follow the FC layer and after just 5 min. of etching the chips start to fall off the substrate. The etch can be stopped before the chips are fully released and the result after 1 minute of etching, see Fig. 4.16. Using this method the release yield is not significantly improved compared to what can be achieved without the oxide layer.
The metal deposition can induce stress in the structure as shown in Fig. 4.11(b).

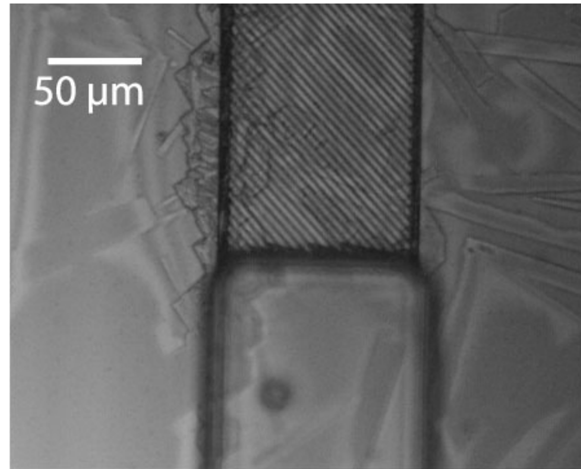

Figure 4.16: Optical microscope picture illustrating some of the issues in using a sacrificial layer of oxide. The oxide, has been etched for 1 minute through the openings (the two vertical black lines). However, the etchant also moves in between the polymer and substrate. Thus the chips will fall off the substrate after approximately 5 minutes of etching.

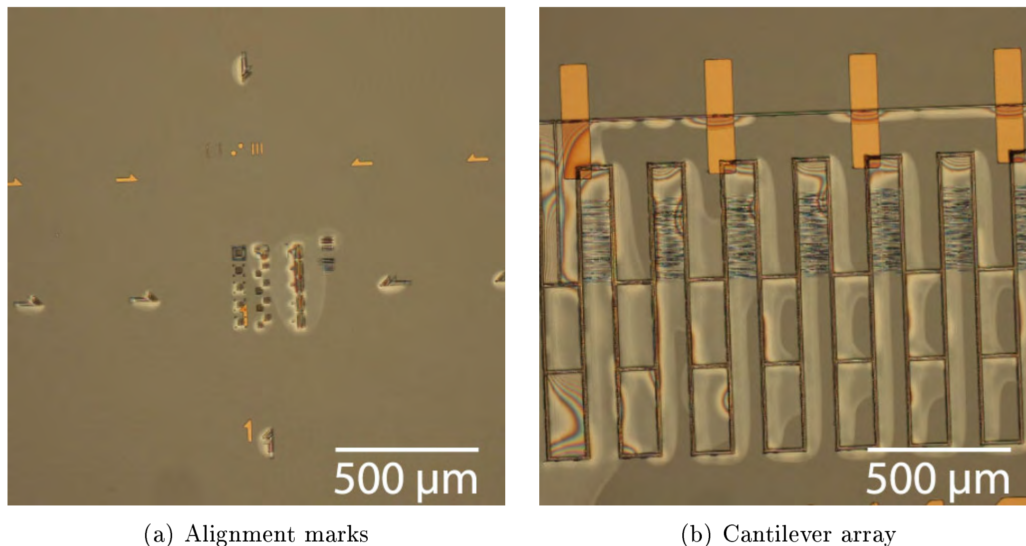

(a) Alignment marks (b) Cantilever array

Figure 4.17: Alignement of imprint to an underlying metal layer proofed impossible with the machines available. After the alignment the stamp moved with respect to the substrate.

The problem was reduced by reducing the deposition rate, but the cantilevers were still bending. Another way around the problem is to place the metal layer below the polymer, so the metal is evaporated onto the substrate and therefore does not induce stress int the polymer. However, this requires that the stamp is aligned to the metal layer. This alignment process turned out to be very difficult, for two reasons. First, it was not possible to do the alignment between the stamp and the metal layer as shown in Fig. 4.17. There was a miss alignment error of about 50 μm horizontally

and about 400 μm vertically. The miss alignment was about the same for all the trials but not constant enough to be useful, the problem is due to machine limitation. The second problem was that in order to perform the alignment the graphene sheets normally used for stabilizing pressure during the imprint could not be used. This caused the stamp to a crack.

4.5 FIB Cantilever

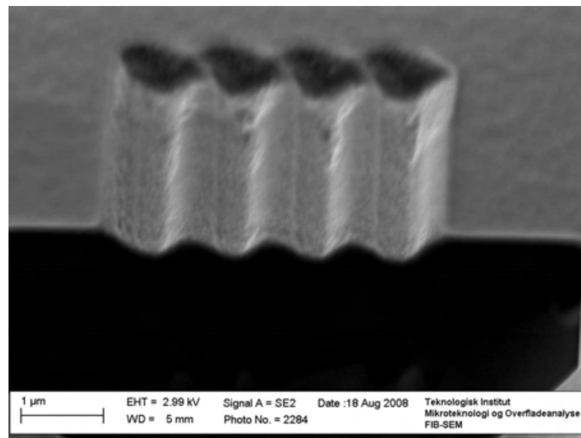

Figure 4.18: SEM image of a test structure fabricated in sililicon by FIB at DTI by Daniel Nilsson. This is a test structure of the grooves, and it shows that the sides are not perfectly flat and the angle is not accurate, but it can be used for some initial tests.

In order to make more advanced structures as discussed in Sec. 3.4, it is necessary to use other machines such as for example FIB. In Sec. 3.4 we discussed to use it for making a reflector made of grooves with an angle of 45°. The structure should be milled into the silicon stamp, so it can be directly transferred to the cantilever. The FIB of the stamp was performed at DTI by Daniel Nilsson. A SEM image of the first small test grooves can be seen in Fig. 4.18.
A larger array of these grooves where then milled into a stamp and used to fabricate cantilevers. A picture of the stamp after the imprint can be seen in Fig. 4.19. The grooves are placed at the end of the cantilever as they are intended for readout of the deflection of the cantilever. The microscope picture also illustrates another problem as the milling process increases the surface roughness of the stamp, which is indicated by the slightly darker color of the silicon around the grooves. A closer observation of the grooves shows that small polymer residues remain in the stamp after the separation between the stamp and substrate. The stamp was not oxidized after the FIB process in order not to alter the structures. The first results however indicate that it is probably necessary to optimize the smoothness of the structures.
Looking at the polymer after imprinting it is more clear what effect the increase of surface roughness has caused, see Fig. 4.20. The polymer around the cantilever with the grooves has been lifted off leaving a small gap between the polymer and the

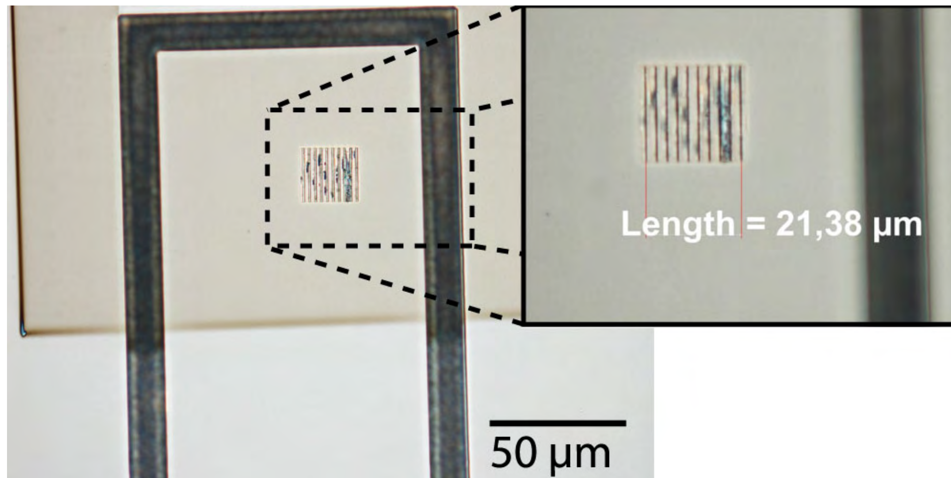

Figure 4.19: Optical microscope picture of the stamp after imprint. Polymer residues in the grooves from the imprint indicates that the FIB area is not smooth.

substrate, which is illustrated by the color rings. The grooves made by the FIB have been transferred as shown in Fig. 4.20. So it is possible to use FIB to modify the stamp and transfer the pattern to a cantilever. However the process needs further optimization, in order to be able to realize grooves suitable for optical applications.

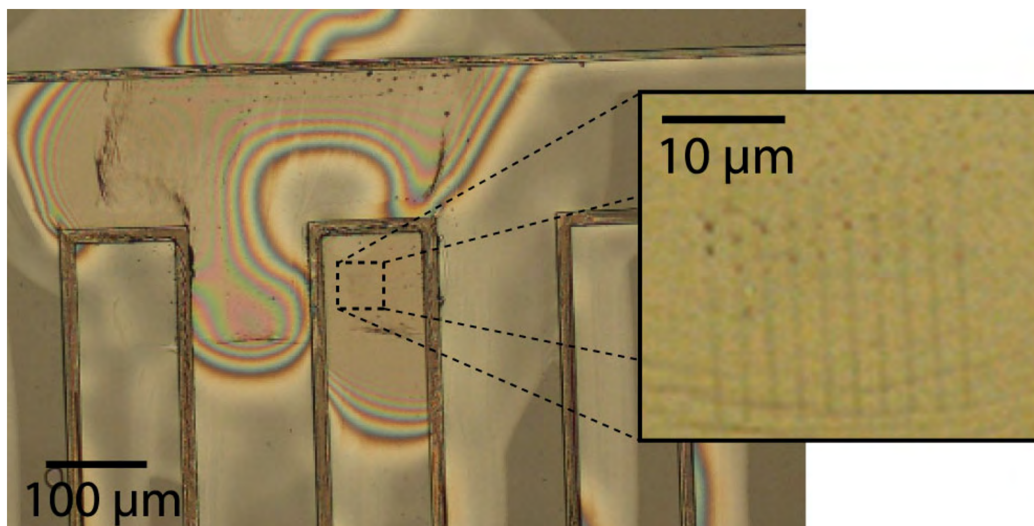

Figure 4.20: Optical microscope picture after imprinting with a stamp that has been milled with FIB. The enlarged picture shows the pattern that has been transferred, which consist of 10 lines with a pitch of about 2 μm.

4.6 Summary

This chapter has focused on the fabrication of the cantilevers and some key fabrication challenges have been highlighted. First the stamp was fabricated in silicon by RIE and oxidation, and finally coated with FDTS. The stamp was then used to fabricate microcantilevers in Topas, and a thick layer of SU8 was used to define a support structure in order to be able to handle the cantilevers. Cantilevers with a length of 200-500 μm, width 100 μm and a thickness of 4.5-5 μm were successfully fabricated with a yield of 95 %. A series of problems occurred during the fabrication, and these were discussed and solutions to how they could be avoided or solved have been presented. Finally, the possibility of using FIB for realizing advanced structures on top of the cantilevers was presented.

Chapter 5

Characterization

This chapter will describe the mechanical characterization of the fabricated cantilevers. For sensing purposes, the mechanical properties in static and dynamic mode are of interest. The static behavior is examined by deflecting the cantilever by an AFM, while the dynamic behavior is examined by using a laser-Doppler vibrometer.

5.1 Static Characterization

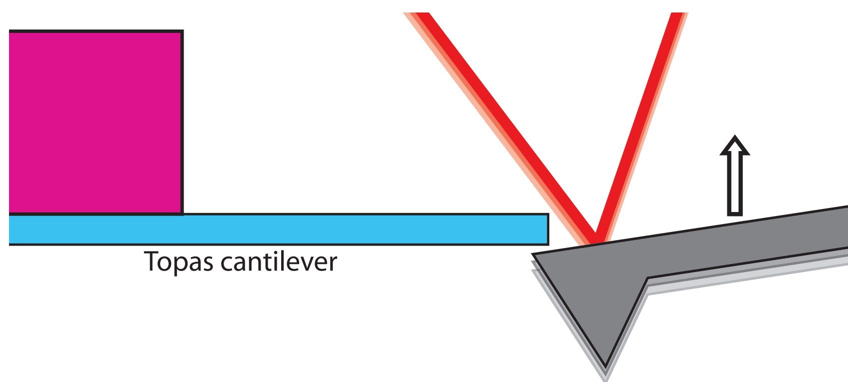

Figure 5.1: Illustration of the setup to measure the spring constant of the fabricated Topas cantilevers. The AFM cantilever is moved upwards in the z-direction as indicated by the arrow, and when it touches the Topas cantilever it will deflect. The deflection is detected by the optical readout system for the AFM.

As discussed in Sec. 2.1 the softness of the cantilever can be examined by looking at the spring constant and the surface stress sensitivity. The easiest way to measure the softness of the cantilever is to measure the spring constant. The spring constant of the fabricated polymer cantilevers can be measured by using a commercial AFM cantilever with a known spring constant of 3 N/m. For this purpose we have taken a chip with cantilevers which are 500 μm long, 100 μm wide and 4.5 μm thick. The measurements have been performed on four different cantilevers from one chip. The

AFM cantilever is used to deflect the polymer cantilever and the resulting deflection of the AFM cantilever is measured. The setup is illustrated in Fig. 5.1.
The AFM cantilever is moved in the Z direction over a distance of 12 μm. The response from one of these measurements is shown in Fig. 5.2.

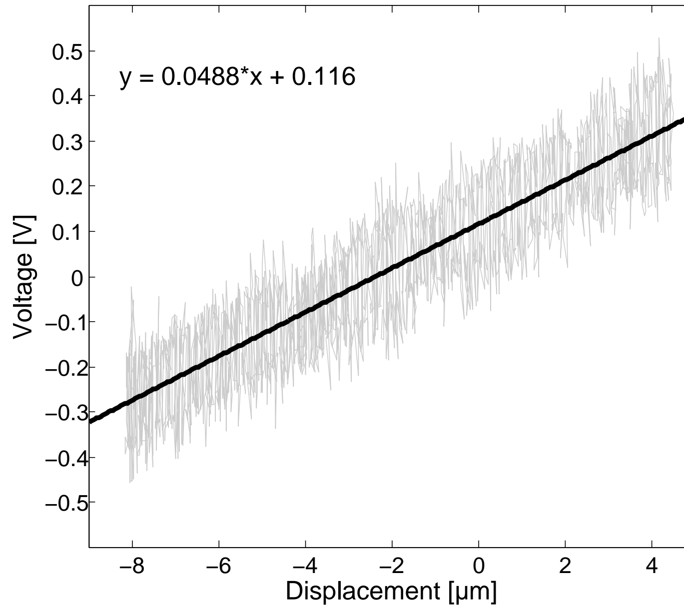

Figure 5.2: The graph shows the deflection of the AFM cantilever, when deflecting a 500 μm long and 4.5 μm thick Topas cantilever. The x-axis shows the displacement of the AFM and the Y-axis shows the differential voltage between the photodiodes A and B in the AFM. The slope is $S_1 = 0.0488$ V/μm.

The response shows a linear behavior which simplifies the theory significantly. In order to calculate the spring constant for the Topas cantilever it is necessary to find the slope of the response from the AFM cantilever. This is done by moving the AFM probe against a solid surface. The response is shown in Fig. 5.3. The two slopes can then be compared and the spring constant can then easily be calculated from the following relation between the slope and the spring constant:

$$\frac{S_{cal}}{k_{cal}} = \frac{S_{Topas}}{k_{Topas}} \tag{5.1}$$

Where k_{cal} is the spring constant of the AFM, k_{Topas} is the spring constant for the Topas cantilever and S_{cal} and S_{Topas} are the measured slope for the AFM and Topas cantilever. For this equation to be valid $k_{cal} \gg k_{Topas}$. For the cantilever measured in Fig. 5.2 the spring constant can be calculate to 52.5 mN/„ and for the four measured cantilevers the result is given in Table. 5.1.

The theoretical spring constant can be calculated for the cantilever by:

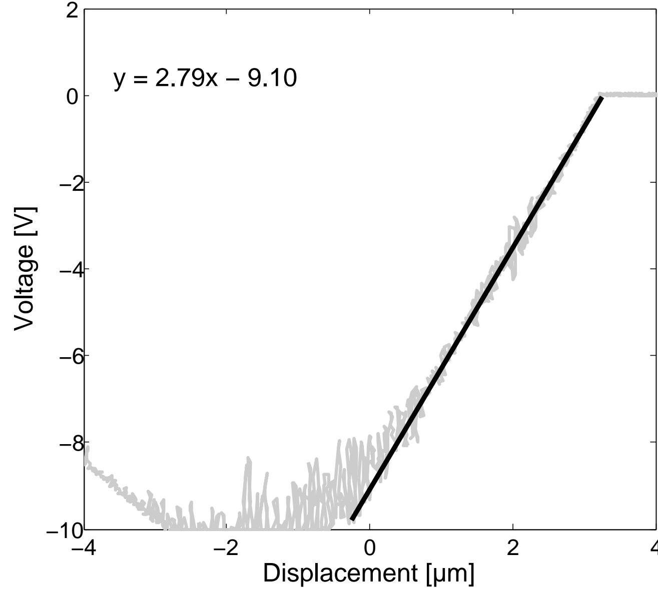

Figure 5.3: The graph shows the deflection of the AFM cantilever, when pushed against a solid surface. The line is fitted to the linear region in order to be able to do the comparison with the Topas cantilever. The x-axis shows the displacement of the AFM cantilever and the Y-axis shows the differential voltage between the photodiodes A and B in the AFM. The slope is $S_{cal}. = 2.79$ and the coresponding spring constant is $k_{cal} = 3$ N/m.

Cantilever No.	1	2	3	4	Average
Slope [V/μm]	0.0627	0.0655	0.0576	0.0488	0.0587
Spring constant [mN/m]	67.5	70	62	52.5	63.1

Table 5.1: List of the slope fitted to the measurements and the calculated spring constant from the fit for four Topas cantielvers. The average is 63.1 mN/m compared to a theoretical value of 47.4 mN/m.

$$k = \frac{3Ewt^3}{12L^3} \tag{5.2}$$

Where E is young's modulus of Topas which is 2.6 GPa, w is 100 μm, t is 4.5 μm and L is 500 μm. This results in a theoretical value of 47.4 mN/m, which is 25 % less than the average measured spring constant. Considering the error in the measurement, and the uncertainty on the spring constant for the commercial AFM cantilever (1-7 N/m which corresponds to a span of -66% to +133%), a 25 % difference is acceptable. Since the two cantilever are optically aligned there will be some uncertainty in this process of about 5 μm of where the Topas cantilever hits the AFM, This results in a difference in spring constant for the AFM from 3 N/m to 3.2 N/m and thus and uncertainty of +/- 3%.
Using the measured spring constant the stress sensitivity ($z_{max}/\Delta\sigma$) can be calcu-

lated to 11 $\mu m^2/N$. The sensitivity is hereby similar to the best commercial available Si cantilevers [22].

5.2 Dynamic Performance

The dynamic behavior of the fabricated Topas cantilever will be investigated in two ways. First the cantilever deflection is detected by a classical beam deflection setup used also used in AFM and secondly by using laser-Doppler vibrometer where the profile of the resonating cantilever can be mapped. The cantilever is actuated by a piezo electric element. Scanning a 400 μm long cantilever between 6000 Hz and 9000 Hz gives the response shown in Fig. 5.4. The resonance frequency is found to be 7.41 kHz, which is close to the theoretical of 7.26 kHz, for a 4.5 μm thick and 100 μm wide cantilever made of Topas. The measurement is performed at atmospheric pressure, and the resulting Q-factor is only 22, which result in a rather poor mass sensitivity of 10 ng, which can be compared to 190 ng total mass of the cantilever. This can be a potential problem for sensing purposes. Polymer has a large internal damping compared to silicon, and therefore polymer cantilevers are not ideal for operating in dynamic mode.

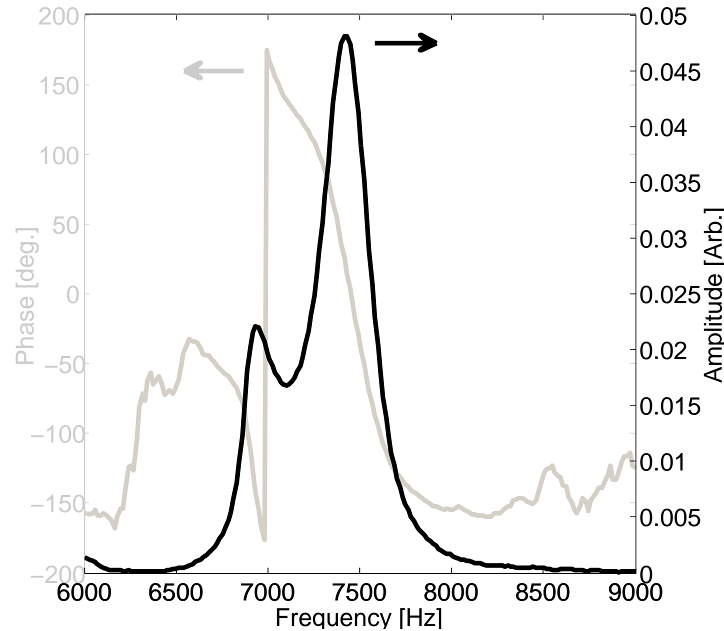

Figure 5.4: Resonant peak for a Topas cantilever with a length of 400 μm, both with amplitude and phase plotted with respect to the frequency.

The cantilever motion can be monitored with a microscope based laser-Doppler vibrometer (MSA-400) from Polytec GmbH [71]. It is possible to map the profile of the cantilever as it is resonating. For a 500 μm long cantilever the profiles of the first 4 modes are shown in Fig. 5.5.

The same system was used to measure the first six modes for the cantilever and the

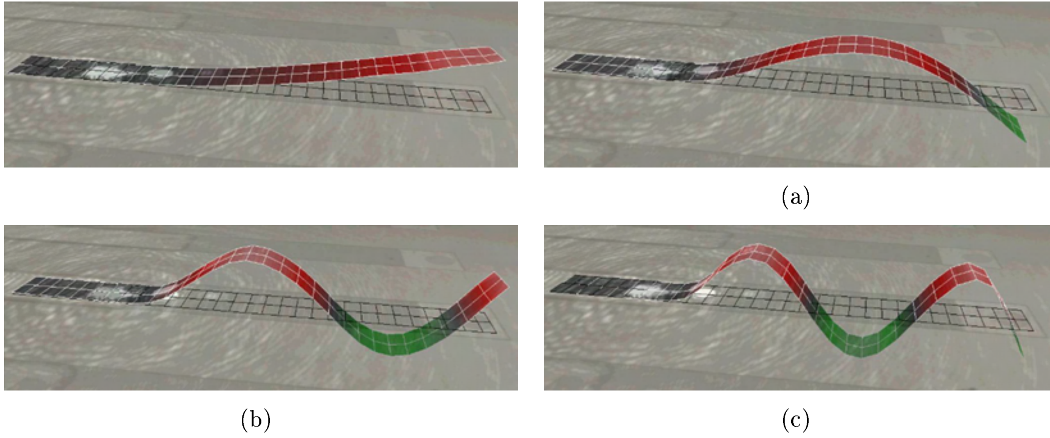

(a)

(b)

(c)

Figure 5.5: Profile of a Topas cantilever in the first 4 resonant modes. For a 500 μm long cantilever, the surface has ripples with a pitch of 4 μm and a depth of 800 nm.

Resonance mode	1	2	3	4	5	6
Frequency [kHz]	4.19	27.6	73.3	138	240	345
Theoretical [kHz]	4.64	29.1	81.5	160	264	394

Table 5.2: Table of the measured frequencies for the first 6 modes. The cantilever is 500 μm long with a rippled surface with a pitch of 4 μm and a depth of 800 nm. The resonance frequency is about 10 % to low which can be explained by the softening due to the ripples.

values are listed in Table. 5.2 with respect to the theoretical value. The measured values are about 10 % below the theoretical value. The measured cantilever has ripples on the first 400 μm, which will lower the stiffness and the resonant frequency of the cantilever. Fitting the thickness of the cantilever to the measured frequency a cantilever. The measured frequency corresponds to cantilever thickness of around 4 - 4.1 μm. This is 400 nm thinner than the cantilever thickness, and roughly half the height of the ripples.

5.3 Summary

The fabricated Topas cantilever has been characterized by measuring the static and dynamic performance. The static performance was characterized by using an AFM cantilever to deflect the Topas cantilever. The average spring constant was found to be 63.1 mN/m, compared to a theoretical value of 47.4 mN/m. For the dynamic measurements there was good agreement between the measured and the theoretical value of the resonant frequency. The Q factor of the cantilever is around 22 at atmospheric pressure. This value is low compared to silicon cantilevers and indicates a poor performance in dynamic mode.

Chapter 6

Peptide-Based Receptors for Explosives

In the group of Professor A. Majumdar, at University of California Berkeley they have also been working on microcantilevers for sensing applications [72]. The fabricated Topas cantilevers have been implemented in an existing setup at Berkeley, capable of measuring on large arrays simultaneously. In this chapter the setup for readout of an array at microcantilevers will be described and the fabricated topas microcantilevers will be characterized using this system [6, 73, 74]. Furthermore, the group at Berkeley has been working on peptide receptors for explosive detection. These receptors will be attached to the Topas cantilevers and functionalized cantilevers will be tested for explosives detection in the setup [75].

6.1 Setup

Lim *et al* has developed the setup for readout of a large array of cantilevers. Their approach has been to use a collimated laser beam from a He-Ne laser for cantilever illumination and a CCD screen for detection of the movement of the cantilevers. The setup is shown in Fig. 6.1. The chips with the cantilever is mechanically fixed inside a chamber, which can be temperature controlled by a peltier element. The gas composition can be controlled by three mass flow controllers and series of valves. The reflected laser beam is passed through a beam splitter and through a lens onto the CCD camera. The great advantage with this setup is that it can readout from multiple cantilevers simultaneously. The major drawback however is that it is not possible to align to individual cantilevers, and therefore the fabricated cantilevers must be almost perfectly identical in order to be aligned simultaneously.
In order to be able to measure the deflection from a large array of cantilevers Lim *et al* have made a custom design. Where each cantilever have a rigid paddle at the end of the cantilever shaped as an open box (Fig. 6.2). The cantilever itself is made from low-stress silicon nitride and gold. At the paddle of the cantilever the gold is mainly used to increase the relectivity, while for the rest of the cantilever (beam), the gold is used for surface immobilization of biomolecules. The final cantilever have

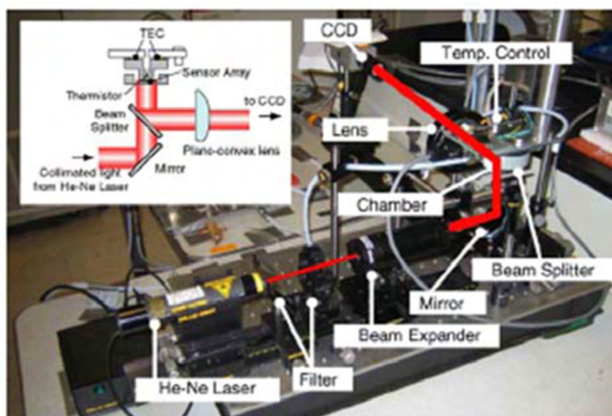

Figure 6.1: Picture of the setup at U.C. Berkeley. To the left is a He-Ne laser. The filters are used to control the intensity of the laser beam. The beam expander expands the beam while the mirror reflects the beam onto the chamber containing the chip. The reflected beam from the cantilever hits a splitter and is directed through a lens on to the CCD camera [6].

a small bending which makes the paddle bend at an angle and thus help reducing the noise from the rest of the chip as the light from the paddle is reflected at this angle, see Fig. 6.2. The gold is only on the top side of the cantilever thereby ensuring that only the top side is being functionalyzed. The chip is designed so it include wells for a set of cantilevers, which then can be functionalyzed by filling the well with a solution containing the biomolecules of interest.

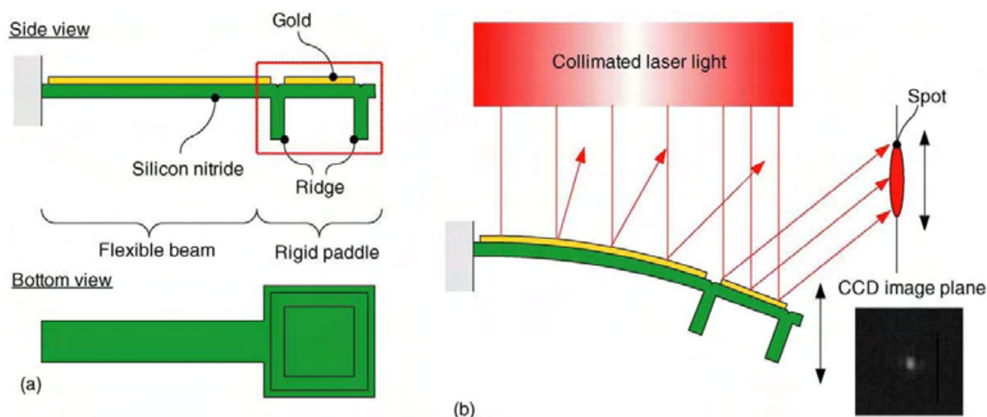

Figure 6.2: Design of the cantilever from U.C. Berkeley. a) shows a graphical representation of the cantilever in both side and bottom view. b) shows how the rigid paddle is used to help focus the reflected beam on to the CCD. (It should also be noted how the bending of the cantilevers helps the beam of interest to be reflected of at an angle, thus reducing noise from unwanted light) [6].

The CCD camera captures frames at a given rate, and these can then be analyzed to find the movement of the cantilevers. This is done by a Matlab program, which analyzes each frame and calculates the position of each cantilever. In order for the

program to be able to differentiate between different cantilevers each dot is separated by a box, see Fig. 6.3. The noise and stray light is subtracted by setting a threshold intensity and the center of the reflected spot is then calculated using the centroid algorithm in Matlab [6]. By moving the lens around it is possible to zoom in on a number of chips and increase the sensitivity, but then the number of cantilevers is limited.

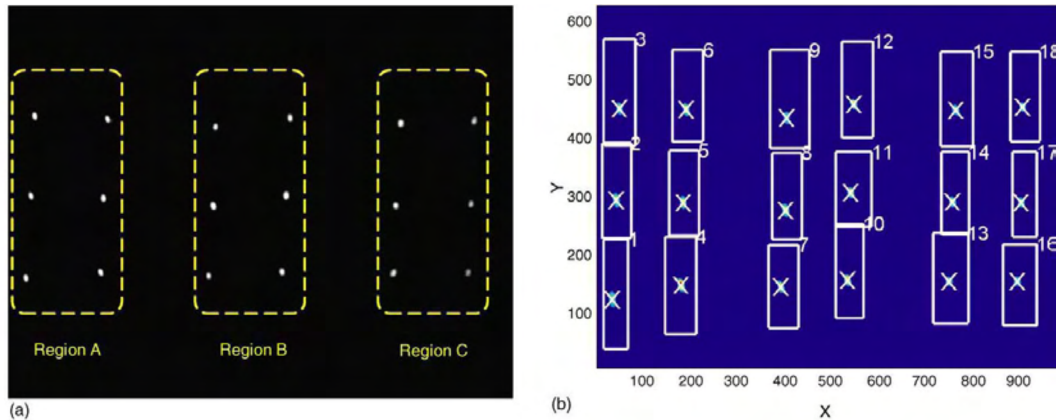

Figure 6.3: The white spots on (a) represents the reflected laser light from the paddle of the cantilevers. The frame recorded by the CCD array is then imported to Matlab (b) and each cantilever spot is marked with a box so the program can keep track of the different cantilevers. [6].

6.2 Characterization

The imprinted Topas cantilevers have a significantly different design without a paddle at the apex of the cantilever for readout. Therefore it is not given that they are compatible with the setup. A microscope picture of a chip with four gold coated cantilevers and four uncoated cantilevers is shown in Fig. 6.4. As discussed in the fabrication chapter the completely metal coated cantilevers have a small bending like the nitride cantilevers, which will make them easier to measure on in the setup.
Fig. 6.5 shows six frames taken during the alignment of one chip with cantilevers. First, the chip is aligned so the base is in focus. It is only possible to see a metal writing stating that this chip has 300 μm long cantilevers, and cantilevers are not in focus. Since the metallization process induces stress in the cantilever, this can be compensated by tilting the beam splitter. As seen in the pictures the four dots from the cantilevers can be traced and finally focused. In order to make sure that the measurements are taking place at the apex of the cantilevers the beam splitter is turned until the spots disappear. A great benefit from having slightly bend cantilevers is that the light reflected from other parts than the tip of the cantilever is greatly reduced. This can be seen by comparing Fig. 6.5(a) and Fig. 6.5(f). It is not possible to use the system for pure polymer cantilevers since the reflection of these are too small.

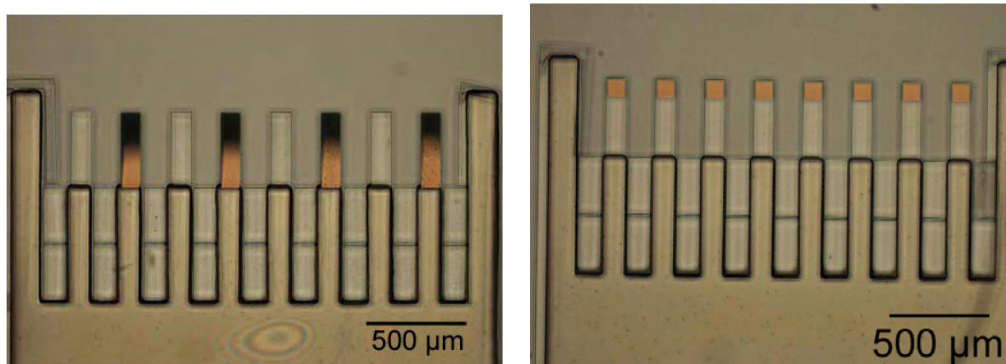

(a) Chip with complete metal coated cantilevers. (b) Chip with only metal at apex.

Figure 6.4: These two microscope pictures shows two chips with the different cantilever designs, all the cantilevers are 400 μm long 100 μm wide and 4.5 μm thick. The left chips contains four pure Topas cantilevers and four metal coated (5 nm Ti, 20 nm Au), while the right chip contains cantilevers with only metal at the apex. The color grading on the metal cantilever indicates that the cantilevers are bending.

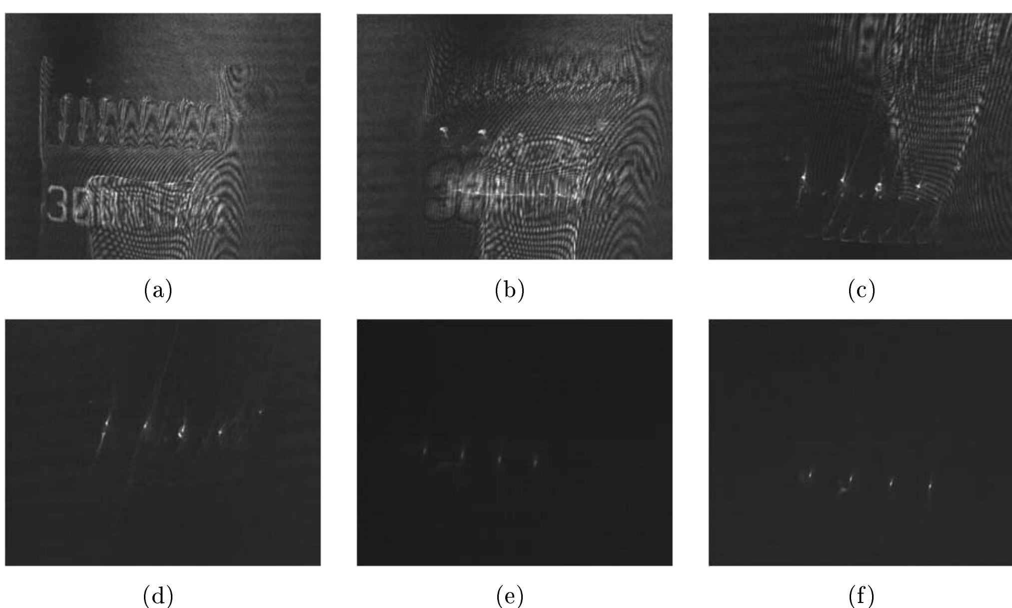

(a) (b) (c) (d) (e) (f)

Figure 6.5: These pictures shows the alignment process of the chip with four gold coated cantilevers, see Fig. 6.4. In the first picture (a) the CCD is aligned with the body chip, as the splitter is being turned the focus shifts to the metal coated cantilevers and in the last picture it is focused on the tip of the cantilever.

The alignment process for the chips with cantilevers only with metal at the apex is shown in Fig. 6.6. Since these cantilever are not as bend, it is not necessary to tilt the splitter much. As seen in Fig. 6.6(d) there are lot more noise in the picture compared to Fig. 6.5(f). However, there is a distinct reflection and spots from all

eight cantilevers are visible on a line.

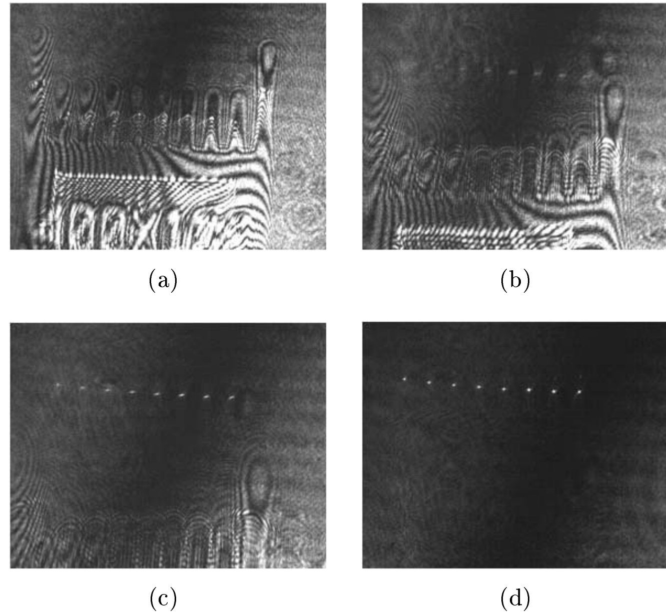

(a) (b) (c) (d)

Figure 6.6: These pictures shows the alignment process of the chip with eight cantilevers with gold at the apex, see Fig. 6.4(b). In the first picture the CCD is aligned with the body chip, as the splitter is being turned the focus shifts to the metal at the apex of the cantilevers and in the last picture it is focused on the metal pad at the apex of the cantilever. Notice how the spots from the cantilever makes an almost perfect line indicating the cantilever being almost perfectly identical in profile.

The chip is place inside a temperature controlled chamber. The chamber is kept slightly above room temperature at 25 °C to keep it stable during measurements. If the temperature is increased, the metal coated cantilevers give a strong response as shown in Fig. 6.7(a) where the temperature is raised to 27 °C and back to 25 °C. The response from the cantilever deflection corresponds to two pixels on the CCD screen, the response is shown in Fig. 6.7(a). The temperature controller gives a small overshoot which the cantilever also responds to. This is seen as a small peak in the beginning of the response. For comparison, the cantilevers with only metal at the apex gives a minimal response, as shown in Fig. 6.7(b). This is expected as most of the cantilevers only consist of Topas and therefore it should not result in a bimorph deflection.
In order to calibrate the number of pixels into an actual deflection of the cantilever, it is necessary to measure the cantilever bending. This can be done by white light interferometry at the two different temperatures. The topography acquired by the interferometer is shown in Fig. 6.8, it shows a metal coated cantilever and an uncoated cantilever. While the metal cantilever is bending the uncoated cantilever is very flat. The metal coated cantilever is bending and towards the apex of the cantilever the reflected light from the cantilever can not be collected by the interferometer.
The topography is measured both at 25 °C and at 27 °C, and the curvature of the

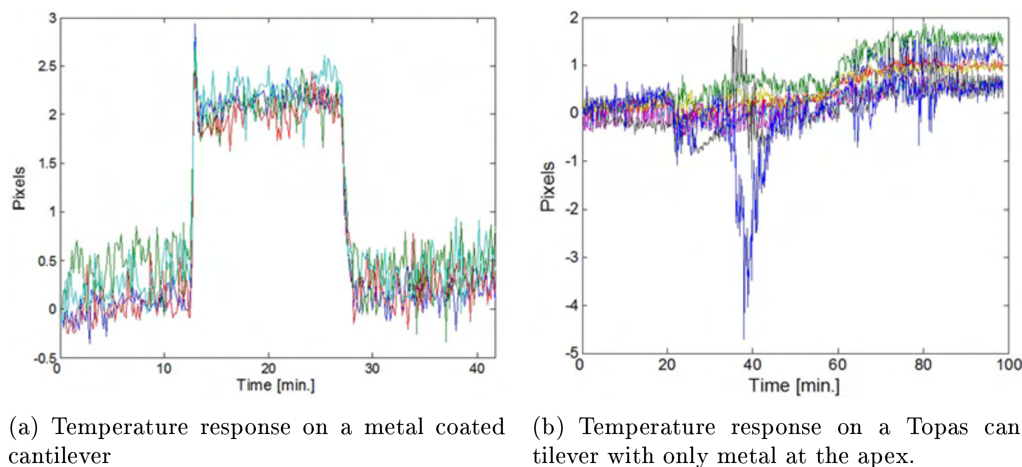

(a) Temperature response on a metal coated cantilever

(b) Temperature response on a Topas cantilever with only metal at the apex.

Figure 6.7: The temperature is initially set to 25 °C and then raised to 27 °C and then set back to 25 °C. The metal coated cantilever yields a strong signal of 2 pixels (a), while the uncoated cantilever hardly gives any response (b).

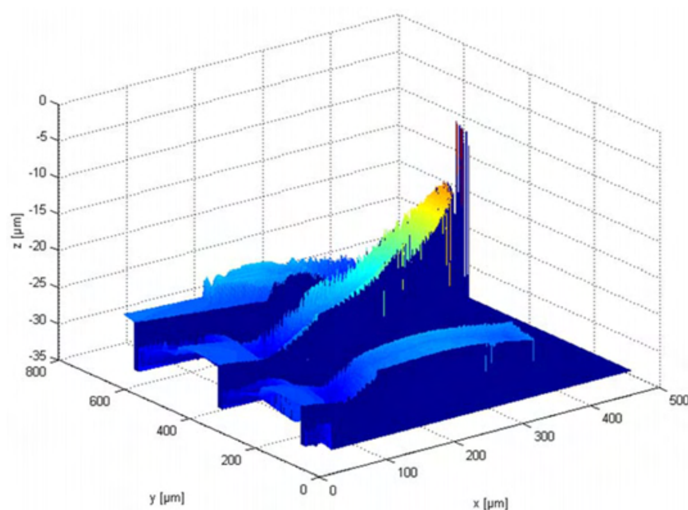

Figure 6.8: Interferometry readout at 25 °C. The topography shows two cantilevers the flat cantilever is the pure Topas cantilever while the bending cantilever is metal coated.

cantilever is plotted in Fig. 6.9. Since it was not possible to measure the entire profile with the interferometer, it is necessary to make a fit to the measurement and then extend it to the appropriate length of the cantilever used for the experiment. The measured deflection is close to what is expected theoretically.
If the cantilevers are to be used for sensing purposes out side the lab, it is important to investigate how humidity affect the cantilevers. Fig. 6.10 shows the response to humidity for the two different cantilever designs. The response to humidity is almost linear, due to problems with stray light the cantilevers with gold at the apex have a high noise level.

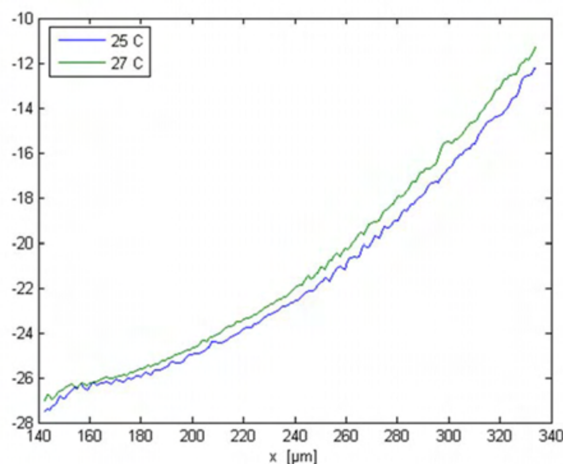

Figure 6.9: The graph shows part of the profile of the cantilever at 25 °C and 27 °C, the bending is caused by the bimorph effect.

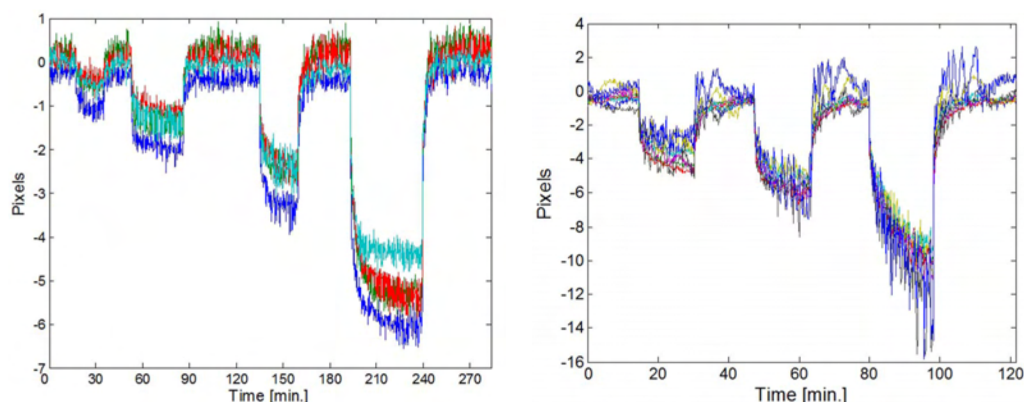

(a) Four metal coated cantilevers response to 10, 20, 40 and 80 % humidity.

(b) Eight metal coated cantilevers response to 20, 40 and 80% humidity.

Figure 6.10: The two graphs shows the reponse to different humidities for both a metal coated cantilever and polymer coated cantilever. They both show a strong response to humidity, but they also return rather quickly to the baseline after exposure.

6.3 Peptide Measurements

The cantilevers are a sensing platform, and the selectivity comes from the receptors attached to the cantilever. In this section the focus will be on peptide-based receptors and the process of attaching them to the cantilevers. The chemical receptors consist of a 12-mer peptide sequence with an OEG (oligo(ethylene glycol)) linker and a cysteine group at the end [75]. The cysteine group is important as the thiol end group it contains makes it possible to bind it to gold surfaces, see Fig. 6.11. The selectivity is achieved through hydrogen binding at the 12-mer peptide sequence which makes it possible to achieve selectivity [76]. The sequence of the peptides

can not be guessed or calculated from the target molecule, so the process of finding the right sequence is done by screening different sequences. The peptide consist of 12 amino acids and with 20 different amino acids the number of possible sequences is 20^{12} Not all the sequences can be tested but through a phage library 3.9×10^9 different combinations have been tested [75]. The target molecules for these test are TNT and DNT as these are explosive compounds and therefore of interest to be able to detect in small vapor concentrations.

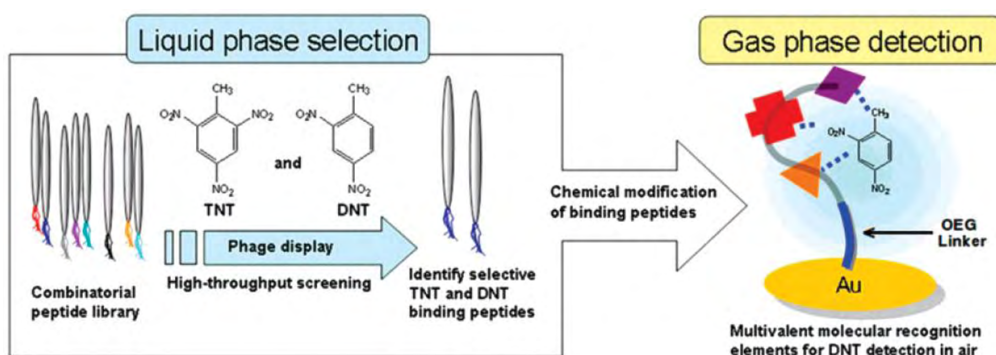

Figure 6.11: Schematic diagram showing the combinatorial peptide library and the two target molecules TNT and DNT. On the right an illustration of how the receptors are wrapped around the target with multiple hydrogen bindings and linked through the OEG to the cysteine group a gold surface [75].

In order to bind the receptors to the cantilevers a gold layer is needed. Thus only the gold coated cantilevers can be used.
The functionalization process is illustrated in Fig. 6.12. Before the functionalization the cantilevers are still sitting on the carrier wafer. As the receptors will only bind to the gold coating it is not necessary to mask the back side of the cantilever during the process and the chip can therefore be lifted off the wafer. After gold deposition the chips has gone through a series of different processing steps which has contaminated the gold surface. The next step is therefore to clean the gold surface. First the chips are placed in acetone for 5 minutes and subsequently dried in a nitrogen flow and placed inside a UV ozone oven for 5 minutes. The receptors are dissolved in milli-q water to a concentration of 1 mM, and the chips are lowered into the solution. The chips are left in the solution for 15 hours to form a continues coating on the cantilever. Finally, the chips are placed in milli-q water for 5 minutes to remove any unspecifically bound molecules. The chips are dried in nitrogen and then moved directly to the measurement chamber.
The coating process was also tested on smaller gold samples $3 \times 3\ \text{mm}^2$. The binding of the peptide was verified by XPS analyzes.
The DNT source used in the project is calibrated so it releases 214 ng/min. when placed in a oven at 80 °C. With a flow of 100 sccm of nitrogen this amounts to a concentration of 7.5 ppm from the source. The concentration can be diluted as was done for the humidity experiments, but for the first tests the maximum concentration was used. There is however one problem with the setup, because as the tubes are

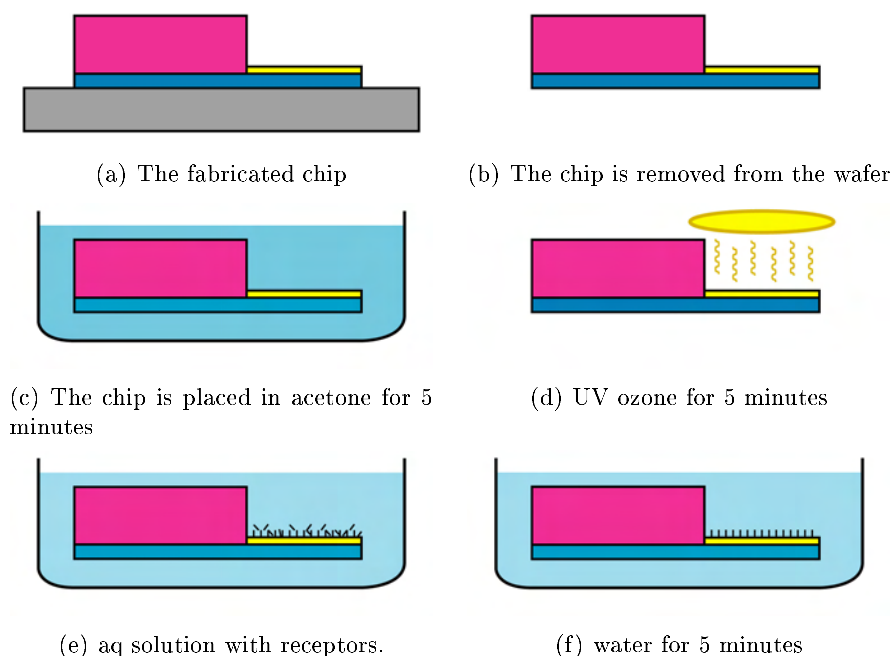

(a) The fabricated chip (b) The chip is removed from the wafer

(c) The chip is placed in acetone for 5 minutes (d) UV ozone for 5 minutes

(e) aq solution with receptors. (f) water for 5 minutes

Figure 6.12: Schematic of the functionalization of gold coated cantilevers with peptide receptors.

not heated the gas would be cooled down after the oven which makes the DNT vapors stick to tubes instead of flowing to the test chamber. This problem was tested by using a GC-MS (gas chromatography-mass spectrometer), comparing the concentration after the source and after the test chamber. It was discovered that the concentration was lowered considerably. After 2 hours only around 5 % of the DNT reaches the chamber. The problem was solved by modifying the setup. First, the tube length was minimized, and secondly heating tape was wrapped around the tubes, see Fig. 6.13. In this way more than 90 % of the explosives ends up in the chamber after 1 hour. Thus the exposures to DNT was performed for 1.5 hours, to make sure that the desired concentration has been reached.
During the coating process all the metal coated cantilevers on the chip are coated with receptors. It is therefore not possible to have a reference cantilever on the chip. To compensate for this, two chips are placed next to each other in the chamber. Fig. 6.14 shows the CCD image of the two chips inside the chamber. The CCD does not catch all the cantilevers from the two chips, but the focus was placed on reaching more than one cantilever from each chip and still have zoomed in on an area equivalent to the previous work so the same calibration could be used. This is also a test to see how well the cantilevers perform if two different chips can be measured on simultaneously in focus. As shown in the picture it was not a problem.
The measurements on a cantilever coated with DNT receptors and an uncoated cantilever are shown in Fig. 6.15(a). As the measurement takes place over several hours some drift is present. Most of the drift can be cancelled by using the reference

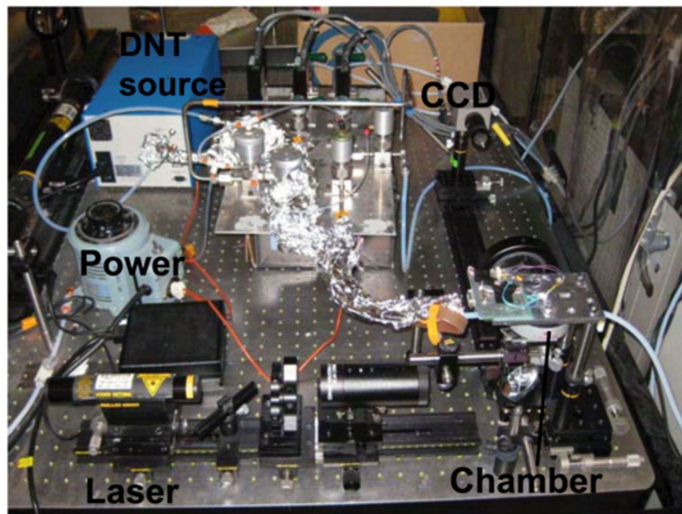

Figure 6.13: In order to use the setup for explosive vapors it is necessary to change the setup. Firstly the tube is shortened and then heated to 65 °C. The setup was also moved to an optical table to minimize noise from mechanical vibrations.

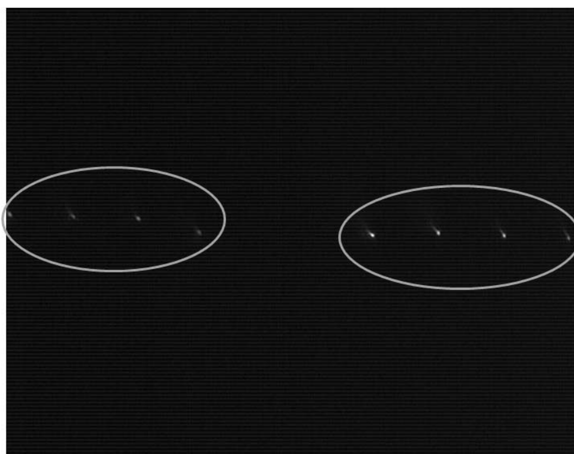

Figure 6.14: The picture shows the frame from two different chips with cantilevers. To the left is the cantilever that has been coated with receptors while the right is the uncoated reference cantilever.

cantilever, and the differential signal is shown in Fig. 6.15(b). From this a response from DNT is seen. However, it does not appear like a normal response where a saturation is achieved when all the receptors are filled after a certain time. The reference cantilever has gone through the same process as the DNT coated one with the exception that there was no receptors in aqueous functionalization solution, there is still a significant difference between the two cantilevers.
In order to make the cantilevers more alike, the reference cantilever was coated with the TNT receptor. It was shown that the selectivity should be very high and thus it should be a better reference to the DNT coated cantilever [75]. The differential

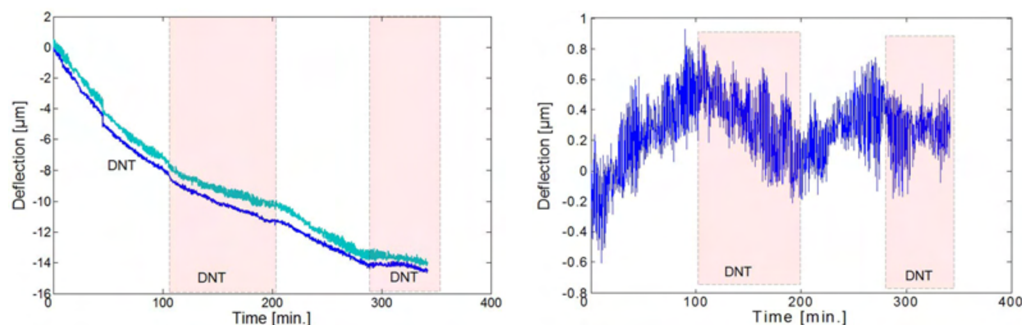

(a) Absolute response from a coated cantilever with DNT receptors (blue) and an uncoated (green).

(b) The two signal subtracted from each other.

Figure 6.15: a) shows the absolute response to DNT vapors for a cantilever coated with DNT receptor and an uncoated cantilever. b) Illustrates the two signals subtracted from each other. During the exposure to the DNT there is a change in the drift which could be intepreted as a signal. The noise is mainly due to the optical readout.

result is shown in Fig. 6.16. There does not appear to be a correlation between when the DNT vapor is introduced and bending of the cantilever.

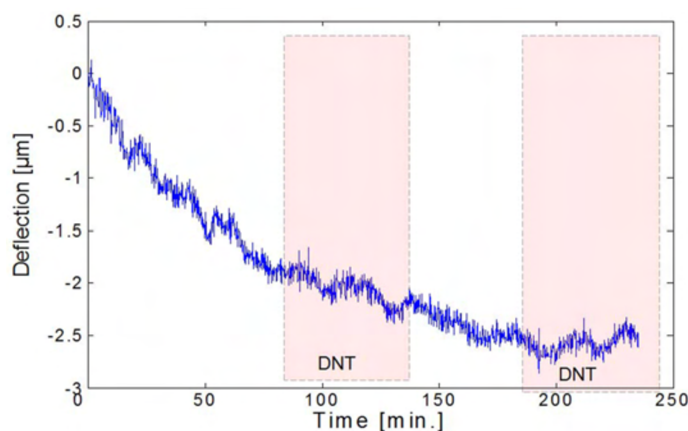

Figure 6.16: The graphs shows the differential signal between a cantilever coated with DNT receptors and one coated with TNT receptors. There does not appear to be any distinct signal from the cantilevers due to the exposure to the DNT vapors.

There are a number of possible scenarios why this is the case. It could be that the signal is too small for detection because the surface stress created in the binding process is very low and therefore the receptors are not applicable for a stress based sensor. The receptors have not been tested on silicon based cantilevers so it is not possible to say if that would work. As part of the optimization the setup was also moved to an optical table to reduce the noise but not significant improvement was achieved. The receptors have been tested on gold surface with DNT vapors in gas phase, but using the GC-MS instead of a cantilever, so the receptors work.

6.4 Summary

In this chapter all the work has been carried out at U.C. Berkeley. The chips have been tested in a setup designed for customized silicon based cantilevers. The metal coated cantilevers showed a strong response to temperature while the uncoated did not, as expected. However both metal coated and bare polymer cantilevers showed an almost linear response to changes in humidity. A protocol for functionalizing the gold coated cantilevers with peptide receptors has been developed and verified by XPS analyzes. However it was not possible to get a distinct signal from DNT binding to a cantilever.

Chapter 7

Shadow Mask and Functionalization

In the NanoNose project the specificity is supposed to come from a polymer coating. This polymer coating needs to be deposited on to the fabricated cantilever. This chapter will go through the technique developed for this purpose. First the design of the system is proposed, and then fabricated. The compatibility with the cantilevers are tested and finally the polymer coating is deposited on a silicon wafer.

7.1 Design of Shadow mask

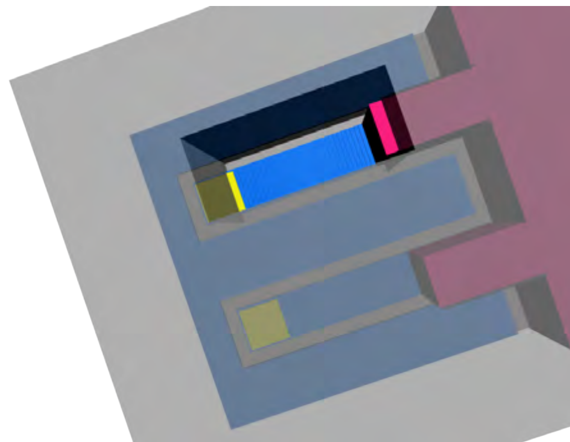

Figure 7.1: 3D illustration the cantilever sitting on the surface with the shadow mask in transparent grey on top. The shadow mask is covering everything except the area over the cantilever that is going to be functionalized.

The polymers which are going to be used for the selective coatings are synthesized by a polymerization process [77]. The process takes place inside a plasma chamber. The plasma is created by introducing argon which is ionized by a potential difference between two electrodes inside the chamber. The monomer for the polymer is intro-

duced and the argon ions initiate the polymerization process and the polymer then coats the samples placed inside the chamber. Since the coating fully covers the sample, chemical binding can not be used to selectively coat the individual cantilevers. For the NanoNose project the cantilevers on the chips should be coated with different polymers. Ideally one for each cantilever to offer a wide array of different polymers and thereby get a distinctive signal from different gasses.
It is therefore necessary to physically shield the cantilevers that do not need to be coated when depositing a polymer. One possibility would be to use photo resist to protect the cantilevers and then perform a lift-off process of the polymer. This would however require that none of the polymer coatings are dissolved during the lift off process or damaged. The process should also be performed during the fabrication, before the thick layer of SU8 is defined since it would make it impossible to spin coat the photo resist. Another possibility is to fabricate a shadow mask that fits over the chips and has an opening over the cantilever which needs to be functionalized. An animation of how this could look is presented in Fig. 7.1.
Even though the process is taking place inside a plasma chamber then it is a fairly low power plasma, a low power is chosen in order not to destroy the monomers. This also means that the directionality of the polymer deposited is poor. It is therefore important that the other cantilevers are physically protected and in contact with the mask. It is intended that the coating will take place before the cantilevers are released and lifted off the substrate. This has two advantages; first, the cantilever, are not fragile and can withstand the pressure from the shadow mask. Secondly, it also ensures that only one side is coated as the back side is still placed on the FC coating which is needed for static measurements.

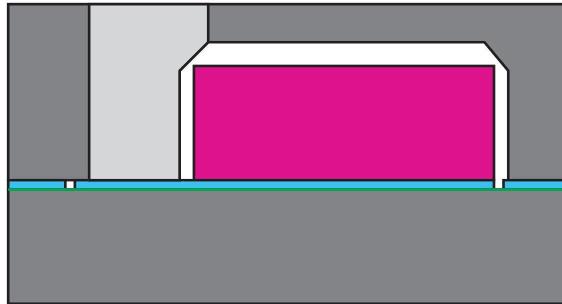

Figure 7.2: Graphical illustration of how the shadow mask fits over the cantilever chip. The light grey area represent the opening over the cantilever that is going to be functionalized. The cavity around the SU8 body is widened by a KOH etch which gives room for fitting the shadow mask over the SU8 body across an entire wafer.

Since the mask needs to come in contact with the cantilevers, the shadow mask must have cavities for the SU8 body chip. By fabricating the cavity in the shape of the SU8 body, the cavity can also be used to fix the shadow mask in the right position. An illustration from the side of how the finished shadow mask can fit over the cantilever, is shown in Fig. 7.2.
One chip has 8 cantilever. In order to functionalize each of them individually it

is necessary to fabricate 8 different shadow masks one for each cantilever. In the fabrication of the shadow mask the same UV mask can be used, but when aligned to the body chip it is moved to the cantilever that is going to be functionalized. Several cantilevers can also be functionalized at a time by exposing each of the cantilever one at a time.

7.2 Fabrication of Shadow mask

The fabrication of the shadow mask requires two masking steps, one to define the cavity and one for opening an area above the cantilever. The fabrication challenge for this part of the project is that rather large structures need to be fabricated. The first idea was just to etch the cavity first and then open the area above the cantilever. However, as illustrated in Fig. 7.3, it is very dificult to get a uniform coating of resist after the cavity has been etched. The none uniformity makes it dificult to fully develop the cantilever opening, and the difference in resist thickness gives problems during the final etching process where it can not withstand the needed etch time.

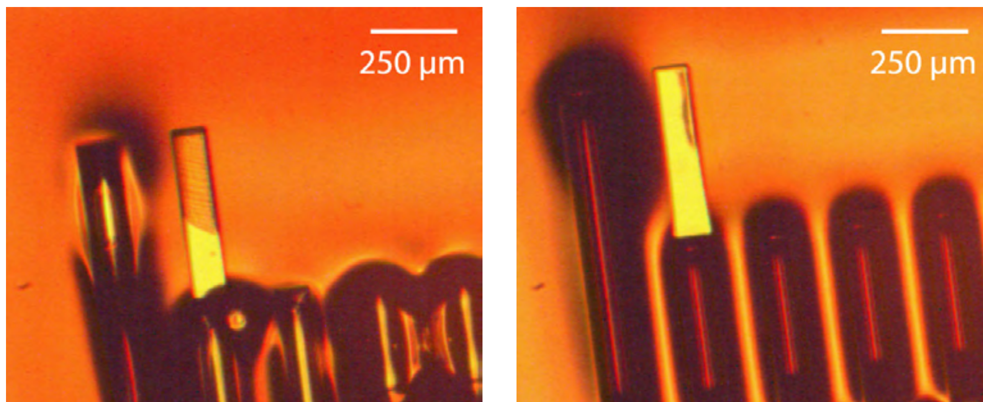

(a) Partly developed cantilever opening. (b) Almost developed cantilever opening

Figure 7.3: The cavity for the SU8 body has been etched, and a thick resist which should have been 10 μm has been spin coated. The first cantilever was then exposed and developed, but due to problem with coverage around the cavities the openings was not fully developed.

A different process flow needed to be developed where the lithographic process is performed before the deep etching on the wafer takes place. Aluminum can be used as masking material in the deep reactive ion etching process, and can easily be etched by a dedicated Al-etch or even just in NaOH, which is already used as developer for the photo resist. The cavity for the SU8 body chip can then be defined in the aluminum layer and then the opening for the cantilever can be etched using a thick layer of resist. As the wafer is unstructured there will not be problems with uniformity of the coating. The final process sequence for the shadow mask is described below and the detailed process sequence is listed in App. B.
The starting point is a double polished 525 μm thick silicon wafer. 150 nm of aluminium is evaporated on to the wafer in two steps, see Fig. 7.4(a). Between the

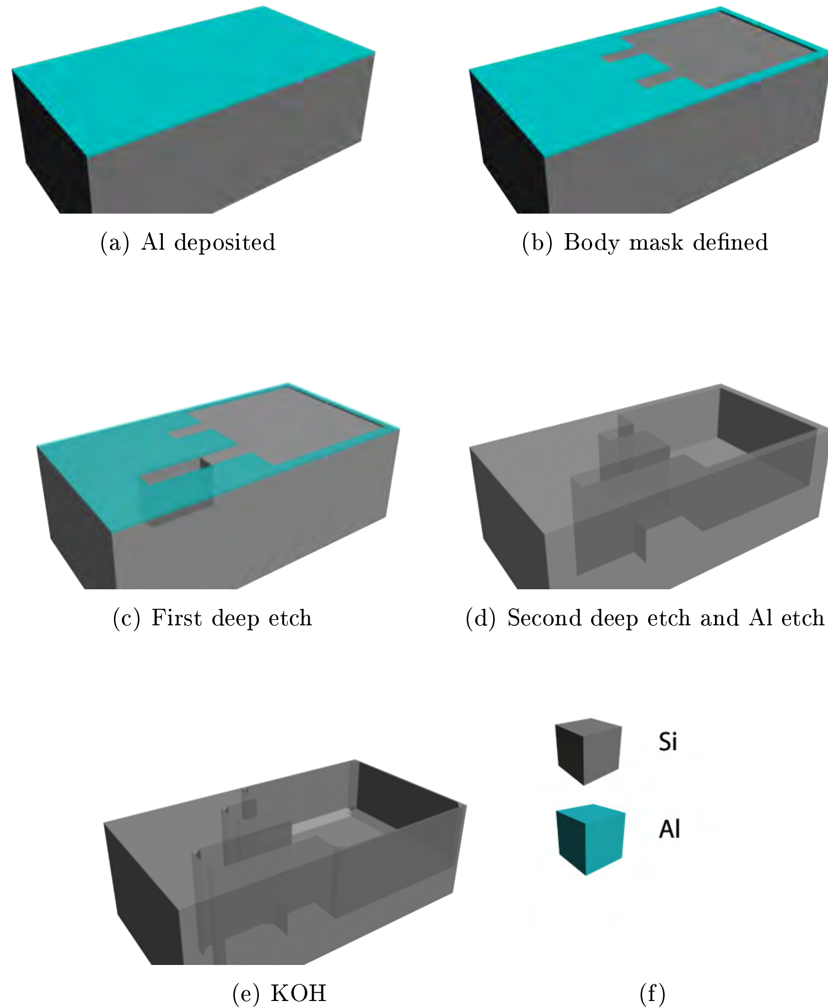

(a) Al deposited
(b) Body mask defined
(c) First deep etch
(d) Second deep etch and Al etch
(e) KOH
(f)

Figure 7.4: Graphical illustration of the process sequence for shadow mask used for functionlization. The first step is to deposit a layer of aluminum (a). The body chip is defined in the aluminum layer (b). The cantilever which is going to be functionalized is opened and etched vertically (c). In the second etch the cantilever opening is completed, and the cavity for the body chip is defined (d). In the last step the hole and cavity is widened by KOH etching (e).

two deposition the wafer is rotated in order to have metal under the pins that holds the wafer during the process. The first mask to be used is the same mask that was used for the SU8 body chip in the fabrication of the cantilever chip. 2.2 μm resist is spun on the wafer and exposed for 15 s (105 mJ/cm^2). The development of the resist in a solution of AZ 351B(NaOH) and water at a ratio of 1:5, the actual development takes about 1 minute while the etching of the aluminum takes another

3 minutes. Since the pattern has been transferred to the aluminum layer the resist can be removed again which is done in acetone, see Fig. 7.4(b).
The next step is to define which cantilever to functionalize. The photo resist also needs to protect the cavity during the etch so 10 μm of AZ4562 is spin coated on the wafer. The mask is the aligned to the cantilever, which is going to be functionalized and the resist is exposed (4 x 30s, 840 mJ/cm^2). If more than one cantilever is to be coated with the same coating then the other can subsequently be exposed. The resist is developed for 6 minutes which is also time enough for the etching of the aluminum layer.
The silicon etch is done in an ASE (Advanced Silicon Etch), the same machine that was used for depositing the FC coating. The ASE is used to etch anisotropically half way down through the wafer, see Fig. 7.4(c). In an etch time of 40 min. (185 cyc.). An average depth of 266 μm is reached. It is not necessary to etch through the wafer because the remaining etch depth can be reached in the next step. After stripping the resist, the wafer is put back into the ASE and etched for 65 min. Before the etch goes through the wafer, the etch is stopped and a carrier wafer is bonded to the shadow mask wafer using a thin 1.5 μm resist, in order to protect the machine. The etch is then continued all the way through the wafer. The carrier wafer is removed by placing it in acetone which removes the resist and the two wafers can be separated. Since the aluminum is no longer needed it is removed by 5 minutes in the developer, see Fig. 7.4(d).
The final step is a KOH etch which widens the cavity making it easier to fit it on top of the SU8 body chip. The KOH is heated to 80 °C where it has an etch rate of 1.3 μm/min.. An etch time of 30 minutes gives an easy fit to the shadow mask, where the cavity for the body chip has been increased by 35-40 μm in both sides, see Fig. 7.4(e).
Optical microscope images from the fabrication of two shadow masks, are shown in Fig. 7.5. In the first mask cantilever one and three are opened, and for the second mask cantilever six and eight are opened. Fig. 7.5(a) and Fig. 7.5(b) show the masks before they are placed in the ASE for the first time. In the cantilever opening the silicon surface is exposed whereas the rest is covered by resist. The body chip is defined in the aluminum layer, but due to the resist it looks significantly darker. Fig. 7.5(c) and Fig. 7.5(d) are taken right after completing the ASE. The cantilever openings are now holes through the wafer and the body chip is a cavity with a depth average of 332 μm. It would not be possible to fit it over the SU8 body like this, since the SU8 structures widen with about 15 μm during the processing of the thick layer. Fig. 7.5(e) and Fig. 7.5(f) shows the finished shadow masks after the aluminum has been removed and the KOH etch has been completed. The holes that were supposed to help in the stress release of the thick SU8 body, were replicated as pillars after the ASE'ing, but are dimensioned so they are removed during the KOH etch and therefore they do not interfere with the alignment of the shadow mask.
Fig. 7.6(a) shows a SEM image of a shadow mask with one opening this give a more clear illustration of how the KOH etch reveals the crystal planes of the silicon. One of the advantages with this shadow mask approach is that the functionlization takes place at wafer scale, so all the chips on the wafer can be functionalized simultaneously.

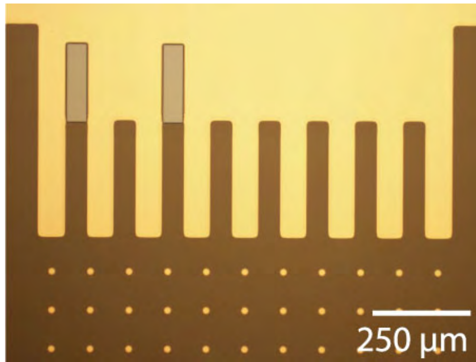

(a) Cantilever one and three are opened in the thick resist.

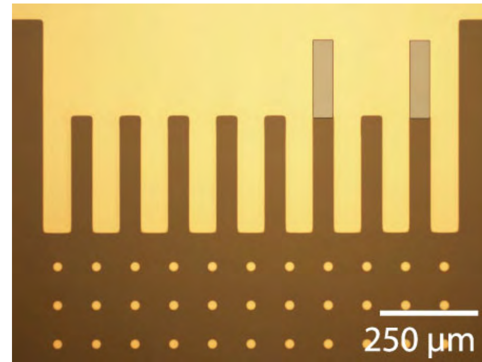

(b) Cantilever six and eight are opened in the thick resist.

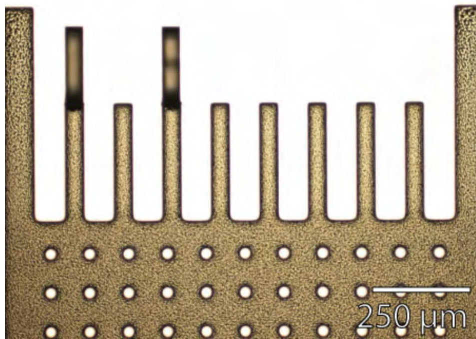

(c) After the last ASE step.

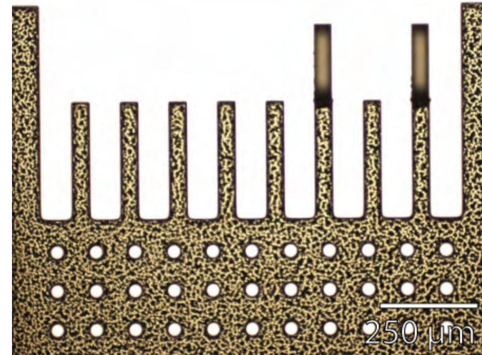

(d) After the last ASE step.

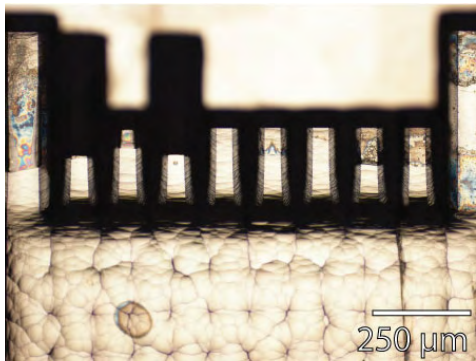

(e) Final shadow mask.

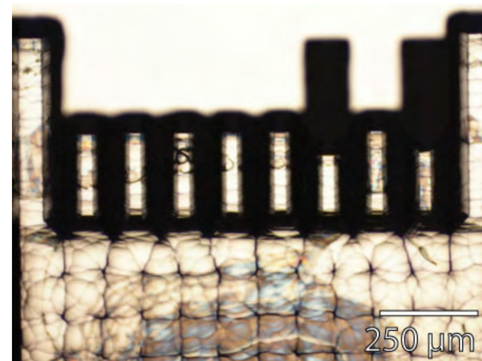

(f) Final shadow mask.

Figure 7.5: Optical microscope pictures of the fabrication of two shadow masks. The left shadow mask has openings for cantilever one and three, while the right has openings for cantilever six and eight.

Fig. 7.6(b) shows a larger area of the shadow mask where cantilever six and eight are opened.

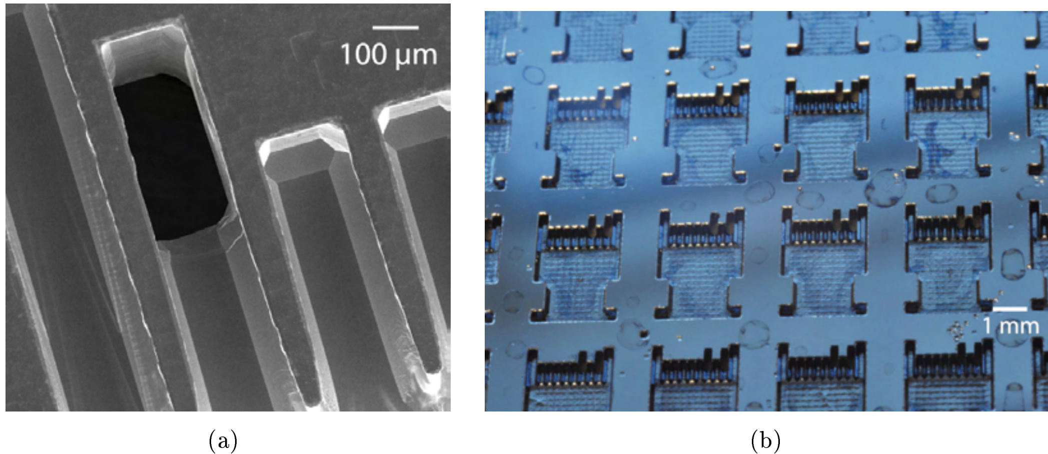

(a) (b)

Figure 7.6: Images of two shadow masks. (a) is a SEM image of a shadow mask with 1 opening over one cantilever, the SEM image makes it easy to see how the crystal planes of the silicon. (b) is a picture of a shadow mask with openings for cantilever 6 and 8.

7.3 Mechanical Alignment

The shadow mask is made so it fits right over the SU8 body of the chip with a tolerance of about 20-30 μm. Since the spacing between the cantilevers on the chip is 150 μm the alignment is sufficient. So the only challenge remaining is to align the shadow mask and the wafer with the chips to each other. The alignment marks used during the photolithographic alignment can be used, but can not be seen by the naked eye, and the same goes for the cantilevers and the holes above them. In order not to have to use a microscope for the alignment a second set of alignment marks was introduced. Fig. 7.7 shows the alignment marks for the two shadow masks fabricated with two openings. The wafer with the cantilever chips has two larger SU8 square with a metal square in the middle. The metal square is 1.5×1.5 mm^2, and the hole trough the shadow mask is 3.3×2.2 mm^2. Therefore it is possible to find and align the mask without the need for a microscope or any other tools. This makes it much easier to use, especially when the coating process does not take place in the same lab as the fabrication.

In order to check that the aligment to the cantilever is achieved the two wafers can be placed under a microscope. The picture from the microscope is shown in Fig. 7.8. The cantilever appears almost precisely in the center of the opening in the shadow mask. It is difficult to see exactly how precis because the shadow mask is out of focus, but an alignment accuracy of about 20 μm is estimated. The apex of the cantilever is not visible as it is not desired to coat the reflective pad and thereby interfere with the optical readout of the cantilever.

The shadow mask has been designed with the plasmapolymerization process in mind, but could also be used for functionalyzation by other techniques. Blagoi *et al.* has demonstrated patterning using anthraquinone photolinkers. By using the shadow mask this could be done without use of an UV-aligner [78]. As the setup looks now

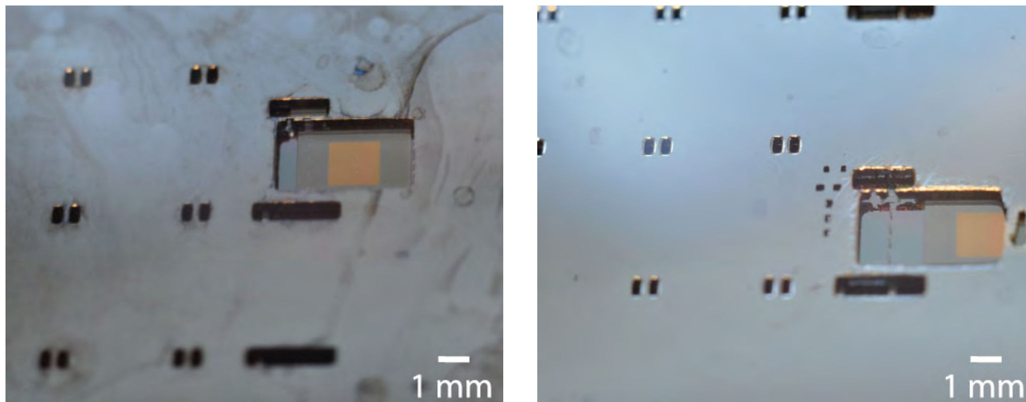

(a) Shadow mask with opening over cantilever one and three.

(b) Shadow mask with opening over cantilever six and eight.

Figure 7.7: Picture of the two different shadow masks on top of a wafer with cantilever chips.

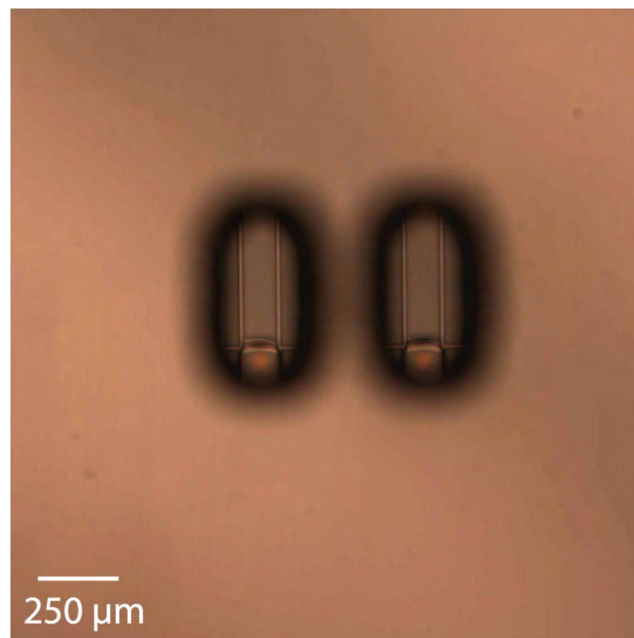

Figure 7.8: Optical microscope image of a shadow mask on top of a chip, with two open cantilevers. The cantilevers are almost precisely in the middle of the openings, and only the desired cantilever can be seen.

it is probably difficult to confine liquid in the holes over the cantilevers, but if desired, then by controlling the hydrophobicity of the stamp and the design of the chip it could be achieved.

7.4 Deposition through shadow mask

As a preliminary test before coating the cantilevers with the shadow mask, a test is performed on a blank silicon wafer, by PhD stud. Claus H. Nielsen. The shadow mask was placed on a silicon wafer and placed inside the plasma chamber where the polymer MAH (maleic anhydride) was deposited. The polymer gives a flourescent signal and it can therefore easily be seen where it is deposited. Fig. 7.9 shows the fluorescent image of MAH deposited through one of the openings. A clear signal is seen from the polymer and the signal gets little less intense in the corners, which is expected.

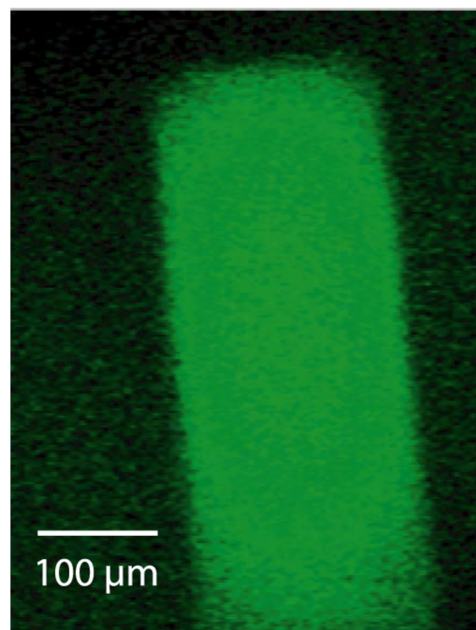

Figure 7.9: Flourescent image of polymer deposited through the shadow mask onto a bare silicon wafer.

One possible problem with this technique is that if the layer becomes too thick then the cantilever can not be released or will be damaged. If the coating will uniformly cover the cantilever, the side walls of the cantilever and the substrate thereby maybe binding it the the wafer. This was not a problem during the project, which might be due to two things. Firstly the used coatings are rather thin in the range of 10-50 nm and secondly some directionality is probably achieved when the polymer passes down the opening in the shadow mask.

7.5 Summary

In this chapter the functionalization process has been designed. By fabricating a shadow mask in silicon the fabricated chips can be functionalized on a wafer scale. The shadow mask is designed so it can be aligned to the chips without use of any

tools and with a precision of 20 μm to the cantilevers.

Chapter 8

Setup and Measurements

In this chapter the chip will be tested with a setup developed for the purpose. First, the setup is described and the first measurements on a blank cantilever are presented. Next the response from coated cantilevers are presented and compared. The effects of the surface structures are tested and finally deflection measurements with the VCSEL readout system are presented.

8.1 Setup

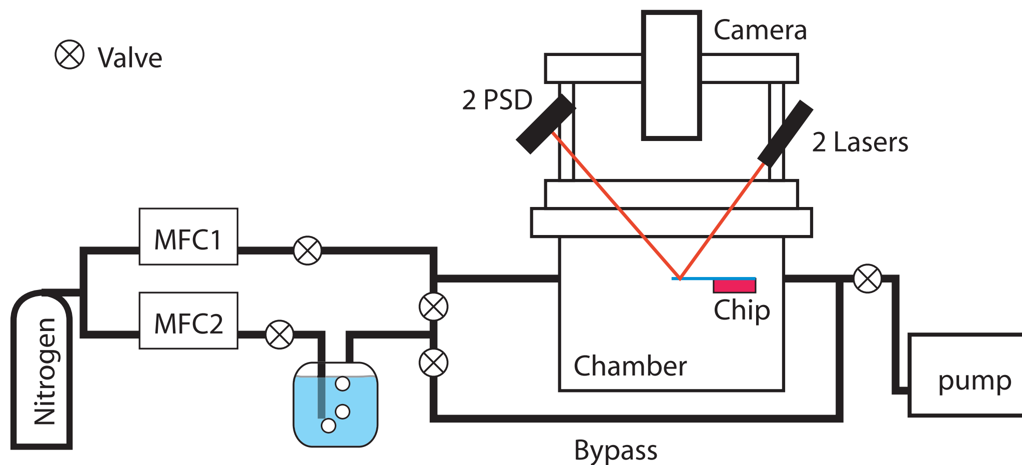

Figure 8.1: Schematic of the measurement setup. Two mass flows controllers are used to control the concentration of the vapors introduced in the chamber. By using the valves the solvent can either be directed through the bypass or in to the chamber.

In order to test the cantilever for sensing applications it is necessary to have a test setup up where the atmosphere can be controlled, and the cantilever deflection can be measured. As discussed in Sec. 1.4 the cantilevers will be measured in both dynamic and static mode, as the polymerization of a polymer onto the cantilever will give rise to a change in stress and mass. A readout scheme that allows for both techniques is

therefore required. For the NanoNose project the idea is to use a VCSEL to measure the movement of the cantilever, but as this is a new technique with some limitations especially with regards to detection range, as discussed in Sec. 2.4, a reference system is needed. The classical beam deflection technique has been used for many years in AFMs. It allows for very accurate measurements in both static and dynamic mode. Therefore this technique is chosen as the reference system.

Ideally the system should be able to measure on all eight cantilevers like in Sec. 6.1. An AFM system is however developed for the readout of one cantilever, and for the readout of each cantilever it uses one laser and one PSD (Position Sensitive Diode), both mounted on stages for alignment to the cantilevers. A compromise of just having two lasers is made, that way simultaneous measurements of two cantilever can be performed. This will enable us to measure on a coated and an uncoated cantilevers simultaneously, which has proofed to be very important for cantilever measurements [79]. The dual AFM readout was fabricated by Danish Micro Engineering A/S, which is a company that specializes in fabricating custom AFMs [80]. The AFM readout will allow us to analyze the cantilever response before using the VCSEL readout technique. A picture of the fabricated dual AFM readout is shown in Fig. 8.2.

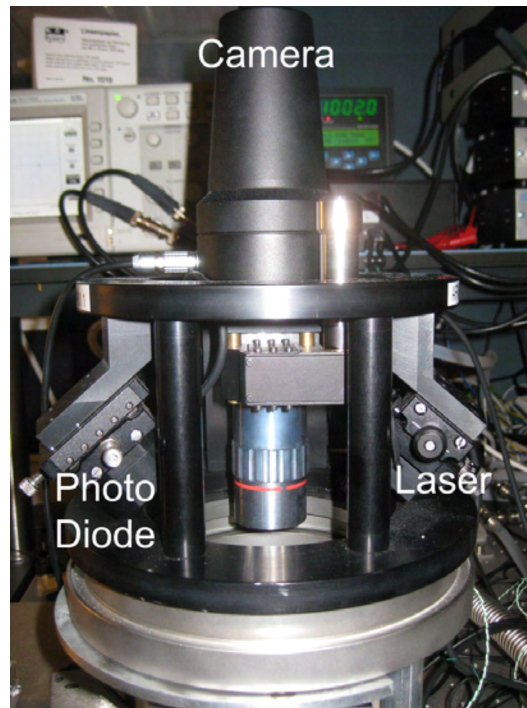

Figure 8.2: Picture of the AFM readout of the cantilevers in the chamber. In the center is a camera used during the alignment of the two AFM setups. On the right the lasers are mounted and the position sensitive diodes are placed to the left.

For many dynamic measurements it is important to be able to control the pressure. Achieving low pressure is easy by just coupling a vacuum pump to the chamber. However, since the setup has to be used for sensing purposes it is necessary to be

able to introduce different gas vapors, which will change the pressure in the chamber. The chamber will be fitted with a regulator connected to the pressure sensor and the valve between the chamber and pump. Hereby the pressure can be controlled for experiments at lower pressures.

The VCSEL readout will probably not be able to measure through the top glass lid of the chamber, and thus needs to fit inside the chamber. This puts a limitation on how small the chamber can be and also the VCSEL needs electrically shielded inputs. The finished chamber is shown in Fig. 8.3. The chamber is cylindrical shaped with an inner diameter of 15 cm and a height of 10 cm. This was estimated to be the smallest size where it is possible to place and adjust the VCSEL setup by hand. The chamber has two gas inlets and one outlet, four inlets for electrical connections which each can hold four shielded wires (16 in total), one inlet for the pressure sensor and one inlet for needle injection of samples. The electrical connections are intended for measuring with the VCSEL inside the chamber but can also be used for thermometers and other sensors.

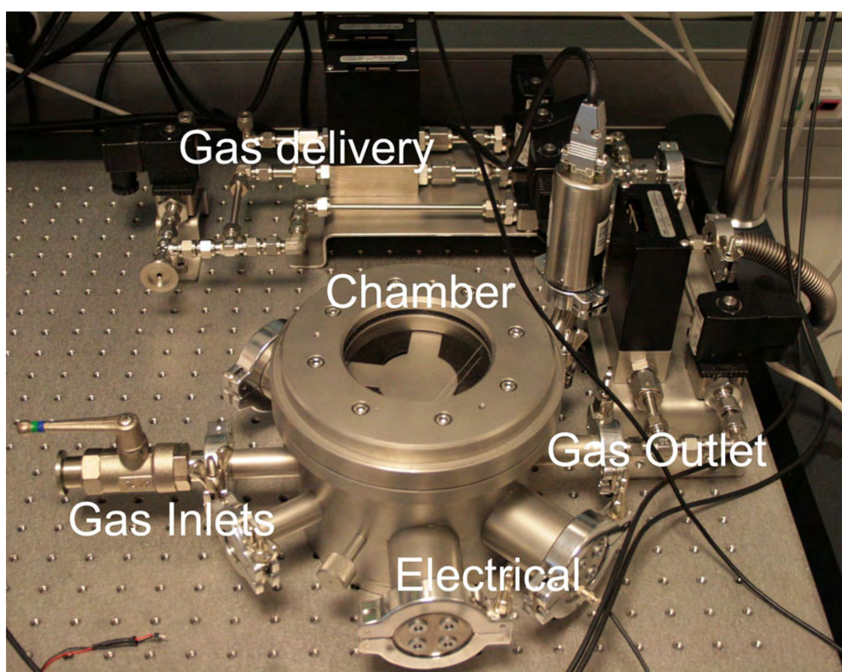

Figure 8.3: Picture of the larger vacuum chamber. The chamber has two gas inlets and one outlet, four inlets for electrical connections each can hold four shielded, one inlet for the pressure sensor and one small for needle injection of samples.

There remains one problem with the chamber, and that is the total volume. The volume of the chamber is close to 2 liters when including the space added by the connectors. Thus it would take about 20 minutes to replace the atmosphere inside the chamber even with a relative high flow of 100 sccm. It was therefore also decided to fabricate a smaller chamber, with a volume of about 1 mL as well. As the sensor is expected to work primarily at atmospheric pressure, and for the first measurements

just the AFM readout would be used, the design could be simplified significantly. Fig. 8.4 shows the fabricated chamber, which is made of aluminum. The chamber has one inlet and one outlet, a milled cavity which acts as the chamber where the chip can be fixed with two screws and a glass lid on top to close it. Since the chamber will have a constant flow through it, it is not necessary to go through a lot of effort sealing the chamber tightly. The chamber also has two holes in the bottom that make it possible to fix it on a stage for final alignment between the cantilevers and the AFM readout.

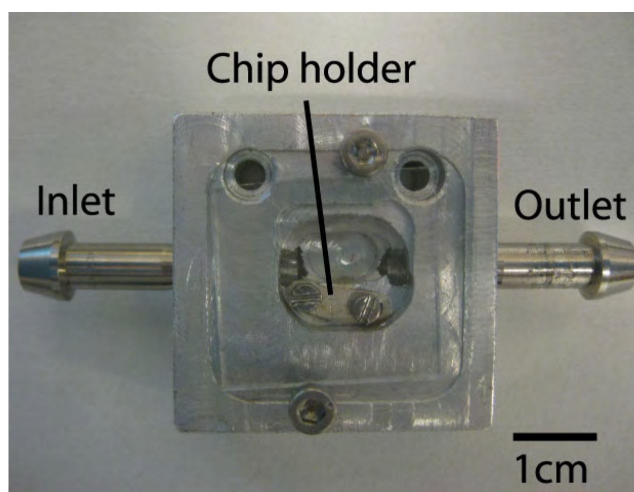

Figure 8.4: Picture of the small home made chamber for testing of the cantilevers. The small chamber can only operate at atmospheric pressure and with the AFM redout. It has a volume of about 1 mL which allows the atmosphere inside to be quickly changed.

8.2 Uncoated response

The first test is to see how the cantilever respond to water vapors or humidity without a coating. For this test a cantilever without a gold coating is used, but it does have a metal pad at the apex of the cantilever for improving the readout of the cantilever. The cantilever is 500 μm long, and has no surface structures. It is possible to detect the movement of the cantilever without metal but the noise level is higher, due to the low amount of light being reflected. The response from a single cantilever exposed to a series of increasing humidities is shown in Fig. 8.5. First, a stable baseline is achieved with a pure nitrogen flow of 50 sccm for 1 hour, during the experiment the total flow is kept constant. For 10 minutes the water vapor is introduced and then pure nitrogen for 30 minutes in which the cantilever returns almost to its original position.
In order to give a better view of the response, the graph in Fig. 8.5 is divided into the four different humidities and plotted in Fig. 8.6. The first observation is that there is a good correlation with increases in humidity. The second observation is that the cantilever almost returns to its original position before the exposure. For the lower

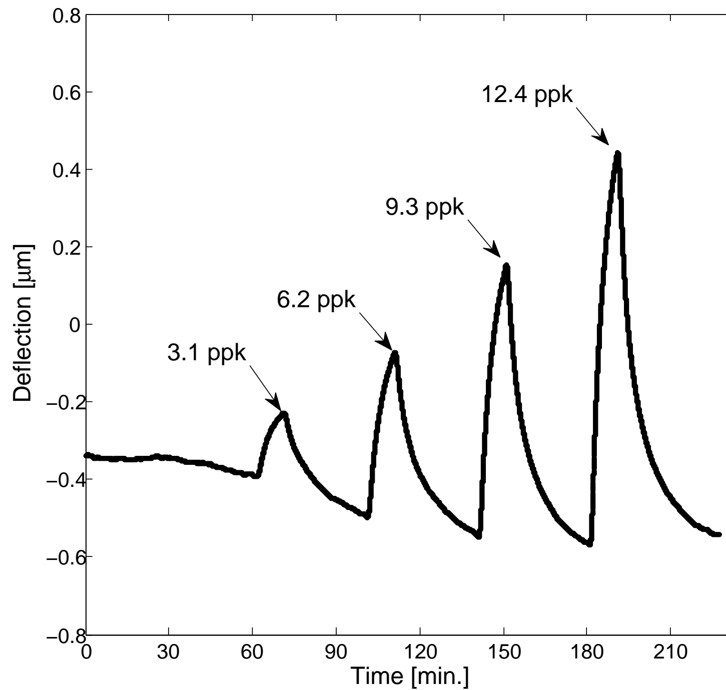

Figure 8.5: The cantilever is placed inside the chamber and changes in the humidity makes the cantilever respond even though it is not coated.

humidities the cantilever has time to return to its original position. As the humidity increases, the 30 minutes of nitrogen flow between the experiments is not sufficient time for the cantilever to return to its original position. The rather slow response might be due to condensation in the tube in this setup as the response in Chap. 6 was faster.

Since the cantilever is uncoated and made completely out of Topas it should not give a response to water. However because of the processing, the cantilever has two different sides. The bottom side has been sitting on a FC coating, while the top side has been etched by RIE. The water uptake for Topas is very small [60]. The response therefore most likely originates from the water film on the surface of the cantilever, which will be different due to the difference in hydrophobicity of the two sides.

The response to water has a strong relation to the deflection of the cantilever. In Fig. 8.7(a) the cantilever deflection after 5 and 10 minutes of exposure is plotted against the concentration. The response is almost linear to the humidity. The gradient of the response can also be used to find the concentration as shown in Fig. 8.7(b). The gradient is calculated as an average deflection over 5 and 10 minutes.

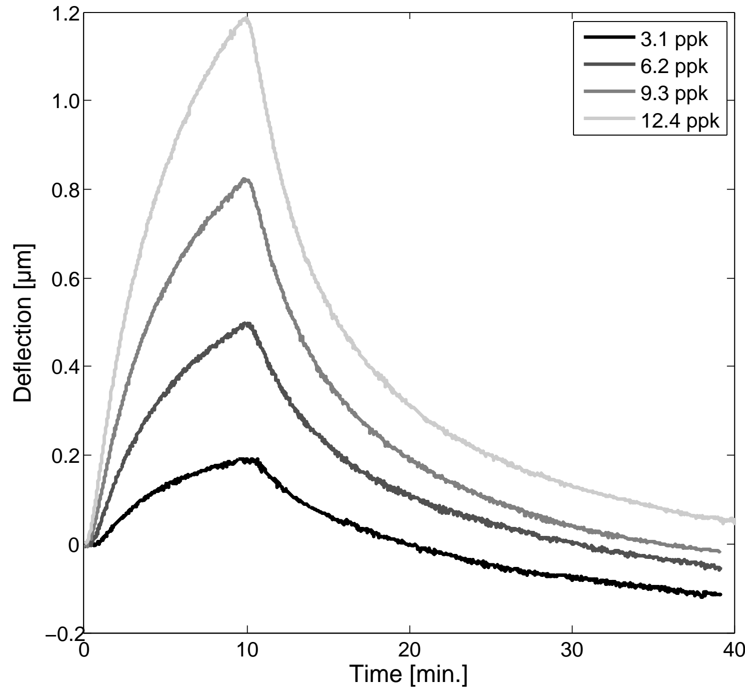

Figure 8.6: This is the response of a pure Topas cantilever to different humidities. There is a consistent relationship between an increase in concentration and deflection towards the hydrophilic side (FC).

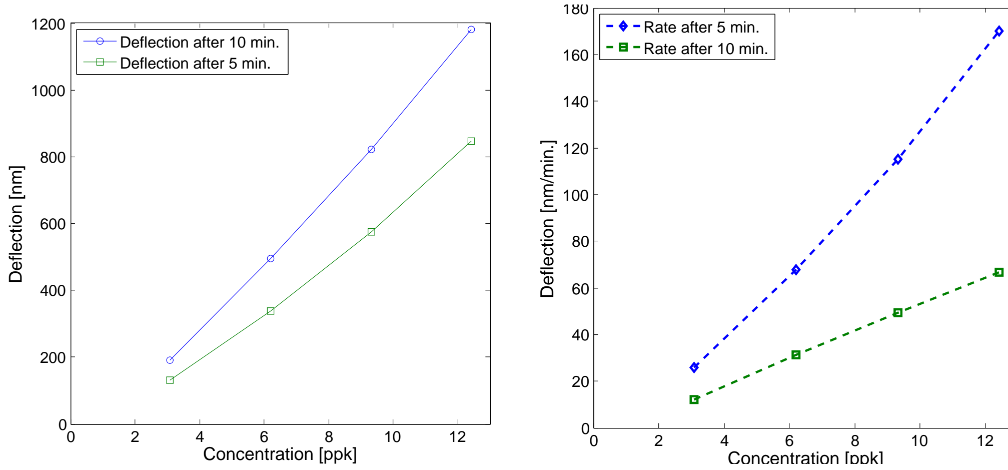

(a) Absolute deflection after 5 and 10 minutes. (b) Gradient of response after 5 and 10 minutes.

Figure 8.7: These graphs shows the relation between absolute deflection vs. concentration and average gradient vs. concentration. There is an almost linear relation between the concentration and the deflection and rate.

8.3 Coated Response

In the NanoNose project the specificity for the cantilevers is achieved by coating the cantilevers with different polymers. The different polymers that will be tested

have first been characterized using a Quartz Crystal Microbalance (QCM) system, by Claus H. Nielsen. The system has basically the same gas delivery system as described in the first section, but the chamber has space for four QCMs. For these preliminary tests with the cantilevers, the response for water and acetone will be tested. Eight different polymers have been tested using the QCM system and their response to water and acetone is shown in Fig. 8.8.

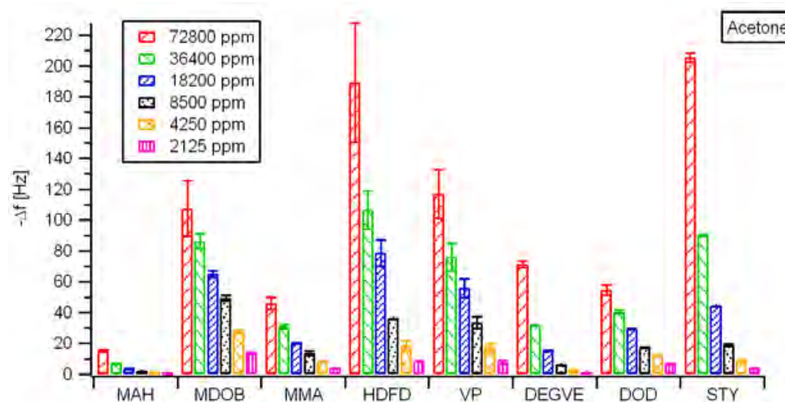

(a) QCM response to acetone. STY and VP gives some response while MAH gives almost no response.

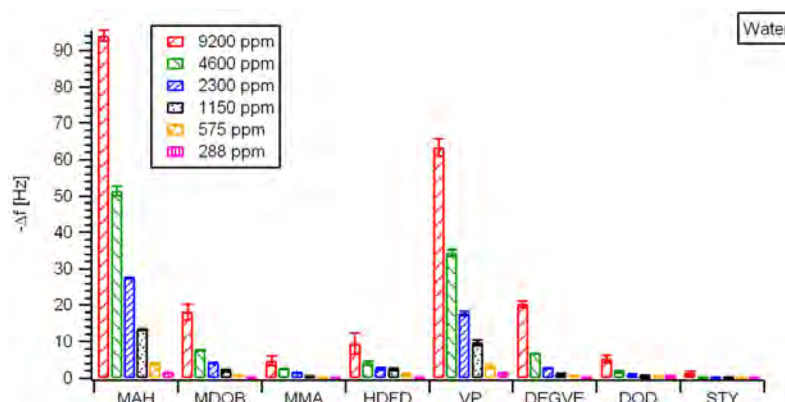

(b) QCM response to water. MAH and VP gives a large resposne while STY gives almost no response

Figure 8.8: This graph is a result of the testing performed on the coatings by Claus H. Nielsen on his QCM system. The graph shows the change in frequency when the a coated crystal is exposed to water and acetone, and it corresponds to a mass loading. For the cantilever measurements the focus will be on three polymer: MAH, VP and STY(or PS).

MAH (maleic anhydride) gives a large response to water above 90 Hz and a very small signal to acetone, and it is therefore chosen as a first candidate to test on the cantilevers. PVP (polyvinyl pyrrolidone) also gives a large response to water just above 60 Hz, while polystyrene PS gives almost no response to water. However, PS

give a larger response to acetone for higher concentrations of 210 Hz. When comparing PS and PVP responses to acetone, it should be noticed that for concentrations below 18.2 ppk PVP give a larger response than PS, but for concentrations above 36.4 ppk PS gives the largest change in frequency.

By using the shadow masking technique presented in Chap. 7 MAH is deposited on to cantilever one and three on a chip, and by using the dual AFM readout it is possible to simultaneously detect the movement of a coated and an uncoated cantilever, as they are exposed to different concentrations of water vapors. The result is shown in Fig. 8.9. The first thing to notice is that the coated cantilever has a different response to the uncoated, which clearly indicates that the cantilever surface has been changed in the process. The next thing to notice is that we see an increased bending when it is coated with the MAH. A positive deflection corresponds to a bending towards the FC coated side of the cantilever, which means that the top side where the MAH is deposited is expanding, as it would if the MAH absorbs water. From the QCM experiments it was shown that MAH gives a change in frequency corresponding to a mass increase, most likely because it absorbs water, and therefore expands in volume and bend the cantilever.

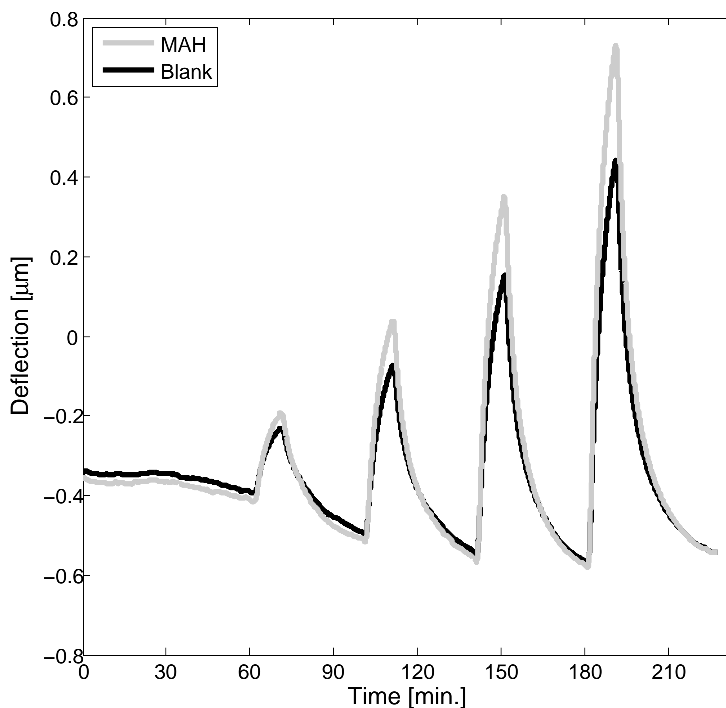

Figure 8.9: The graph shows the response from both a blank cantilever and one coated with MAH. The MAH coated cantilever gives a larger response than the uncoated as expected.

In order to make use of the reference cantilever and to be able to see a response achieved by the coating, the response from the blank cantilever is subtracted from the MAH coated cantilever. The resulting response curve is shown in Fig. 8.10. The differential response also follows concentration, so an increase in concentration result

in a larger deflection.

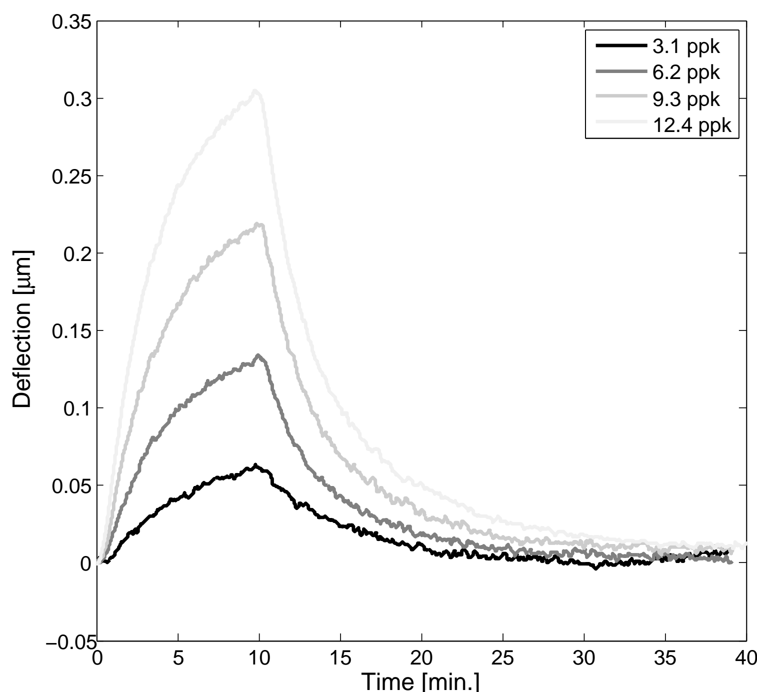

Figure 8.10: The graph shows the differential response between a cantilever coated with MAH and an uncoated cantilver. There is still a direct depending on the deflection and the concentration

Fig. 8.11(a) shows the deflection after 5 and 10 minutes with respect to concentration, the deflection shows an almost linear response the the concentration. Fig. 8.11(b) shows gradient of the response, the gradient for the first 5 minutes is larger than after 10 minutes which shows that the response is going towards a saturated response.
MAH yields a good response to water. However it requires a longer time to achieve a stable base line in the setup with nitrogen flow before the experiment, because it has a tendency to absorb water from the environment. PVP also gives a strong signal to water but has from the QCM measurements proven to be a more stable coating. Also, the response to acetone is smaller than for many other of the tested polymers. PS is a good candidate for detecting acetone. It gives a large signal to acetone while almost nothing to water.
The PVP and the PS are deposited onto the cantilever using two different shadow masks. One with openings above cantilever one and three, and one for cantilever six and eight. This will test if it is possible to deposit a series of coatings. The response of PVP and PS to acetone is shown in Fig. 8.12. Unfortunately, both the PVP coated cantilever and the PS coated cantilever gives a response to acetone. The measurement is done twice for two different concentrations. For the small concentration the PVP coating gives a larger response than PS, but for the higher concentration the response is higher for the PS. The kinetics in the absorption is not identical. For PVP, the signal returns faster back to its initial value, which could indicate that the response

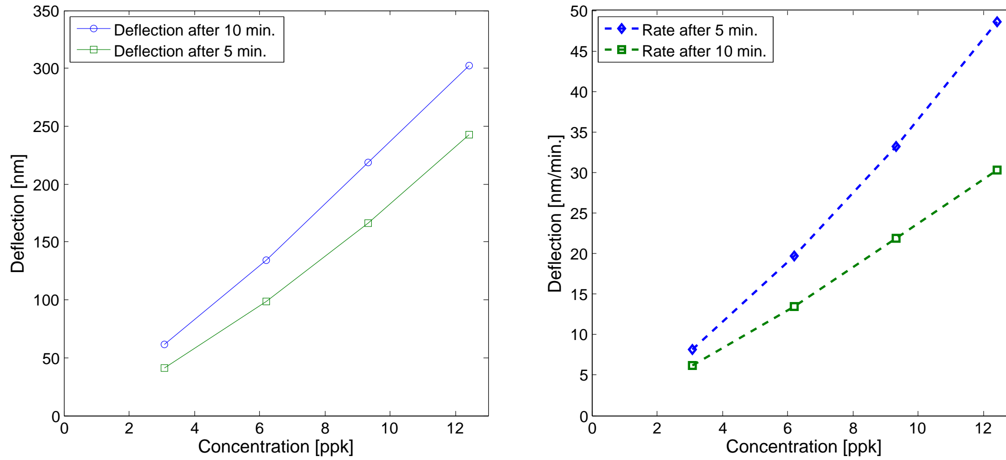

(a) Deflection vs. concentration of MAH coated cantilever minus an uncoated.

(b) Gradient vs. concentration of MAH coated cantilever minus an uncoated.

Figure 8.11: These plots shows the relation between concentration of humidity and the increase in deflection from a MAH coating on a cantilever.

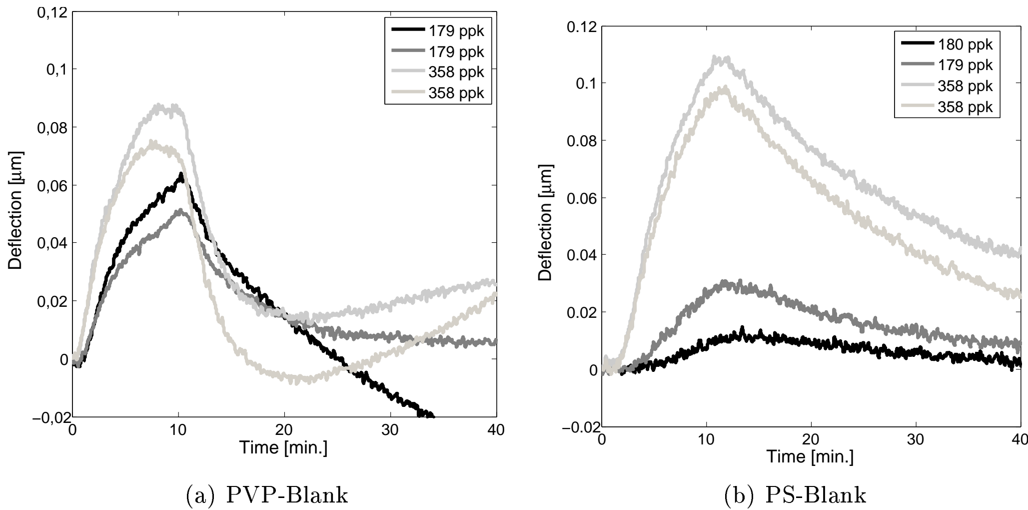

(a) PVP-Blank

(b) PS-Blank

Figure 8.12: These graphs shows the response to acetone for the PS and PVP, with an uncoated cantilever as a reference.

is more of a surface phenomenon and not due to absorption into the coating.

The response to water for PVP and PS is shown in Fig. 8.13. Like the MAH the PVP gives a strong response to water. PS gives almost no response at all to water as expected from the QCM experiments. The experiments are again repeated twice for two different concentrations. The response is very reproducible and the responses are almost identical.

Fig. 8.14 shows the collected response from three different coatings and their maximum deflection when exposed to water and acetone. When comparing the responses

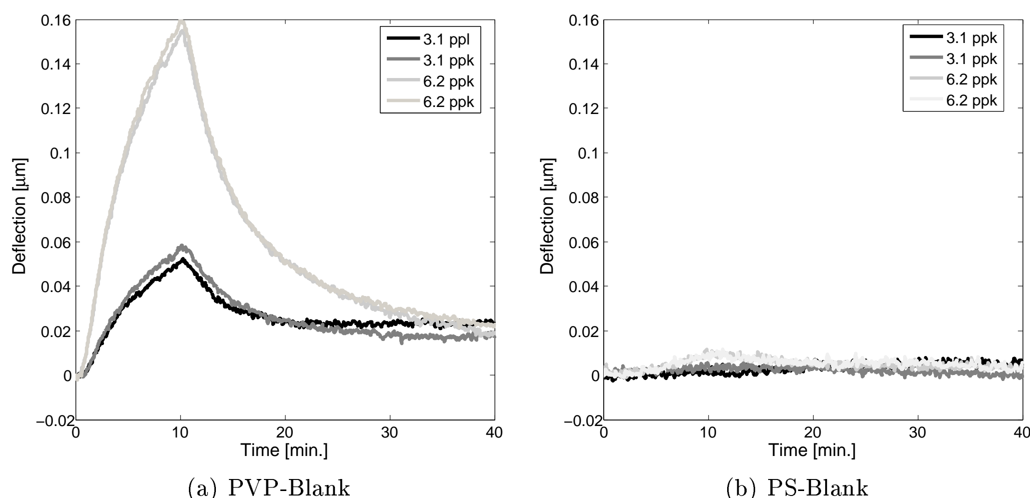

(a) PVP-Blank (b) PS-Blank

Figure 8.13: These graphs shows the response to water for the PS and PVP, with an uncoated cantilever as a reference.

to the results achieved in the QCM setup (see Fig. 8.8) there is a very clear similarity in the responses achieved with water. The responses to acetone is not as clear as for water, but the especially the high level of concentration gives a response which consistent with the QCM measurements, where PS should give the highest response.

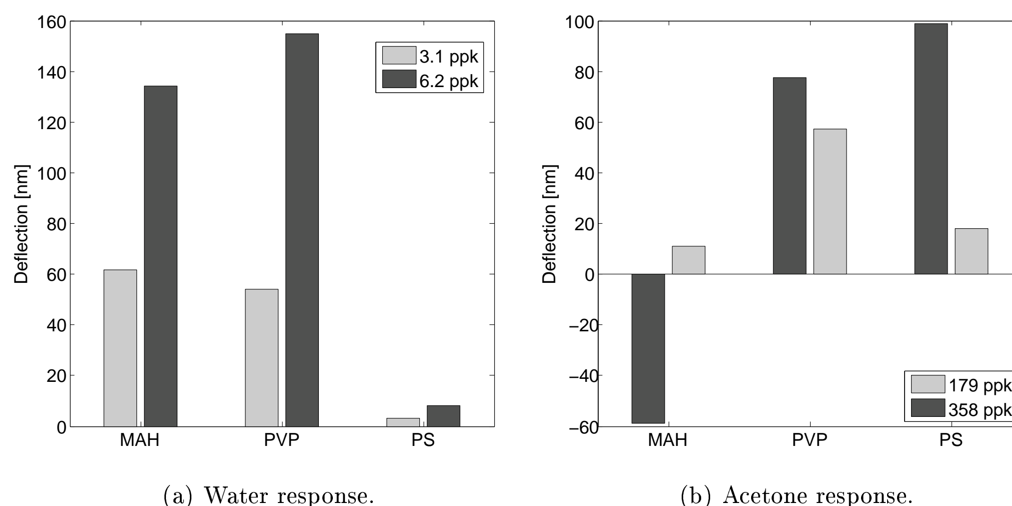

(a) Water response. (b) Acetone response.

Figure 8.14: These graphs shows the deflection after 10 minutes exposure to water and acetone for the PS, PVP and MAH, with an uncoated cantilever as a reference. The response to water is in good agreement with the results obtained on the QCM setup, with a strong response from MAH and PVP while PS gives almost no response. For the response to acetone PS do give the largest response for the highest concentration, but for the lower concentration PVP gives a higher response, This trend was also observed for the QCM measurements. The negative MAH response most be due to surface adsorption, but it has not been thoroughly tested.

8.4 Differential Measurements

The best way to compare the two coatings is by measuring simultaneously on two cantilevers coated differently on the same chip. The result from this is shown in Fig. 8.15. The graphs show the deflection of the PVP coated cantilever minus the deflection of the PS coated cantilever. Therefore water should give a positive response while acetone should result in a negative response. As expected from the individual responses to water in Fig. 8.13, the response to water gives positive and reproducible response.
For acetone, the small concentration also gives a positive response, which is also to be expected from the QCM. However, at higher concentrations the response starts being positive but then becomes negative. For higher concentrations there is a clear distinction between acetone and water. The results clearly indicate that the cantilevers have been coated with two different polymers and we conclude that it is possible to use the new shadow mask technique as proposed in Chap. 7.

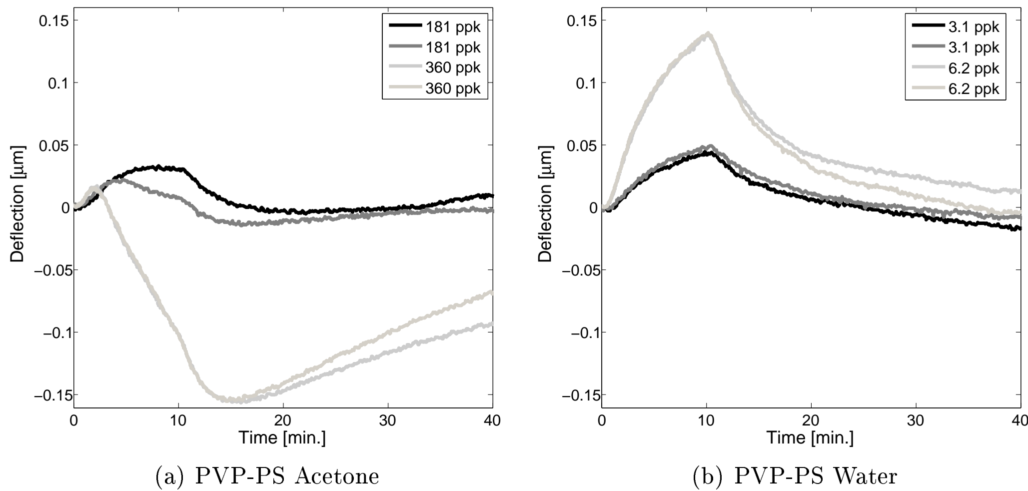

(a) PVP-PS Acetone (b) PVP-PS Water

Figure 8.15: These graphs shows differential response when the PVP-PS is exposed to Acetone and water.

In order to actually prove that the technique works on a wafer scale other chips from the same wafer were tested. They all yielded similar responses. The response from on chips is shown in Fig. 8.16. The response pattern is identical to what was observed by the first chip. The high water concentration gives a positive response and the high concentration of acetone a negative response is seen. It is therefore shown that it is possible to coat several chips simultaneously by using the shadow mask.
In order to verify the specific coating and it location on the cantilevers. The cantilevers should also be tested with other technique like the fluorescent response, XPS or other techniques.

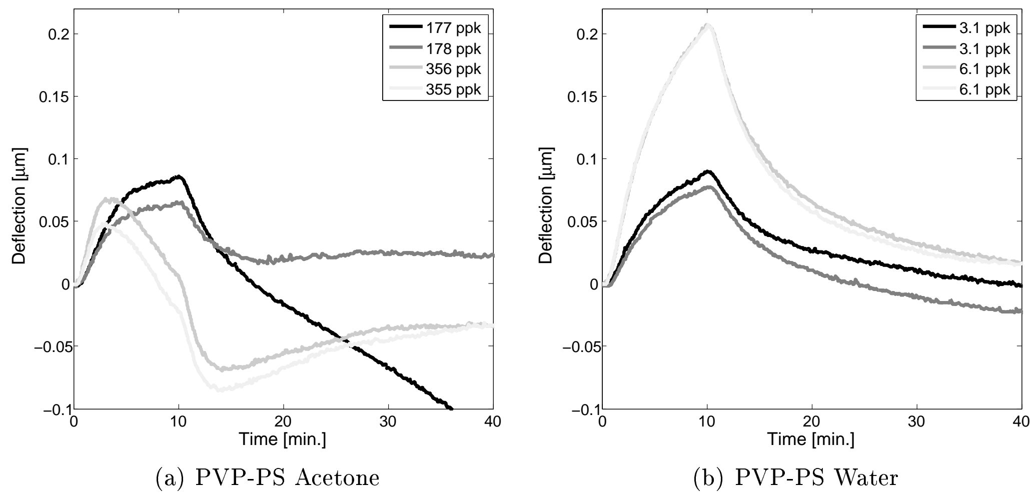

(a) PVP-PS Acetone (b) PVP-PS Water

Figure 8.16: These graphs shows the response to acetone and water for another chip from the same wafer, and thus coated in the same process as the one tested in Fig. 8.15.

8.4.1 Resonance Measurements

The coated cantilever were also tested in dynamic mode. Fig. 8.17 shows the dynamic measurement for a MDOB coated cantilever with a length of 400 μm. The cantilever is exposed to increasing water vapor concentrations four times but it is not possible to correlate a frequency change to the water vapors. The coatings is only around 20 nm thick and cantilever and therefore the added mass is going be equally small and with the poor Q-factor of the polymer cantilevers it is not possible to detect the small increase in mass with the polymer cantilever.

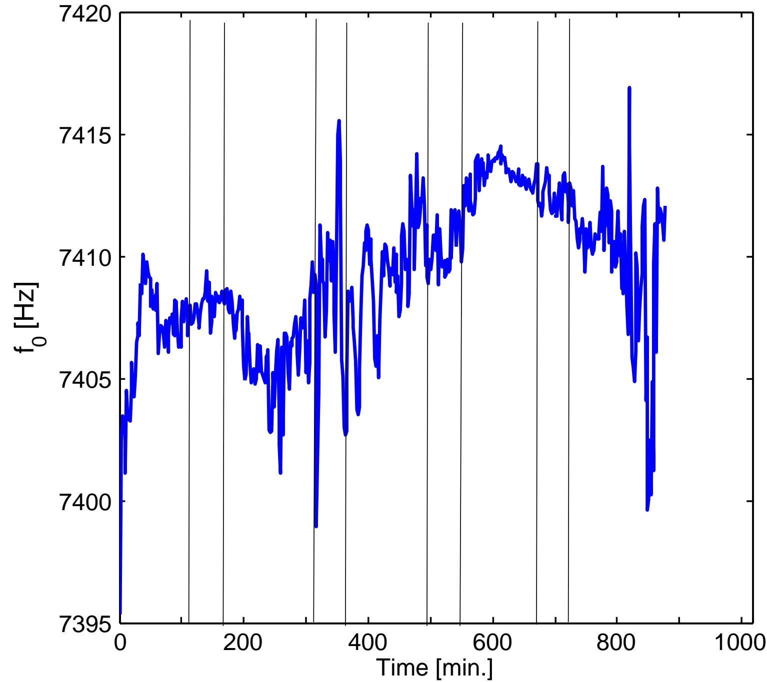

Figure 8.17: The graphs shows the resonance frequency shift for a MDOB coated cantilever. The lines indicate the intervals where the humidity is introduced. It is not possible to detect any changes. The four exposures are with increasing concentration from: 0.6 ppk, 1.2 ppk, 3 ppk and 6 ppk. In static mode a clear signal was observed for same concentrations.

8.5 Surface Structures

In order to isolate the effects of surface structures on the cantilever surface, some cantilever were designed with the ripples at a 45° angle on the cantilevers, as shown in Fig. 8.18.
The cantilevers will still bend in a normal manner, but because the ripples are at an angle they should also induce a twist in the cantilever. Fig. 8.19(a) shows the deflection of the cantilevers. The photo diodes used to detect the deflection have four segments and can therefore also measure the twisting of the cantilevers. The response from the twist has not been calibrated in the system, but the response is shown in Fig. 8.19(b). The two cantilevers twist in opposite direction as expected from the angle of the ripples.
These are just some preliminary results of the effects of surface structures. For a more detailed study different angles should be tested as well as different pitch of ripples and sizes.

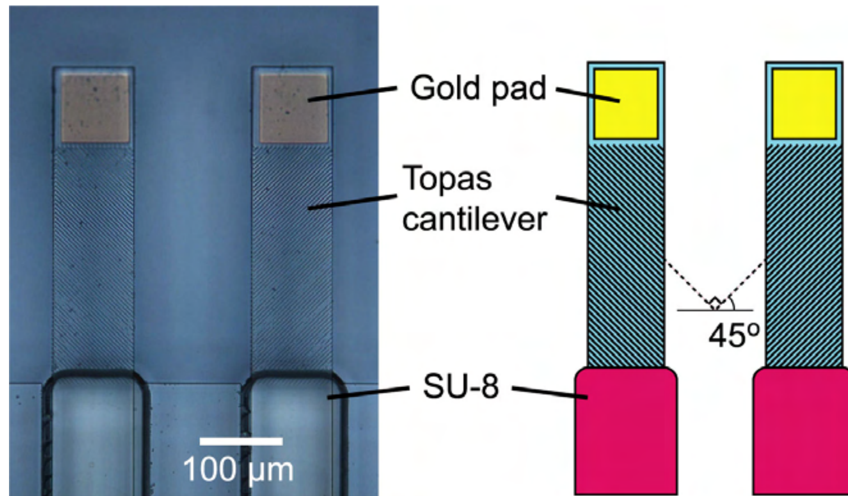

Figure 8.18: To the left is a microscope picture of the cantilevers with ripples at a angle, and to the right is an graphical illustration of it.

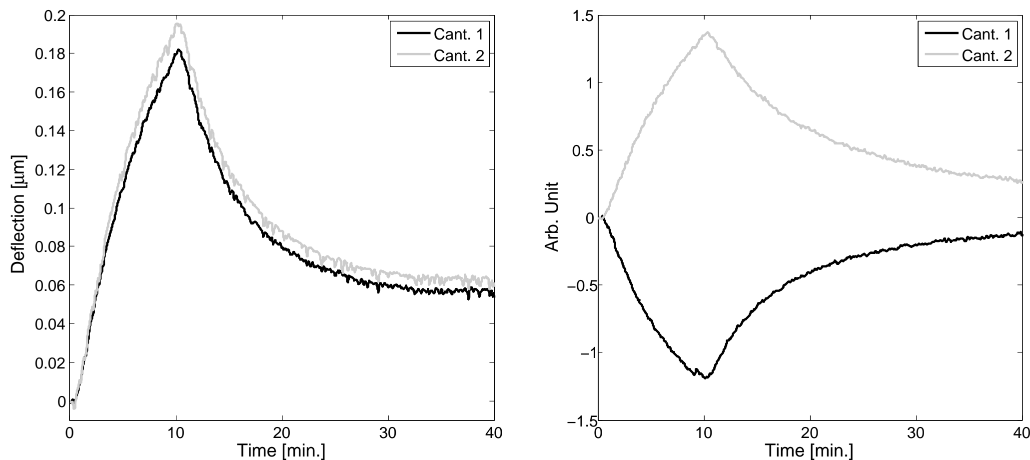

(a) Deflection for humidity of a concentration of 6.2 ppk.

(b) This graph shows the twist of the two cantilevers, and they clearly twist in opposite directions.

Figure 8.19: These graphs shows the deflection and twist of two cantilever with ripples at a 45° angle on the cantilevers. The cantilevers twists in opposite direction, because they ripples are in opposing directions, see Fig. 8.18.

8.6 VCSEL Response

In the NanoNose project it was proposed to use a VCSEL for the readout of the deflection of the cantilever, see Sec. 1.4. The principle and the theory behind this readout system was explained in the second part of Chap. 2. The first initial experiments were performed by PhD David Larsson using a commercial single-mode 850 nm VCSEL is used [81]. A Topas cantilever without metal pad is placed per-

pendicular to the emitted beam from the VCSEL. As discussed in Sec. 2.4, there is an optimal operating current around the threshold current where the relative signal response also called visibility is the largest. The visibility is calculated as follows:

$$Visibility = \frac{P_{max} - P_{min}}{P_{max} + P_{min}} \tag{8.1}$$

Fig. 8.21 shows the output power as a function of the supply current. The power transmitted through the cantilever is detected by a photo diode placed on the other side of the cantilever. The visibility is calculated for the output power and the voltage signal from the laser. Both indicate an optimal operating current around 0.98 mA.

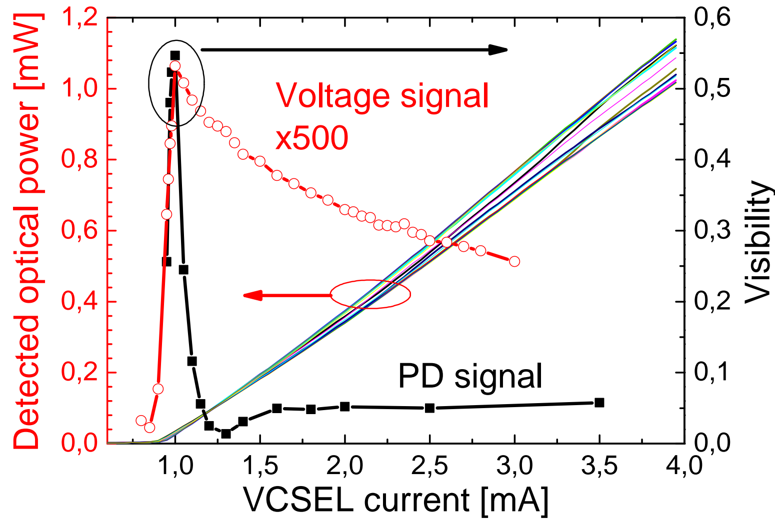

Figure 8.20: The detected optical power is plotted with respect to the supply current to the VCSEL. The visiblity of the signal is calulated and plotted for the pnoto diode signal (PD) and voltage. The optimal operating current is at the highest visibility which is at 0.98 mA

The cantilever chip is mounted on a piezo stage in order to control the displacement of the cantilever. The cantilever is placed around 35 μm from the VCSEL and moved in steps of 10 nm. The measured output power and the laser voltage are shown in Fig. 8.21. The signal also shows the periodic response which was predicted by the theory. The highest sensitivity is achieved at the steepest slope where up to 45 mV/nm is measured with in a range of $\pm$25 nm with a noise floor below 1.2 mV. Thus the sensitivity from the readout system is about 27 pm. These measurements are performed on a pure Topas cantilever without coating or metal to help the reflection.

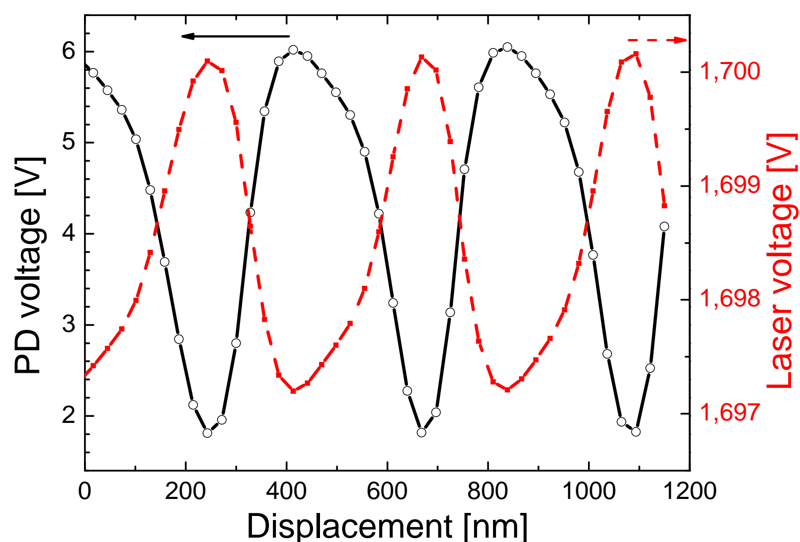

Figure 8.21: Photo diode voltage (output power) and laser voltage versus displacement of a Topas cantilever. The periodic response is related to half a wavelength of the VCSEL, the supply current is 0.98 mA.

8.7 Summary

In this chapter the setup for testing the cantilever responses to different gases was introduced, it allows for measuring two cantilever simultaneously while introducing different vapors. The coatings that have been developed by Claus H. Nielsen, was transferred to the cantilevers using the shadow masks. The responses from the coated cantilevers to water and acetone fitted well with most of the observations from the QCM measurements. It was illustrated that including surface structures on the cantilevers can affect the bending of it. Furthermore, the VCSEL can be used to perform very sensitive measurements of the position of the pure polymer cantilever down to a theoretical limit of 27 pm.

Chapter 9

Conclusion

The major goal of this thesis have been to fabricate microcantilevers by nanoimprint lithography. This goal have been fulfilled as microcantilevers with a thickness of 4.5 μm and length of 500 μm has been fabricated. By developing a shadow mask the cantilever could be functionalized by plasmapolymerization on a wafer scale. Thus the major goals of the project have been achieved.

The basic mechanics behind a cantilever with respect to end-point deflection surface stress sensitivity and the resonant frequency have been be described. Illustrating how the thickness can be around 10 times thicker for a polymer cantilever and still achieve the same sensitivity as a silicon based cantilever for static measurements due to the lower Young's modulus of the polymer material. The theory behind the special readout using self-mixing in a VCSEL have been introduced. This new readout system has great potential for sensing of cantilever deflection. However, it also has disadvantages when measuring larger deflections than a quarter wavelength. In order to take the sinusoidal signal into account a more advanced method of operating the device needs to be developed. The solution could be to measure the deflection at two positions on the cantilever thus being able to switch between the laser depending on which has the most sensitive response. The experimental results with the VCSEL setup showed that it was possible to measure the displacement of a bare Topas cantilever, and based on the noise in the system a sensitivity of 27 pm could be achieved.

In order to fabricate cantilevers by NIL it was necessary to completely redesign the mask layout for the fabrication such that a minimum amount of polymer needs to be displaced. The new design allows for much faster imprint and also improves the uniformity across the wafer. Compared to the injection molded cantilevers the thickness variation is 5 times lower. The challenge of releasing the cantilever was solved by fabricating the cantilevers on a fluorocarbon layer and coating the stamp with an FDTS coating. The stamp was used to fabricate microcantilevers in Topas, and a thick layer of SU8 was used as a support structure to finally lift the cantilevers of the substrate. Cantilevers with a length of 200-500 μm, a width 100 μm and a thickness of 4.5-5 μm were successfully fabricated with a yield of 95 %. The process was repeated more than 70 times over a span of two years, and it have proven to be a reproducible new technique.

By fabricating cantilevers using NIL, some advantages are also achieved. Structures can be implemented into the stamp and replicated on the cantilever without adding complexity to the fabrication. FIB was also used for making advanced structures in the stamp and then transferred to the cantilevers, since the stamp is reused it becomes economically liable technique. It can therefore be concluded that the technique expands the possibilities for cantilever sensing without adding additional cost and complexity in the fabrication of the cantilever.

The fabricated Topas cantilevers have been characterized by measuring static and dynamic performance. The spring constant was measured using an AFM cantilever to deflect the Topas cantilever. The average spring constant was found to be 63.1 mN/m, compared to a theoretical value of 47.4 mN/m. For the dynamic measurement there was a good agreement between the measured and the theoretical value for the frequency. However, with a Q factor of around 22 at atmospheric pressure is very low and make it basically impossible to use the cantilevers for sensing in dynamic mode.

Peptide receptors were functionalized on gold coated cantilevers but it was not possible to detect a specific signal from explosives vapors. However it was still possible to detect temperature and humidity responses with a setup designed for silicon based cantilever with a collimated laser beam and a CCD array.

Plasma-polymerized polymers were successfully deposited on to individual cantilevers on a wafer scale, and thereby it is possible to coat 300 chips simultaneously. A shadow mask has been fabricated in silicon and it fits mechanically over the cantilever chips. It can be aligned with a precision of 20 μm without use of any tools or microscope.

A setup for testing the cantilever responses to different gases has been built. It allows for measuring two cantilevers simultaneously while introducing different vapors. Using the functionalized cantilevers it was possible to get a response from the coatings and it was possible to distinguish between water and acetone. The responses was in good agreement with the observations from QCM measurements.

9.1 Outlook

Future work on this would be to optimize the surfaces of the bare cantilevers so they become more identical and less responsive to humidity and other solvents, and thus making it easier to compare the signals from the coated cantilevers. It could also be interesting to replace the SU8 support with a more inert material.

It was not possible to make a solid conclusion based on the measurements with the rippled cantilevers. The effect could be more systematically studied in the future, trying to identify optimal structures for surface stress detection and for reflection of laser light.

Future work would also include adding more coatings, using the eight cantilevers in the array and have a different coating for each of them. Thereby enabling the sensor to distinguish between different vapors and hopefully also mixtures.

The fabrication technique could also potentially be expanded to fabricate cantilever of other materials such biopolymers and other polymers which can not be patterned

by UV. By fabricating cantilever of biopolymer or combination of biopolymers and other polymers different physical properties could be investigated in a very precis and sensitive manner.
The shadow masking technique could also be used for functionalizing other surface coatings on to the Topas cantilever. It could also be expanded to coat cantilever which was not fabricated by this technique like the SU8 cantilevers.

Bibliography

[1] S. M. Mahmud and A. I. Alrabady. A new decision-making algorithm for airbag control. *Ieee Transactions on Vehicular Technology*, 44(3):690–697, 1995.

[2] M. McCulloch, T. Jezierski, M. Broffman, A. Hubbard, K. Turner, and T. Janecki. Diagnostic accuracy of canine scent detection in early- and late-stage lung and breast cancers. *Integrative Cancer Therapies*, 5(1):30–39, 2006.

[3] K. Mew. Airport security screening: Privatize or federalize. *Public Works Management Policy*, 2005; 10; 3.

[4] L. M. Collins, Y. Zhang, J. Li, H. Wang, L. Carin, S. J. Hart, S. L. Rose-Pehrsson, H. H. Nelson, and J. R. McDonald. A comparison of the performance of statistical and fuzzy algorithms for unexploded ordnance detection. *Ieee Transactions on Fuzzy Systems*, 9(1):17–30, 2001.

[5] N. H. Pontoppidan, S. Sigurdsson, and J. Larsen. Condition monitoring with mean field independent components analysis. *Mechanical Systems and Signal Processing*, 19(6):1337–1347, nov 2005.

[6] S. H. Lim, D. Raorane, S. Satyanarayana, and A. Majumdar. Nano-chemo-mechanical sensor array platform for high-throughput chemical analysis. *Sensors and Actuators B-Chemical*, 119(2):466–474, 2006.

[7] G. Binnig, C.F. Quate, and C. Gerber. Atomic force microscope. *Physical Review Letters*, 56(9):930–933, 1986.

[8] J. Thaysen, A. Boisen, O. Hansen, and S. Bouwstra. Atomic force microscopy probe with piezoresistive read-out and a highly symmetrical wheatstone bridge arrangement. *Sensors and Actuators A: Physical*, 83(1-3):47–53, 2000.

[9] M. Tortonese, R. C. Barrett, and C. F. Quate. Atomic resolution with an atomic force microscope using piezoresistive detection. *Applied Physics Letters*, 62(8):834–836, 1993.

[10] S. C. Minne, S. R. Manalis, and C. F. Quate. Parallel atomic force microscopy using cantilevers with integrated piezoresistive sensors and integrated piezoelectric actuators. *Applied Physics Letters*, 67(26):3918–3920, 1995.

[11] F. J. Norton. U. s. patent no. 2,307,800. Patent, 1943.

[12] A. Boisen, J. Thaysen, H. Jensenius, and O. Hansen. Environmental sensors based on micromachined cantilevers with integrated read-out. *Ultramicroscopy*, 82(1-4):11–16, 2000.

[13] H. J. Butt. A sensitive method to measure changes in the surface stress of solids. *Journal of Colloid and Interface Science*, 180(1):251–260, 1996.

[14] H. P. Lang, R. Berger, C. Andreoli, J. Brugger, M. Despont, P. Vettiger, Ch Gerber, J. K. Gimzewski, J. P. Ramseyer, E. Meyer, and H. J. Guntherodt. Sequential position readout from arrays of micromechanical cantilever sensors. *Applied Physics Letters*, 72(3):383–385, 1998.

[15] J.R. Barnes, R.J. Stephenson, C.N. Woodburn, S.J. O'Shea, M.E. Welland, T. Rayment, J.K. Gimzewski, and C. Gerber. A femtojoule calorimeter using micromechanical sensors. *Review of Scientific Instruments*, 65(12):3793–3798, 1994.

[16] J. R. Barnes, R. J. Stephenson, M. E. Welland, C. Gerber, and J. K. Gimzewski. Photothermal spectroscopy with femtojoule sensitivity using a micromechanical device. *Nature*, 372(6501):79–81, 1994.

[17] D. C. Yi, A. Greve, J. H. Hales, L. R. Senesac, Z. J. Davis, D. M. Nicholson, A. Boisen, and T. Thundat. Detection of adsorbed explosive molecules using thermal response of suspended microfabricated bridges. *Applied Physics Letters*, 93(15):3, 2008.

[18] L. R. Senesac, D. Yi, A. Greve, J. H. Hales, Z. J. Davis, D. M. Nicholson, A. Boisen, and T. Thundat. Micro-differential thermal analysis detection of adsorbed explosive molecules using microfabricated bridges. *Review of Scientific Instruments*, 80(3):9, 2009.

[19] Matthieu Guirardel, Liviu Nicu, Daisuke Saya, Sary Hinh, Julien Sicard, Denis Lagrange, Fabrice Mathieu, Eric Cattan, Denis Remiens, and Christian Bergaud. *Proceedings of the 2004 IEEE International Frequency Control Symposium and Exposition. A Conference of the IEEE Ultrasonics, Ferroelectrics, and Frequency Control Society (UFFC-S) and Proceedings of the IEEE International Frequency Control Symposium and Exposition*, pages 317–320, 2005.

[20] B. J. Theaker, Z. Ali, T. Sarkodie-Gyan, and W. T. O. Hare. Gas-sensing system using an array of coated quartz crystal microbalances with a fuzzy inference system. *Journal of Thermal Analysis and Calorimetry*, 55(2):371–381, 1999.

[21] Cantion. http://www.cantion.com/. Internet, 2006.

[22] Concentrís. http://www.concentris.com. Internet, 2009.

[23] Protiveris. http://www.protiveris.com/. Internet, 2006.

[24] W. M. Shu, D. S. Liu, M. Watari, C. K. Riener, T. Strunz, M. E. Welland, S. Balasubramanian, and R. A. McKendry. Dna molecular motor driven micromechanical cantilever arrays. *Journal of the American Chemical Society*, 127(48):17054–17060, 2005.

[25] http://www.micromotive.de/. Micromotive gmbh, 2009.

[26] A. Boisen and T. Thundat. Design & fabrication of cantilever array biosensors. *Materials Today*, 12(9):32–38, 2009.

[27] G. Genolet, J. Brugger, M. Despont, U. Drechsler, P. Vettiger, N. F. de Rooij, and D. Anselmetti. Soft, entirely photoplastic probes for scanning force microscopy. *Review of Scientific Instruments*, 70(5):2398–2401, 1999.

[28] M. Nordstrom, S. Keller, M. Lillemose, A. Johansson, S. Dohn, D. Haefliger, G. Blagoi, M. Havsteen-Jakobsen, and A. Boisen. Su-8 cantilevers for bio/chemical sensing; fabrication, characterisation and development of novel read-out methods. *Sensors*, 8(3):1595–1612, 2008.

[29] Andrew W. McFarland, Mark A. Poggi, Lawrence A. Bottomley, and Jonathan S. Colton. Injection moulding of high aspect ratio micron-scale thickness polymeric microcantilevers. *Nanotechnology*, 15(11):1628–1632, 2004.

[30] Andrew W. McFarland, Mark A. Poggi, Lawrence A. Bottomley, and Jonathan S. Colton. Production and characterization of polymer microcantilevers. *Review of Scientific Instruments*, 75(8):2756–2758, 2004.

[31] A. W. McFarland and J. S. Colton. Chemical sensing with micromolded plastic microcantilevers. *Microelectromechanical Systems, Journal of*, 14(6):1375–1385, 2005.

[32] A. W. McFarland, M. A. Poggi, L. A. Bottomley, and J. S. Colton. Injection-moulded scanning force microscopy probes. *Nanotechnology*, 16(8):1249–1252, 2005.

[33] M. K. Baller, H. P. Lang, J. Fritz, Ch Gerber, J. K. Gimzewski, U. Drechsler, H. Rothuizen, M. Despont, P. Vettiger, F. M. Battiston, J. P. Ramseyer, P. Fornaro, E. Meyer, and H. J. Guntherodt. A cantilever array-based artificial nose. *Ultramicroscopy*, 82(1-4):1–9, 2000.

[34] Thomas A. Betts, Christopher A. Tipple, Michael J. Sepaniak, and Panos G. Datskos. Selectivity of chemical sensors based on micro-cantilevers coated with thin polymer films. *Analytica Chimica Acta*, 422(1):89–99, 2000.

[35] Stephen D. Senturia. *Microsystem Design*, volume 4. KAP, 2002.

[36] R. G. Budynas W. C. Young and R. J. Roark. *Roark's formulas for stress and strain*, volume 7. McGrawHill., Boston,, 2002.

[37] Peter A. Rasmussen. *Cantilever-based Sensors for Surface Stress Measurements*. Phd-thesis, Technical University of Denmark, 2006.

[38] Joseph T. Verdeyen. *Laser Electronics*. Prentice Hall, 3 edition, 1995.

[39] A. Hsu, J. F. P. Seurin, S. L. Chuang, and K. D. Choquette. Optical feedback in vertical-cavity surface-emitting lasers. *Ieee Journal of Quantum Electronics*, 37(12):1643–1649, 2001.

[40] W. M. Wang, K. T. V. Grattan, A. W. Palmer, and W. J. O. Boyle. Self-mixing interference inside a single-mode diode-laser for optical sensing applications. *Journal of Lightwave Technology*, 12(9):1577–1587, 1994.

[41] W. M. Wang, W. J. O. Boyle, K. T. V. Grattan, and A. W. Palmer. Self-mixing interference in a diode-laser - experimental-observations and theoretical-analysis. *Applied Optics*, 32(9):1551–1558, 1993.

[42] S. Y. Chou, P. R. Krauss, and P. J. Renstrom. Imprint of sub-25 nm vias and trenches in polymers. *Applied Physics Letters*, 67(21):3114–3116, 1995.

[43] http://www.intel.com/. Intel, 2009.

[44] http://www.itrs.net/. International technology roadmap for semiconductors, 2009.

[45] M. D. Austin, H. X. Ge, W. Wu, M. T. Li, Z. N. Yu, D. Wasserman, S. A. Lyon, and S. Y. Chou. Fabrication of 5 nm linewidth and 14 nm pitch features by nanoimprint lithography. *Applied Physics Letters*, 84(26):5299–5301, 2004.

[46] N. Chaix, C. Gourgon, C. Perret, S. Landis, and T. Leveder. Nanoimprint lithography processes on 200 mm si wafer for optical application: Residual thickness etching anisotropy. *Journal of Vacuum Science & Technology B*, 25(6):2346–2351, 2007.

[47] T. Nielsen, D. Nilsson, F. Bundgaard, P. Shi, P. Szabo, O. Geschke, and A. Kristensen. Nanoimprint lithography in the cyclic olefin copolymer, topas((r)), a highly ultraviolet-transparent and chemically resistant thermoplast. *Journal of Vacuum Science & Technology B*, 22(4):1770–1775, 2004.

[48] T. I. Kim and S. M. Seo. The facile fabrication of a wire-grid polarizer by reversal rigiflex printing. *Nanotechnology*, 20(14):6, 2009.

[49] L. J. Guo. Recent progress in nanoimprint technology and its applications. *Journal of Physics D-Applied Physics*, 37(11):R123–R141, 2004.

[50] H. Schift. Nanoimprint lithography: An old story in modern times? a review. *Journal of Vacuum Science & Technology B*, 26(2):458–480, 2008.

[51] L. J. Heyderman, H. Schift, C. David, J. Gobrecht, and T. Schweizer. Flow behaviour of thin polymer films used for hot embossing lithography. *Microelectronic Engineering*, 54(3-4):229–245, 2000.

[52] H. Schift, G. Kim, J. Lee, and J. Gobrecht. 3d visualization of mold filling stages in thermal nanoimprint by white light interferometry and atomic force microscopy. *Nanotechnology*, 20(35):6, 2009.

[53] R. H. Pedersen, O. Hansen, and A. Kristensen. A compact system for large-area thermal nanoimprint lithography using smart stamps. *Journal of Micromechanics and Microengineering*, 18(5):9, 2008.

[54] H. Tan, A. Gilbertson, and S. Y. Chou. Roller nanoimprint lithography. *Journal of Vacuum Science & Technology B*, 16(6):3926–3928, 1998.

[55] M. Bender, M. Otto, B. Hadam, B. Vratzov, B. Spangenberg, and H. Kurz. Fabrication of nanostructures using a uv-based imprint technique. *Microelectronic Engineering*, 53(1-4):233–236, 2000.

[56] S. H. Ahn and L. J. Guo. High-speed roll-to-roll nanoimprint lithography on flexible plastic substrates. *Advanced Materials*, 20(11):2044–+, 2008.

[57] L. R. Bao, X. Cheng, X. D. Huang, L. J. Guo, S. W. Pang, and A. F. Yee. Nanoimprinting over topography and multilayer three-dimensional printing. *Journal of Vacuum Science & Technology B*, 20(6):2881–2886, 2002.

[58] Stephan Keller, Daniel Haefliger, and Anja Boisen. Optimized plasma-deposited fluorocarbon coating for dry release and passivation of thin su-8 cantilevers. *Journal of Vacuum Science & Technology B: Microelectronics and Nanometer Structures*, 25(6):1903–1908, 2007.

[59] R. W. Jaszewski, H. Schift, P. Groning, and G. Margaritondo. Properties of thin anti-adhesive films used for the replication of microstructures in polymers. *Microelectronic Engineering*, 35(1-4):381–384, 1997.

[60] B. Bilenberg, M. Hansen, D. Johansen, V. Ozkapici, C. Jeppesen, P. Szabo, I. M. Obieta, O. Arroyo, J. O. Tegenfeldt, and A. Kristensen. Topas-based lab-on-a-chip microsystems fabricated by thermal nanoimprint lithography. *Journal of Vacuum Science & Technology B*, 23(6):2944–2949, 2005.

[61] D. Nilsson, S. Balslev, and A. Kristensen. A microfluidic dye laser fabricated by nanoimprint lithography in a highly transparent and chemically resistant cyclo-olefin copolymer (coc). *Journal of Micromechanics and Microengineering*, 15(2):296–300, 2005.

[62] T. Nishino, M. Meguro, K. Nakamae, M. Matsushita, and Y. Ueda. The lowest surface free energy based on -cf3 alignment. *Langmuir*, 15(13):4321–4323, 1999.

[63] H. Schift, S. Saxer, S. Park, C. Padeste, U. Pieles, and J. Gobrecht. Controlled co-evaporation of silanes for nanoimprint stamps. *Nanotechnology*, 16(5):S171–S175, 2005.

[64] C. A. Tipple, N. V. Lavrik, M. Culha, J. Headrick, P. Datskos, and M. J. Sepaniak. Nanostructured microcantilevers with functionalized cyclodextrin receptor phases: Self-assembled monolayers and vapor-deposited films. *Analytical Chemistry*, 74(13):3118–3126, 2002.

[65] J. J. Headrick, M. J. Sepaniak, N. V. Lavrik, and P. G. Datskos. Enhancing chemi-mechanical transduction in microcantilever chemical sensing by surface modification. *Ultramicroscopy*, 97(1-4):417–424, 2003.

[66] G. Khanarian and H. Celanese. Optical properties of cyclic olefin copolymers. *Optical Engineering*, 40(6):1024–1029, 2001.

[67] A. G. Nagy. Radial etch rate nonuniformity in reactive ion etching. *Journal of the Electrochemical Society*, 131(8):1871–1875, 1984.

[68] http://www.Topas.com/. Topas advanced polymers gmbh, 2009.

[69] S. Keller. *Fabrication of an autonomous surface stress sensor with the polymer SU-8*. Phd-thesis, Technical University of Denmark, 2008.

[70] http://www.microresist.de. micro resist technology gmbh, 2009.

[71] http://www.polytec.com/. Polytec gmbh, 2009.

[72] Guanghua Wu, Ram H. Datar, Karolyn M. Hansen, Thomas Thundat, Richard J. Cote, and Arun Majumdar. Bioassay of prostate-specific antigen (psa) using microcantilevers. *Nat Biotech*, 19(9):856–860, 2001.

[73] M. Yue, H. Lin, D. E. Dedrick, S. Satyanarayana, A. Majumdar, A. S. Bedekar, J. W. Jenkins, and S. Sundaram. A 2-d microcantilever array for multiplexed biomolecular analysis. *Journal of Microelectromechanical Systems*, 13(2):290–299, 2004.

[74] M. Yue, J. C. Stachowiak, H. Lin, R. Datar, R. Cote, and A. Majumdar. Label-free protein recognition two-dimensional array using nanomechanical sensors. *Nano Letters*, 8(2):520–524, 2008.

[75] J. W. Jaworski, D. Raorane, J. H. Huh, A. Majumdar, and S. W. Lee. Evolutionary screening of biomimetic coatings for selective detection of explosives. *Langmuir*, 24(9):4938–4943, 2008.

[76] J. McCafferty, A. D. Griffiths, G. Winter, and D. J. Chiswell. Phage antibodies - filamentous phage displaying antibody variable domains. *Nature*, 348(6301):552–554, 1990.

[77] B. Winter-Jensen. Plasma-polymerisation of polycyclic compounds. Patent WO 2005/092521 A2, 2005.

[78] G. Blagoi, S. Keller, F. Persson, A. Boisen, and M. H. Jakobsen. Photochemical modification and patterning of su-8 using anthraquinone photolinkers. *Langmuir*, 24(18):9929–9932, 2008.

[79] H. P. Lang, R. Berger, F. Battiston, J. P. Ramseyer, E. Meyer, C. Andreoli, J. Brugger, P. Vettiger, M. Despont, T. Mezzacasa, L. Scandella, H. J. Güntherodt, C. Gerber, and J. K. Gimzewski. A chemical sensor based on a micromechanical cantilever array for the identification of gases and vapors. *Applied Physics A: Materials Science and Processing*, 66(0):S61–S64, 1998.

[80] http://www.dme spm.dk/. Danish micro engineering a/s, 2009.

[81] D. Larsson, A. Greve, J. M. Hvam, A. Boisen, and K. Yvind. Self-mixing interferometry in vertical-cavity surface-emitting lasers for nanomechanical cantilever sensing. *Applied Physics Letters*, 94(9):3, 2009.

Appendix A

Publications and Conference Contributions

A.1 Articles

A. Greve, S. Dohn, C. H. Nielsen, N. B. Larsen, and A. Boisen "Wafer-scale Functionalization of Microcantilevers" *In progress*

S. Dohn, **A. Greve**, W. Svendsen, and A. Boisen "Effect of refractive index changes on polymer cantilever based bio/chemical sensors when using the optical lever read-out technique" *(submitted)*

A. Greve, J. Olsen, N. Privorotskaya, L. Senesac, T. Thundat, W.P. King, A. Boisen. "Micro-calorimetric sensor for vapor phase explosive detection with optimized heat profile" Microelectronic Engineering xxx (2009) xxx xxx in press

A. Greve, S. Keller, A. L. Vig, A. Kristensen, D. Larsson, K. Yvind, J. Hvam, M. Cerruti, A. Majumdar and A. Boisen "Thermoplastic microcantilevers fabricated by nanoimprint lithography" J. Micromech. Microeng., Vol. 20, 015009 (2010)

D. Larsson, **A. Greve**, J.M. Hvam, A. Boisen, K. Yvind, "Self-mixing interferometry in vertical-cavity surface-emitting lasers for nanomechanical cantilever sensing" App. Phys. Lett. 94 (2009).

L.R. Senesac, D. Yi, **A. Greve**, J.H. Hales, Z.J. Davis, D.M. Nicholson, A. Boisen, T. Thundat, "Micro-differential thermal analysis detection of adsorbed explosive molecules using microfabricated bridges" Rev. Sci. Instrum. 80 (2009) 035102.

D. Yi, **A. Greve**, J.H. Hales, L.R. Senesac, Z.J. Davis, D.M. Nicholson, A. Boisen, T. Thundat, "Detection of adsorbed explosive molecules using thermal response of suspended microfabricated bridges", Appl. Phys. Lett. 93 (2008) 154102.

C. Ayela, T. Alava, D. Lagrange, D. Rèmiens, C. Soyer, T. Ondarçuhu, **A. Greve**, L. Nicu, "Electronic scheme for multiplexed dynamic behavior excitation and detection of piezoelectric silicon-based micromembranes", IEEE Sensors Journal 8 (2008) 210-217.

A.2 Conferences

A. Greve, J. H. Hales, D. Yi, L. Senesac, T. Thundat, A. Boisen. "Bridge based receptor-free sensor for explosive vapour detection" International Workshop on Nanomechanical Cantilever Sensors (*Talk*) Montréal, Canada. May 27-30, 2007.

A. Greve, J. H. Hales, D. Yi, L. Senesac, T. Thundat, A. Boisen. "Bridge based receptor-free sensor for explosive vapour detection" 33. International conference on micro- and nano-engineering (*Poster*), Copenhagen, Denmark. September 23-26, 2007.

A. Greve, J. H. Hales and A. Boisen "MEMS Based Receptor-Free Detection of Explosives" Nordic Demining Reseach Forum (*Talk*), Varde, Denmark, August 21-24, 2007.

A. Greve, S. Keller, D. Larson, A. Kristensen, K. Yvind, J. Hvam and A. Boisen. "Fabrication of Cantilevers by Nanoimprint Lithography" International Workshop on Nanomechanical Cantilever Sensors (*Talk*), Mainz, Germany. May 19-21, 2008.

A. Greve, S. Keller, D. Larsson, A. Kristensen, K. Yvind, J. Hvam, and A. Boisen. "Fabrication of Cantilevers by Nanoimprint Lithography" Danish Physical Society (*Poster*), Nyborg, Denmark. June 17-18, 2008.

A. Greve, S. Keller, S. Dohn, A. Kristensen, M. Cerruti, A. Majumdar and A. Boisen. "Effects of Surface Structured Polymer Cantilever Fabricated by Nanoimprint Lithography" International Workshop on Nanomechanical Cantilever Sensors (*Poster*), Jeju, Korea. May 20-22, 2009.

A. Greve, S. Dohn, S. Keller, A. L. Vig, A. Kristensen, C. H. Nielsen, N. B. Larsen and A. Boisen. "Wafer Scale Coating Of Polymer Cantilever Fabricated By Nanoimprint Lithography", IEEE MEMS (*Poster*), Hong Kong, China. January 24-28, 2010.

Appendix B

Detailed Process Sequences

Project: Stamp
Operator: Anders Greve
Last revision: 19-03-2009
Substrates: Silicon <100>, 100mm, 525µm, single side
Goal:

Step N	Description	Equipment	Program/Parameters	Ta	A	l
1	Wafer					
	Stock out					
2	Surface structures					
	BHF dip	30 s. BHF 5 min. H20				
	Resist	PR2_2 1.5µm resist				
	Aligner	Exposure hard contact 8 s.	Mask "RIP"			
	Development	Development 60 s. H2O: 5 min.				
	Reactive Ion Etch (RIE)	Si etch Recipe: ef_aniso time: 2.5 min.. SF6: 31 sccm O2: 9 sccm Pressure: 80 mTorr Power: 35 W				
	Resist Strip Acetone	Bath 1: 1 min. Bath 2: 2 min. with US H2O: 5 min with N2 bubles				
3	Cantielver definition					
	BHF dip	30 s. BHF 5 min. H20				
	Resist	PR2_2 1.5µm resist				
	Aligner	Exposure hard contact 10 s.	Mask "IMP"			
	Development	Development 60 s. H2O: 5 min.				
	Reactive Ion Etch (RIE)	Si etch Recipe: ef_aniso time: 15min. SF6: 31 sccm O2: 9 sccm Pressure: 80 mTorr Power: 35 W				
	Resist Strip Acetone	Bath 1: 1 min. Bath 2: 2 min. with US H2O: 5 min with N2 bubles				
4	Oxidation					
	RCA	standard RCA				
	Oxidation	WET1000 time: 90 min.				
	BHF dip	8 min. BHF 5 min. H20				
5	Coating					
	MVD	Rec. "Stamp" multiple cycles				

Anders Greve, DTU Nanotech

Figure B.1: Detailed process sequence for fabrication of stamp.

Project: Fabrication of Topas cantilevers
Operator: Anders Greve
Last revision: 19-03-2009
Substrates: Silicon <100>, 100mm, 525μm, single side
Goal:

Step N	Description	Equipment	Program/Parameters
1	RELEASE COATING WITH FLUOROCARBON		
	Stock out		
	C4F8-passivation	ASE	dry_tef2
2	Topas Imprint		
	Bake	hotplate	5 min 150 C
	Topas Spin	Manual spinner	2500 rpm max. Acc.
	Post Bake	hotplate	10 min 150 C
	Cool down		flat place min. 5 min
	Imprint	EVG NIL	15 kN 30 min 170 C
	Optical inspection	microscope	
	Residual etch	RIE2	Rec. "mbmtopas" 5 min.
	Height test	Dektak	scan center and edge
	Optical inspection	microscope	
3	Metal dep. 1		
	AZ spin	Track1	PR2_2
	AZ exposure	KS Aligner	5s soft(35mJ/cm2)
	RevBake	hotplate	120C, 100s
	Flood exposure	KS Aligner	35s, 3min H2O-rinse
	Develop	developer	60s
	Optical inspection	microscope	
	Metal deposition	Alcatel	5nm Ti; dep. rate 1Å/s, 20nm Au, dep.rate 1Å/s;
	Lift-off	Lift-off bench	30 min with U-sound pulses
	Rinse and drying	Lift-off bench	3min H2O-rinse ; drying on single wafer centrifuge
	Optical inspection	microscope	
4	SU8		
	SU-8 spin-coating	KS Spinner	300rpm, 30s, 100rpm/s; 600 rpm, 60s, 100rpm/s
	SU-8 soft-bake II	Hotplate1	2ºC/min, 10h, 50ºC
	SU-8 exposure	KS Aligner	5x50s 5x350mJ/cm2,
	Post-exposure bake	Hotplate1	2ºC/min, 10h, 50ºC
	SU-8 development	Developer	10 min FIRST, 10 min FINAL
	Rinse	Developer	Isopropanol, Air-drying
9	RELEASE		
9.1	Dry release	manual	
9.2	Optical inspection	Microscope	
10	END OF BATCH		
10.1	Out of cleanroom	-	

Anders Greve, DTU Nanotech

Figure B.2: Detailed process sequence for fabrication of cantilevers.

Project: **Fabrication of shadow mask**
Operator: **Anders Greve**
Last revision: **21-09-2009**
Substrates: **Silicon <100>, 100mm, 525µm, double side**
Goal: **Shadow mask 1,3 and 6,8**

Step N	Description	Equipment	Program/Parameters		
1	Metal				
	Stock out		500 µm wafer double polished		
	Metal	Alcatel	75 nm Al		
	Metal	Alcatel	75 nm Al		
2	Define Cantilever for func.				
	HMDS	HMDS	program 4		
	AZ	Track1	PR2_2		
	UV	EVG Align.	15 s support mask		
	Develop	developer	1 min (3min extra for Al Etch)		
	Acetone	acetone	2+2min		
	Spin 10 µm	SSE Spinner	10 µm		
	UV	KS Aligner	4x30s		
	Develop	developer	~5 min.		
	Optical inspection	microscope			
3	ASE etch 1				
	Etch cant	ASE	40 min (185 cyc.)		
	etch depth	Dektak			
	Strip resist	acetone			
4	ASE etch 2				
	ASE	ASE	120 cyc.		
	etch depth	Dektak			
	bond to carrier	Track1	PR1_5		
	Optical inspection	microscope			
	ASE	ASE	180 cyc.		
5	KOH				
	KOH	KOH	Etch untill alignment possible ~25 min.		
	Optical inspection	microscope			

Conclusion:

Anders Greve, DTU Nanotech

Figure B.3: Detailed process sequence for fabrication of shadow mask.

Appendix C

Matlab files for VCSEL

```
clear all
close all

z=linspace(0,50E-6,2000); % Range of z
r=linspace(-2E-6,2E-6,2000);
Y=erf(z);
b=3E-6;
theta=0.192;

c=1/1.5E-6^2;
erf(0.1)

for i=1:length(z)

geometric(i)=(b/(b+2*tan(theta)*2*z(i)))*100;
boundary(i)=3E-6*(b/(b+2*tan(theta)*2*z(i)))/2;
bound=3E-6*(b/(b+2*tan(theta)*2*z(1)))/2;

Reflect=2*sqrt(pi/(4*c))*erf(sqrt(c)*(boundary(1)))-2*sqrt(pi/(4*c))*erf(sqrt(c)*(-↙
boundary(1)));
Reflected(i)=2*sqrt(pi/(4*c))*erf(sqrt(c)*(boundary(i)))-2*sqrt(pi/(4*c))*erf(sqrt(c)*↙
(-boundary(i)));
profile(i)=exp(-(r(i)^2/(b/2)^2));

percent(i)=Reflected(i)/Reflect*100;
boundp(i)=boundary(i)/bound*100;
difp(i)=percent(i)-boundp(i);
end


figure(2)
plot(z,percent,z,geometric)

figure(3)
plot(r,profile)
```

Figure C.1: Calculation for the reflection of a cantilever back into the VCSEL

```
clear all
close all

% Constants
lambda=850e-9; % wavelength [m]
q_e=1.602e-19; % Electron charge [C]
R_2=.997; % DBR Top mirror Power reflectivity
R_1=0.999; % DBR Bottom mirror power reflectivity
r_2=sqrt(R_2); % DBR Top mirror
r_3=sqrt(0.01); % Cantilever reflection (also calculated in first appendix)
z=linspace(50e-6,53e-6,2000); % Optical path length
eta_i=0.9; % Differential quantum efficiency _i
d_laser=1.4e-6; % Length of Laser cavity
I_th0=4.62e-3 % threshold current 0
g_0=330000 % m^-1 3300 cm^-1
h_planck=6.626e-34; % Plancks constant [J*sec]
c_sl=3e8; % speed of ligth [m/s]
I_cur=4.65e-3

% Calculations
xi=(1-R_2)*(r_3/r_2);

R_eff=R_2*(1+xi^2+2*xi*cos(4*pi*z/lambda));
T_eff=1-R_eff;
F_R=sqrt(R_eff/R_1);                % Part of equation 9 HSU et. al.
F_D=((1-R_eff)+F_R*(1-R_1));        % Part of equation 9 HSU et. al.
for i=1:length(F_D)
    F_z(i)=T_eff(i)/F_D(i);         %
end

%Losses
alpha_m=-log(R_1*R_eff)/d_laser;    % mirror loss
alpha_i=2000;                       % internal loss per m

% Feedback effects on differential quantum efficiency and threshold
%eta_d=F_z*eta_i*0.9; % Differential quantum efficiency (0.9 is due to small loss) ↙
T_eff/((1-R_eff)+sqrt(R_eff/R_1)*(1-R_1));
eta_d=F_z*eta_i.*alpha_m./(alpha_m+alpha_i);

deltag_th=(xi/d_laser)*cos(4*pi*z/lambda);     %
Photon_E=(h_planck*c_sl)/lambda;
I_th=I_th0*exp(deltag_th/g_0);

for i=1:length(I_th)
    Power_outth(i)=eta_d(i)*(Photon_E/q_e)*(I_cur-I_th(i));
end

figure(1)
plot(z, Power_outth)
figure(2)
plotyy(z, I_th,z, eta_d)
figure(3)
plotyy(z, R_eff,z, eta_d)
```

Figure C.2: Calculation for the reflection of a cantilever back into the VCSEL

Appendix D

Mask Designs

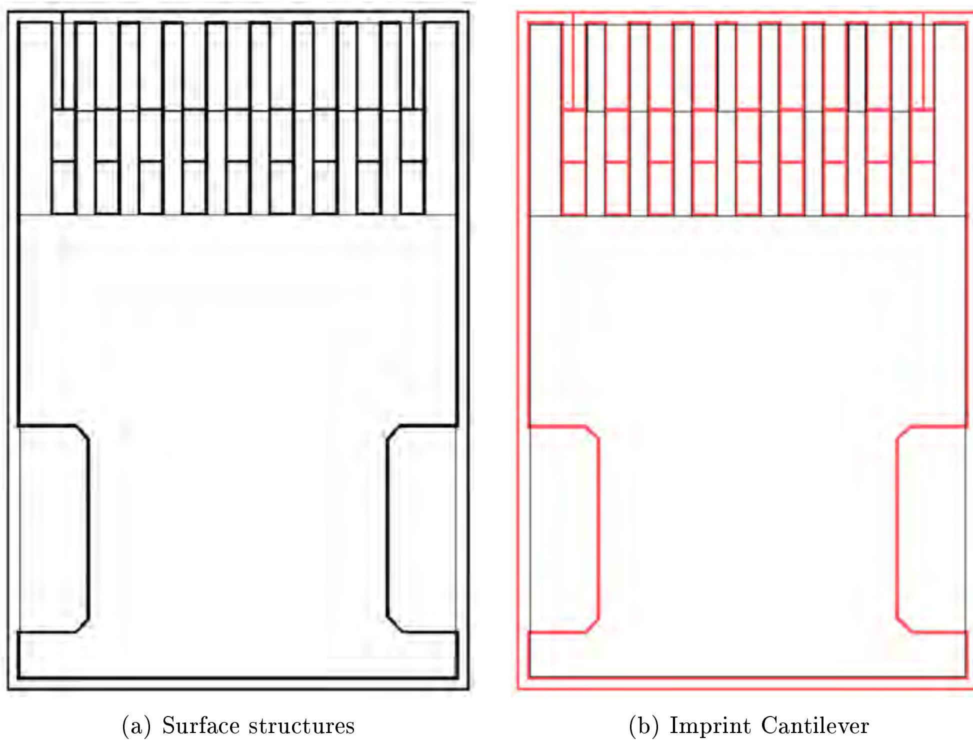

(a) Surface structures

(b) Imprint Cantilever

Figure D.1

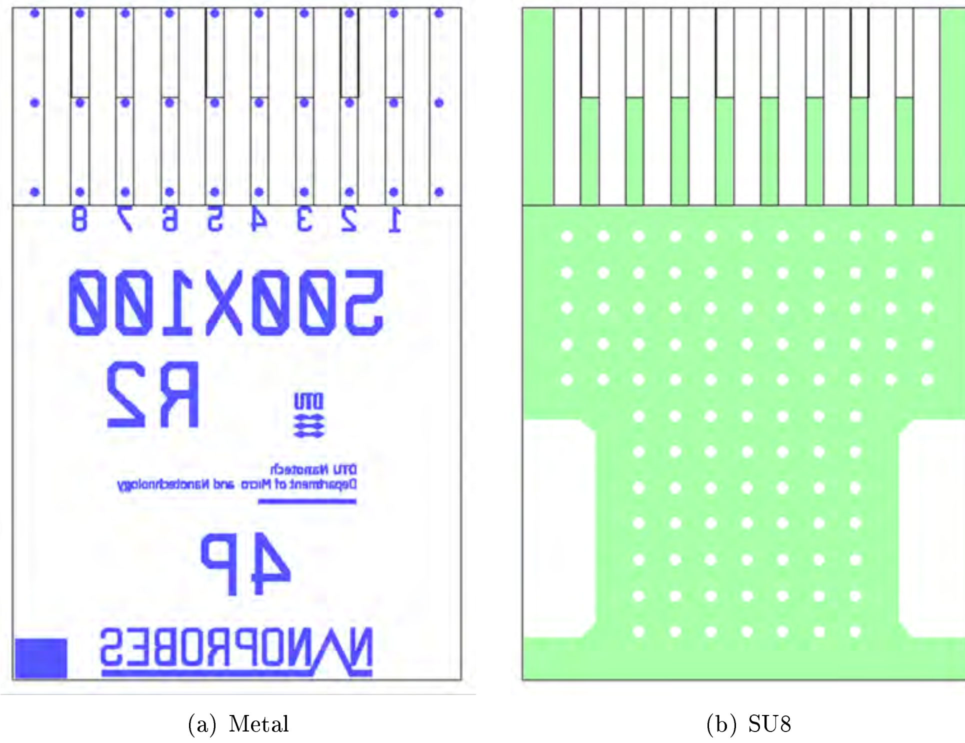

(a) Metal (b) SU8

Figure D.2

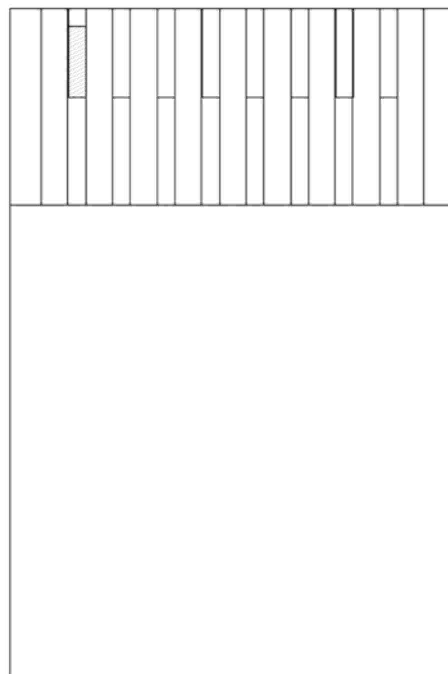

Figure D.3: Functionalization.

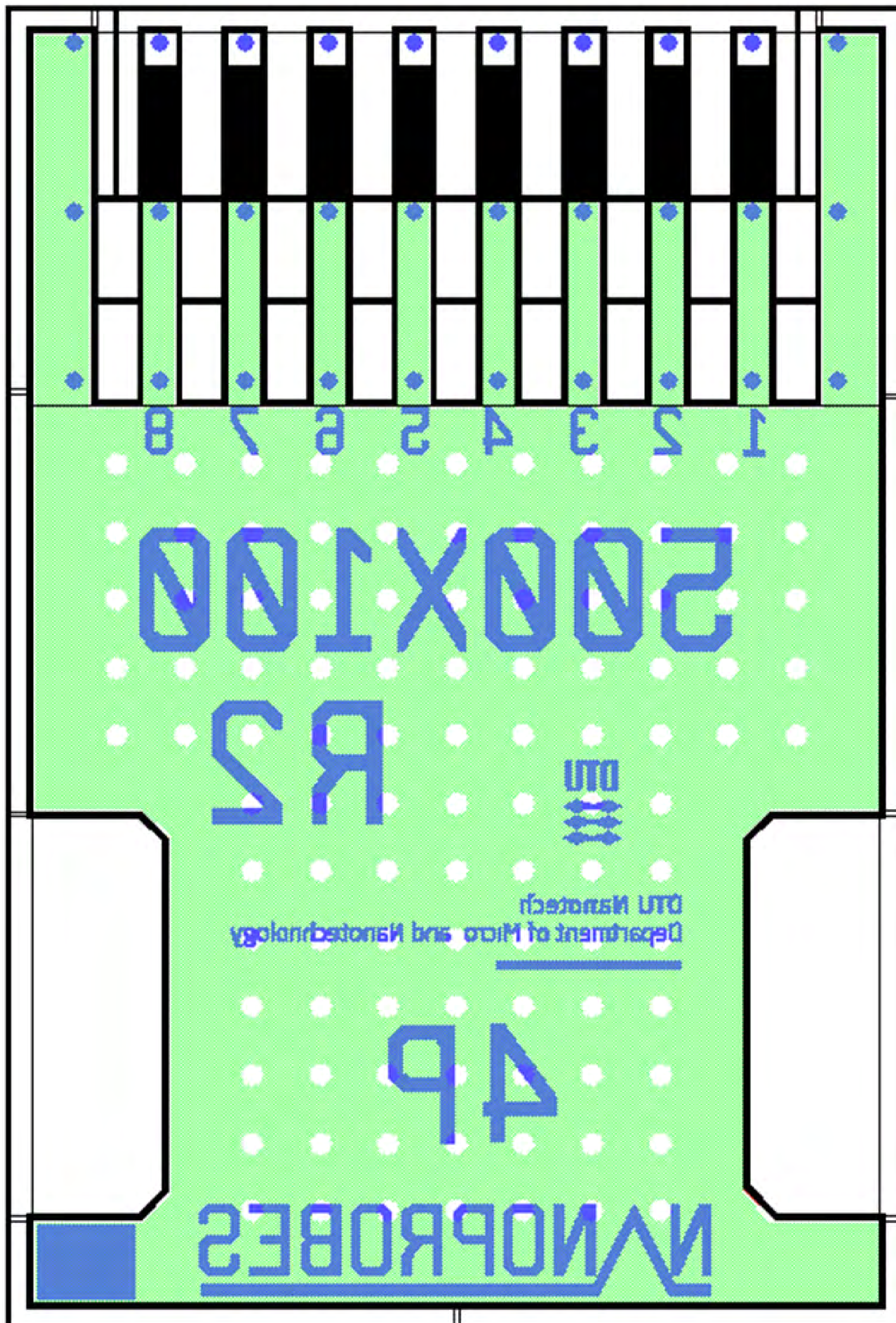

Figure D.4: Single chip All masks

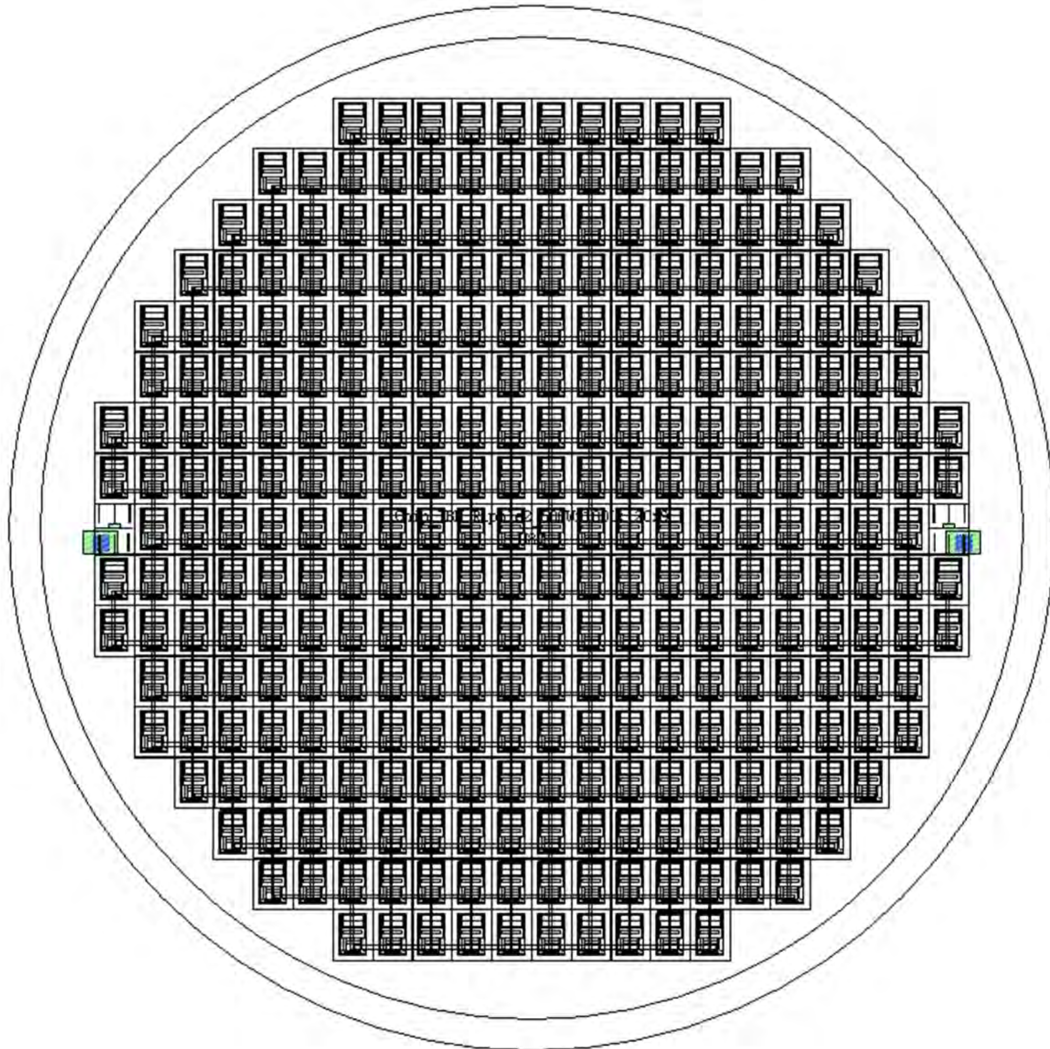

Figure D.5: Wafer